Distribution Agreement

In presenting this thesis or dissertation as a partial fulfillment of the requirements for an advanced degree from Emory University, I hereby grant to Emory University and its agents the non-exclusive license to archive, make accessible, and display my thesis or dissertation in whole or in part in all forms of media, now or hereafter known, including display on the world wide web. I understand that I may select some access restrictions as part of the online submission of this thesis or dissertation. I retain all ownership rights to the copyright of the thesis or dissertation. I also retain the right to use in future works (such as articles or books) all or part of this thesis or dissertation.

Signature:

_____   _____

Xiaohong Wang   Date

Reaction Dynamics and Vibrational Studies of Atmospheric Species on Potential
Energy Surfaces

by
Xiaohong Wang
Doctor of Philosophy
Chemistry

_____
Joel M. Bowman, Ph.D
Advisor

_____
James T. Kindt, Ph.D
Committee Member

_____
Susanna W. Weaver, Ph.D
Committee Member

_____
Francesco Evangelista, Ph.D
Committee Member

Accepted:

_____
Lisa A. Tedesco, Ph.D.
Dean of the James T. Laney School of Graduate Studies

_____
Date

Reaction Dynamics and Vibrational Studies of Atmospheric Species on Potential Energy Surfaces

by

Xiaohong Wang
B.S., University of Science and Technology of China, 2011

Advisor: Joel M. Bowman, Ph.D.

An abstract of
A dissertation submitted to the Faculty of the
James T. Laney School of Graduate Studies of Emory University
in partial fulfillment of the requirements for the degree of
Doctor of Philosophy
in Chemistry
2016

Abstract

Reaction Dynamics and Vibrational Studies of Atmospheric Species on Potential Energy Surfaces

By Xiaohong Wang

The potential energy surface (PES) plays a significant role in the theoretical studies of reaction dynamics and vibrational spectrums. In our work, the PES is obtained using weighted linear least-square fitting method with respect to tens of thousands of scattered electronic energies. The key feature of surfaces is that they are explicitly invariant under all permutations of the same nuclei, which is built into the polynomial basis used for the fitting.

Lots of fundamental chemical reactions implicate crucial processes in atmospheric chemistry. Taking advantage of the above fitting techniques, we can perform detailed dynamics simulations of such reactions, including H_2+CN, photo-dissociation of HOCO, unimolecular decay of Criegee Intermediate, CH_3CHOO. The theoretical exploration, usually collaborating with the experimental studies, throws insight into the microscopic mechanism of the reactions.

The availability of PESs also makes it practical to perform quantum vibrational studies of various systems. Several advanced quantum mechanical methods are implemented and applied in the dissertation work. Diffusion Monte Carlo is applied to solve the ground vibrational states numerically exactly. The variational vibrational configuration interaction approach is used to obtain a large range of vibrational states simultaneously. We have performed the vibrational calculations of many atmospheric species, including C_4, CH_3CHOO and CH_3NO_2, which successfully support and guide the assignment of experimental observations. Besides, an efficient technique is implemented and tested in the latest vibrational calculations, which greatly reduces the computational expense without losing the accuracy.

Reaction Dynamics and Vibrational Studies of Atmospheric Species on Potential Energy Surfaces

by

Xiaohong Wang
B.S., University of Science and Technology of China, 2011

Advisor: Joel M. Bowman, Ph.D.

A dissertation submitted to the Faculty of the
James T. Laney School of Graduate Studies of Emory University
in partial fulfillment of the requirements for the degree of
Doctor of Philosophy
in Chemistry
2016

Acknowledgements

I am really fortunate to have had many who supported and encouraged me over these years. I have never been alone on the road to obtain the Ph.D. Of all the people to whom I want to deliver thanks, I would like to express my deepest gratitude to my advisor, Dr. Joel M. Bowman, for his guidance, patience and continuous support. Through his instruction, I have become a better writer, presenter and independent thinker. More importantly, his everyday lifestyle taught me the attitude necessary to pursuit good science, and guided me to be energetic and optimistic in life. His mentorship was paramount in providing a well rounded experience consistent with my long-term goals.

I would also like to thank Dr. James Kindt, Dr. Susanna W. Weaver and Dr. Francesco Evangelist for taking the time to be committee members of my graduate study and their helpful suggestions. I must also thank Dr. Stuart Carter for his patient guidance and help on the application of the MULTIMODE program.

I must thank all the current and past members in Bowman group: Dr. Yimin Wang, Dr. Riccardo Conte, Dr. Hanchao Liu, Chen Qu, Dr. John S. Mancini, Qi Yu, Dr. Zahra Homayoon, Dr. Gabor Czako, Dr. Bastiaan Braams, especially Chen Qu and Dr. Hanchao Liu, for all their supports and valuable discussions. I am also grateful to Ann Dasher and Susan Browne for their coordination work.

Last but not least, I want to deliver the deepest appreciation to my family, whose encouragement, companionship and unwavering love are always the most faithful strength throughout my life. I also want to thank all my friends, especially Bing Gu, who always gave their unconditional support and encouragement, and stood by me as I went through the difficult times. Because of all these people, every day of my Ph.D. study at Emory has become an enjoyable memory.

Table of Contents

List of Tables

List of Figures

Citations to Previously Published Work

Chapter 4 contains research from two publications:

1. X. Wang, J. M. Bowman *"Zero-point Energy is Needed in Molecular Dynamics Calculations to Access the Saddle Point for H+ HCN$\rightarrow$H$_2$CN* and cis/trans-HCNH* on a New Potential Energy Surface"* J. Chem. Theo. Chem. 9, 901, (2013)

2. B. Yang, P. Zhang, X. Wang, P. C. Stancil, J. M. Bowman, N. Balakrishnan, R. C. Forrey, *"Quantum dynamics of CO-H$_2$ in full dimensionality"*. Nat. Commun. 6, 6629, (2015)

Large portions of Chapter 5 and Chapter 8 about studies of CH$_3$CHOO have appeared in the following three publications:

1. J. M. Bowman, X. Wang, Z. Homayoon, *"Ab initio computational spectroscopy and vibrational dynamics of polyatomic molecules: Applications to syn and anti-CH$_3$CHOO and NO$_3$"*, J. Mol. Spectro. 311, 2, (2014)

2. H. Lin, Y. Huang, X. Wang, J. M. Bowman, Y. Nishimura, H. A. Witek, Y.P. Lee, *"Direct Infrared Identification of the Criegee Intermediates syn-and anti-CH$_3$CHOO and Their Distinct Conformer-Dependent Reactivity"*, Nat. Commun. 6, 7012, (2015)

3. N. M. Kidwell*, H. Li*, X. Wang*, J. M. Bomwan, M. I. Lester *"Unimolecular dissociation dynamics of vibrationally activated CH$_3$CHOO Criegee intermediates to OH radical products"* Nat. Chem. 2016 (Accepted. *Equal contributions of coauthors)

Most of Chapter 6 has been published as:

1. X. Wang, J. M. Bomwan *"Mode-Specific Tunneling in the Unimolecular Dissociation of cis-HOCO to H + CO$_2$"*. J. Phys. Chem. A. 118, 684, (2014)

Chapter 7 includes studies from one publication:

1. X. Wang, X. Huang, J. M. Bowman, T. J. Lee, *"Anharmonic rovibrational calculations of singlet cyclic C$_4$ using a new ab initio potential and a quartic force field"* J. Chem. Phys. 139, 224302 (2014)

Chapter 9 consists of a study from one publication:

1. X. Wang, S. Carter, J. M. Bowman *"Pruning the Hamiltonian Matrix in MULTIMODE: Test for C$_2$H$_4$ and Application to CH$_3$NO$_2$ Using a New Ab Initio Potential Energy Surface"*, J. Phys. Chem. A, 119, 11632 (2015)

Chapter 1

Introduction

Atmosphere contains many different chemical species, and numerous chemical reactions occur in every second. Many studies have been dedicated to promote the understanding of these atmospheric species and associated reactions. Infrared spectrum (IR) is one of the most popular and powerful approaches to study the structures and vibrations of molecules. In order to investigate the mechanism of reactions, various techniques and instruments are invented and developed experimentally. In theory, the dynamic simulations are usually employed to supplement and explain the experimental observations, and are necessary to obtain deep insights into the microscopic reaction mechanism.

The potential energy surface (PES), which describes the molecular interaction for different geometries, is the key for the theoretical study. Accurate PES is the prerequisite for subsequent simulations. Therefore, constructing the PES is the first and the most significant part of each project. Employing an accurate PES, vibrational calculations or/and dynamic simulations are performed to provide details or useful aspects of the chemical system. Quasiclassical trajectory (QCT) approach based on high quality *ab initio* PES is applied to describe reactions for most cases. For the vibrational calculations,

we implemented and applied several quantum mechanical approaches, including diffusion Monte Carlo (DMC) and variational methods.

The dissertation is structured into three parts. The first part involves the main theories and methods we use. In Chapter 2, we describe the construction of PES, which is invariant with respect to the permutation of all like atoms. Chapter 2 will also describes the quasi-classical trajectory approach, covering initial condition sampling and final condition analysis. In Chapter 3, we describe the vibrational calculations methods, including the DMC method and the vibrational configuration interaction calculation.

The second part covers dynamic calculations of several chemical systems. Chapter 4 focuses on the association reaction simulation of H+HCN, in which the importance of including zero-point energy in the dynamic calculation is explored in detail. Chapter 5 describes the construction of a very challenging PES for Criegee intermediate syn-CH_3CHOO. Collaborating with experimental study, we studied the unimolecular decay of syn-CH_3CHOO, resulting in hydroxyl and vinoxy products using QCT simulation. In Chapter 6, we present a one-dimensional model to describe the tunneling effect in the dissociation reaction cis-HOCO$\rightarrow$H+CO_2 as the excitation of specific vibration modes.

In the last part, we present the vibrational calculation applications using different techniques. We start this part from a relatively small system cyclic C_4 molecule in Chapter 7. The energies of ro-vibrational states are calculated using two different approaches, and the results are compared in detail. Then Chapter 8 describes the IR spectrum calculation of both syn- and $anti$-CH_3CHOO isomers, including the survey spectrum and the more accurate calculation of fundamental states. Finally, we introduce a technique which can greatly reduce the Hamiltonian matrix size, and apply in the vibrational calculations of C_2H_4 and CH_3NO_2. Using the technique, the computational cost is greatly reduced without scarifying the accuracy.

Part I

Theory and Methods

Chapter 2

Potential Energy Surface and Dynamic Simulation

2.1   Potential Energy Surface

Under the Born-Oppenheimer approximation, the Schrödinger equation can be solved by separating the electronic and nuclear motions. The solution of molecular electronic Schrödinger equation at each nuclear configuration is known as potential energy. Then the nuclear motion is treated as independent of the electrons, and can be determined by solving the nuclear Schrödinger equation.

The potential energy can be computed by directly solving the electronic Schrödinger equation at specific nuclear geometry using *ab initio* software package. The biggest limitation of calculating the potential energy on-the-fly at each possible configuration is the high computational cost resulting from the large number of points required in the dynamic and vibrational calculations, which is not practical for the complex polyatomic systems. An alternate approach is to build the analytical representation of the poten-

tial energy as a function of geometry for the specific chemical system, which is termed potential energy surface (PES).

The analytical representation of PES have been explored extensively in the literature. The mathematical function of PES can be fitted using different approaches, such as those based on the electronic energies, and semi-empirical adjustment of parameters on the experimental data. In our projects, the PESs are constructed using the direct *ab initio* calculation results. The fitting function of PES needs to incorporate the permutation symmetry of the molecule, which means that the potential energy is invariant with respect to the permutations of the same nuclei. One of the approaches to enforce the permutation invariance is to manually replicate the electronic energies when permuting the identical atoms, as was done for H_2CO[1] and C_2H_2[2]. However, for the system with a high order of permutation symmetry, this approach could result in a huge enlarged dataset, which is not feasible. A more decent approach to build the permutation invariant PES is to incorporate the symmetry into the expression function. This approach uses basis functions that explicitly incorporates the permutation invariance. The molecular configuration can be expressed in different ways, such as Cartesian coordinates and Jacobi coordinate. The representation of molecular geometry we use is the internuclear distance.

This section will start with a brief overview of Born-Oppenheimer approximation, the basis of all the following calculations. Two techniques to generate the permutation invariant fitting basis will be presented, and then followed by the detailed procedure for generating new potential energy surfaces. Dipole moment is the key to calculate the intensities of infrared spectrum. Similar techniques of building PES can be applied to build the dipole moment surface (DMS), which will be briefly discussed in the last part of this section.

2.1.1   Born-Oppenheimer approximation

Even for the simplest molecules, its Schrödinger equation is almost impossible to solve an-alytically. To overcome this difficulty, the Born-Oppenheimer approximation is adopted, which considers the great difference in masses of electrons and nuclei. The full molecular Hamiltonian operator is given by:

$$\hat{H} = \hat{T}_N + \hat{T}_e + \hat{V}_{NN} + \hat{V}_{eN} + \hat{V}_{ee} \tag{2.1}$$

where $\hat{T}_e$ and $\hat{T}_N$ refer to the electronic and nuclear kinetic energy, and $\hat{V}_{NN}$, $\hat{V}_{eN}$ and $\hat{V}_{ee}$ refer to the nuclear-nuclear repulsion, electron-nuclear attraction and electron-electron repulsion energy. The Schrödinger equation $\hat{H}\psi = E\psi$ can in principle explain all the property of molecules. Because the electrons are much lighter, they move much faster than the nuclei and the electronic motion can be separated from the nuclear motion. As a consequence, we can regard the nuclei as fixed and solve the purely electronic equation

$$\hat{H}_{el}\psi_{el} = E_{el}\psi_{el}, \text{ where } \hat{H}_{el} = \hat{T}_e + \hat{V}_{eN} + \hat{V}_{ee} \tag{2.2}$$

Since the nuclei are treated fixed, then the nuclear repulsion energy V_{NN} is just a constant. The total electronic energy is formed by $E_e = E_{el} + V_{NN}$, also known as potential energy.

The separation of electronic and nuclear motion indicate that the total wavefunction ψ can be approximated as the product function

$$\psi \approx \psi_{el}(\mathbf{r}_e; \mathbf{r}_N)\chi_N(\mathbf{r}_N) \tag{2.3}$$

where the two terms are solved from equations

$$(\hat{H}_{el} + \hat{V}_{NN})\psi_{el}(\mathbf{r}_e; \mathbf{r}_N) = E_e(\mathbf{r}_N)\psi_{el}(\mathbf{r}_e; \mathbf{r}_N)$$

$$(\hat{T}_N + U(\mathbf{r}_N))\chi_N(\mathbf{r}_N) = E_N\chi_N(\mathbf{r}_N)$$

(2.4)

Thus, by solving the electronic Schrödinger equation we obtain the potential energy E_e at specific configurations of the molecule. By sampling the molecule at various geometries, we can obtain a sufficiently large dataset to build the function representing the potential energy against the nuclear positions, which is known as potential energy surface (PES). This is the strategy we employed for the projects.

2.1.2 Monomial Symmetrization

To begin, we define the molecular configurations based on the internuclear distance, r_{ij}, of the molecule. Instead of using r_{ij} directly, we use Morse variable $y_{ij} = \exp(-r_{ij}/\alpha)$, where α is constant parameter usually fixed at 2.0 bohr. The transformation will ensure stable representation of potential energy when the internuclear distance is large. The number of internuclear distances depends on the size of the molecule. The first approach of permutation invariant fit is monomial symmetrization, which is straightforward and relatively easy to understand.[3,4]

The potential energy surface can be represented by the expansion of monomials of Morse variables. Take the triatomic molecule A_2B for example, there are three internulcear distances and a single permutation to consider. We first represent the potential as:

$$V(\mathbf{y}) = \sum_{m=0}^{M} C_{abc}[y_{12}^a y_{13}^b y_{23}^c], \ \ m = a + b + c$$

The total degree m over all powers of y_{ij} is constrained at most M. However, using this

mathematical expression, the PES usually does not satisfy permutation invariance unless replicating the energies when permuting identical nuclei. As shown in Figure 2.1, when the $A^{(1)}$ and $A^{(2)}$ permute, the variable y_{12} and y_{13} map onto y_{13} and y_{12} respectively. Therefore, the invariant basis function can be obtained by symmetrizing the single monomial $y_{12}^a y_{13}^b y_{23}^c$ using the corresponding two monomials $y_{23}^c(y_{12}^a y_{13}^b + y_{12}^b y_{13}^a)$. In general, we
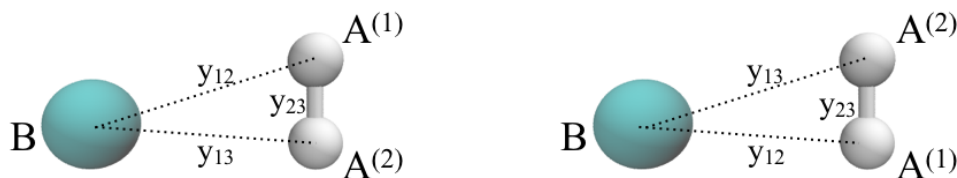
Figure 2.1: Permutation of identical nuclei in the A_2B triatomic system.

can present the permutation invariant function of PES as:

$$V(\mathbf{y}) = \sum_{m=0}^{M} C_{i_1\ldots i_d} S(y_1^{i_1} y_2^{i_2}, \ldots, y_d^{i_d}), \ m = \sum_{n=0}^{d} i_n \tag{2.5}$$

where "S" is the symmetrized operator of monomials. The symmetrized monomial is obtained by adding all permutation equivalent monomials, which reduces the number of independent terms in the PES representation. The number of permutation equivalent monomials is equal to the number of permutations of same atom. Thus, the derivation of symmetrized basis function can be quite complicated. This approach has been implemented systematically by Xie et al, and successfully applied to many systems, such as H_3O^+.[4]

After generating the symmetrized basis functions, the coefficients can be computed using direct linear least square fitting method, and we apply the regular routine from

mathmatical library for this task, such as LAPACK.

2.1.3   Invariant Polynomial

The second approach is based on the theory of polynomial invariants, which will form more compact and efficient permutationally invariant bases. The classical mathematical background can be found in Ref 5, which will be skipped here. Essentially, the potential is expressed as:

$$V(\mathbf{y}) = \sum_{\alpha}^{M} h_\alpha(p_1(\mathbf{y})...p_d(\mathbf{y}))q_\alpha(\mathbf{y}) \tag{2.6}$$

In the expression, d is the fitting dimension, which is equal to $N(N-1)/2$ for the system containing N atoms. $p_i(\mathbf{y})$ is the k-th primary invariant polynomials and $q_\alpha(\mathbf{y})$ is the α-th secondary invariant polynomial. Both primary and secondary polynomials are invariant under permutation symmetry group. There are d primary invariant polynomials and h_α is the polynomial of them. The total order of polynomials is constrained to value M as well.

The number of primary invariant polynomials is equal to the dimension of system, which is $N(N-1)/2$ for N-atom system. Consider the case of A_2B, there is a single primary polynomial associated with the AA bond length, which is $p_1(\mathbf{y}) = y_{23}$. Two primary invariants associate with the two AB distances: $p_2(\mathbf{y}) = (y_{12}+y_{13})/2$ and $p_3(\mathbf{y}) = (y_{12}^2 + y_{13}^2)/2$. There is single secondary invariant $q_1(\mathbf{y}) = 1$. For more complex system, finding the primary and secondary invariant polynomials is not an easy task. The number of secondary invariant polynomials can be easily expressed using the dimension of system or the order of symmetry group. We use the computational algebra software MAGMA[6] to generate these polynomials.

Note that the two approaches mentioned above are almost numerically equivalent

using different expressions. The invariant polynomial approach shows better efficiency by factoring the basis to the product of primary and secondary invariant polynomial. However, the traid-off of the invariant polynomials is that it loses the flexibility to manipulate the basis. Usually, to satisfy specific physical properties of the system, we need to revise the basis function for the better fit. The revision of basis function will be very difficult for the invariant polynomials because of the factorization to two polynomial terms. One example is the PES fitting for the long range interaction of molecules. In order to ensure that the interaction energy is exactly zero at far distance, the basis functions containing the dependent terms of separate molecules need to be removed. These terms can be relatively easy to be found and removed for the monomial symmetrization, in contrast this removal is a quite difficult for the invariant polynomials. This PES fitting strategy for the interaction energy has been applied to several systems such as methane-water interaction.[7]

The efficiency of monomial symmetrization has been improved by Xie *et al* using a systematic approach to factorize the polynomial basis into the multiplication of two lower order polynomials and subtraction of smaller polynomials with the same order.[4] Using this approach, the monomial symmetrization method can run almost at the same speed with the invariant polynomial method.

2.1.4   Dipole Moment Surface

The dipole moment is a vector, and its value is also dependent on the choice of molecule coordinate. Thus the presentation dipole moment surface (DMS) is different from PES.

The dipole moment can be calculated using:

$$\vec{\mu} = \sum_i \omega_i(\mathbf{X})\vec{x_i} \tag{2.7}$$

where $\mathbf{X}$ refers to the Cartesian coordinate of molecule, $\omega_i(\mathbf{X})$ is the effective charge on the ith nuclei which depends on the molecule configuration, and $\vec{x_i}$ is the position vector of the $i-$th nuclei. The effective charges are scalar quantities, which can be expressed using the same approach as PES.

Same with potential energy, the dipole moment is invariant under permutation of like nuclei. In order to make the dipole moment vector invariant, the function $\omega_i(\mathbf{X})$ must be covariant, which means that when permuting identical nuclei i and j, the point charge pair $(\omega_i(\mathbf{X}),\omega_j(\mathbf{X}))$ is equal to the $(\omega_j(\mathbf{X'}),\omega_i(\mathbf{X'}))$. Details of fitting basis to satisfy covariant property can be found in Ref 3,8.

2.1.5   Procedure for Constructing PES

The procedure to generate new PES usually depends on the system and problems we are interested in. According to our experience, there are several steps usually taken for the construction process.

We begin the process by locating the stationary points of the system, which are usually optimized from direct *ab initio* calculation or previous calculations. Initial sampling of the configuration space is performed by running direct molecular dynamics using low-level electronic structure methods such as density functional theory (DFT), and small bases. The direct dynamic calculations are initiated from different stationary points, and are usually simulated at several different energies. Initial samples are chosen from the direct dynamics trajectories. Then we use the desired high-level method to calculate the

electronic energies of sampled geometries. Note that the final electronic structure method choice needs to consider the required accuracy of tasks and computation expense of the method. Based on the energies, we obtain the preliminary PES using a linear least-square fit.

The preliminary PES is improved and tested in various aspects. To ensure the accurate geometries and energetics of stationary points, additional points are usually added to the dataset by randomly sampling configurations around the stationary points. In addition, we compare the harmonic frequencies of stationary points with direct *ab initio* calculations. This step is extremely important for PES which will be used for the vibrational spectroscopy calculation. Furthermore, we always test the PES by running classical molecular dynamics, from which the poorly behaved regions that are not well sampled can be easily detected. The PES are fixed by adding additional configurations in the vicinity regions. A new fit is performed after adding more points, and the process keeps iterating until we are satisfy with the PES.

In this thesis, we present the construction of PES of the following systems, including H_2CN,[9] H_2CO,[10] C_4,[11] CH_3CHOO,[12–14] CH_3NO_2,[15] for the purpose of dynamics simulation and IR spectrum calculation. Details of each PES will be found in the following chapters.

2.2   Molecular Dynamic Simulation

Classical trajectory simulation method is widely used to study the dynamics of chemical systems. The motions of molecules are determined by solving the Hamilton's classical

equations as:

$$\frac{\partial H}{\partial q_i} = -\frac{dp_i}{dt}$$
$$\frac{\partial H}{\partial p_i} = \frac{dq_i}{dt} \tag{2.8}$$

where p_i and q_i are the coordinate and momentum of i-th atom respectively. H is the system's Hamiltonian, which is the sum of kinetic $T(\mathbf{p}, \mathbf{q})$ and potential energy $V(\mathbf{q})$, represented as:

$$H = T(\mathbf{p}, \mathbf{q}) + V(\mathbf{q}) \tag{2.9}$$

Initial conditions are crucial in the dynamic simulations, which are usually chosen to directly compare with experimental results or other calculations or predict the outcome of chemical reactions. Several methods exist for the initial condition sampling.[16] Micro-canonical sampling and normal mode sampling are the two most commonly used methods in our projects. Micro-canonical sampling is an efficient and straightforward method, for which the momentum of system is selected to satisfy the total energy constraint. Without changing the molecular configuration, the velocity of each atom is randomly distributed and then scaled so that the total kinetic energy is equal to a specified value E. Next we will focus on the standard normal mode sampling method.[16–18]

2.2.1 Normal Mode Sampling

To begin, normal mode analysis is performed by diagonalizing the mass-weighted force constant matrix, where we obtain the harmonic frequency ω_i and normal mode vectors $\mathbf{L}$. The Hamiltonian of an n-mode system can be approximately represented by the sum

of energies for each harmonic oscillators, given by:

$$H(\mathbf{P}, \mathbf{Q}) = E = \sum_{i=1}^{n} E_i = \sum_{i=1}^{n} \frac{P_i^2 + \omega_i^2 Q_i^2}{2} \tag{2.10}$$

where P_i and Q_i are the momentum and normal coordinate respectively of i-th mode. In order to form an uniform distribution in the phase space, the values for P_i and Q_i are chosen randomly by giving each normal mode a random phase as:

$$Q_i = [\sqrt{2E_i}/\omega_i]\cos(2\pi R_i)$$
$$P_i = -[\sqrt{2E_i}]\sin(2\pi R_i) \tag{2.11}$$

where R_i is a random number.

The $\mathbf{Q}$ and $\mathbf{P}$ are transformed back to Cartesian coordinate $\mathbf{q}$ and momentum $\mathbf{p}$ using the normal mode vector $\mathbf{L}$ by:

$$\mathbf{q} = \mathbf{q}_0 + M^{-1/2}\mathbf{L}\mathbf{Q}$$
$$\mathbf{p} = M^{1/2}\mathbf{L}\mathbf{P} \tag{2.12}$$

where $\mathbf{q}_0$ is the equilibrium coordinates and $\mathbf{M}$ is the diagonal matrix whose elements are the masses of atoms.

2.2.2   Rotation Sampling

For the rigid rotor, angular momentum can be calculated by summing up the angular momentums of each atom:

$$\mathbf{J} = \sum_{i=1}^{n} L_i = \sum_{i=1}^{n} \mathbf{r}_i \times m_i \mathbf{v}_i \tag{2.13}$$

where $\mathbf{r}_i$ and m_i are the position vector and mass of i-th atom.

Let $v_i = \omega \times r_i$, where ω is the angular velocity of the rigid body, we can derive $\mathbf{J}$ in the form of matrix as:

$$\mathbf{J} = \begin{bmatrix} \sum_{i=1}^{n} m_i(y_i^2 + z_i^2) & -\sum_{i=1}^{n} m_i x_i y_i & -\sum_{i=1}^{n} m_i x_i z_i \\ -\sum_{i=1}^{n} m_i y_i x_i & \sum_{i=1}^{n} m_i(x_i^2 + z_i^2) & -\sum_{i=1}^{n} m_i y_i z_i \\ -\sum_{i=1}^{n} m_i z_i x_i & -\sum_{i=1}^{n} m_i z_i y_i & \sum_{i=1}^{n} m_i(x_i^2 + y_i^2) \end{bmatrix} \begin{bmatrix} \omega_x \\ \omega_y \\ \omega_z \end{bmatrix} \tag{2.14}$$

By diagonalizing the moment of inertia matrix, the molecule can be transformed to the principle axis frame. In principle axis frame, the $\mathbf{J}$ vector elements can be simplified to:

$$J_x = I_{xx}\omega_x; \ \ J_y = I_{yy}\omega_y; \ \ J_z = I_{zz}\omega_z \tag{2.15}$$

The desired angular momentum $\mathbf{J}$ can be obtained by adjusting the velocities of each atom. Note that spurious angular momentum $\mathbf{j}_s$ can be added through the initial normal mode sampling step. The desired angular momentum $\mathbf{j}_f$ is added to the molecule by forming the vector $\mathbf{j} = \mathbf{j}_f - \mathbf{j}_s$. Rotational velocity $\omega \times \mathbf{r}_i$ is added by:

$$\omega = I^{-1}\mathbf{j} \tag{2.16}$$

where $\mathbf{I}^{-1}$ is the inverse of the momenta of inertia matrix.

Once the angular moment vector $\mathbf{J}$ is determined, we can calculate the rotational energy of the molecule. In principle axis frame, the rotational energy can be expressed by:

$$E_{rot} = \frac{1}{2}(\frac{J_x^2}{I_x} + \frac{J_y^2}{I_y} + \frac{J_z^2}{I_z}) \tag{2.17}$$

2.2.3   Zero Point Energy Constraint

After the simulations have finished forming the desired products, the final configurations and momenta of trajectories can be used to analyze the properties of the products.[19]

One of the well-known issues of quasi-classical trajectory is the zero-point energy (ZPE) violation of products. No matter how we sample and assign ZPE to each normal mode initially, the energies in these modes can fluctuate during the simulations. Such unphysical flow of ZPE tends to enhance the rate of intramolecular vibration energy redistribution of the molecule. Besides, the products can be formed with energies less than their ZPE, which may affect the results of final analysis.

Different models have been proposed and applied to address the ZPE violation issue of QCT simulation.[20–24] Many methods involve the control of energies in each mode during the simulation, which may cause the discontinuity and noise of trajectories. We employ two straightforward methods to deal with ZPE violation, soft ZPE constrain and hard ZPE constrain. Soft ZPE constrain means that the total vibrational energies of all products have to be larger than the sum of their ZPEs, otherwise the trajectory will be discarded. Hard ZPE constrain is a similar but more restrictive approach, in which the vibrational energy of each fragment has to be larger than its ZPE, otherwise the trajectory is discarded. Usually, the harmonic ZPE is used to determine the ZPE violation, which is equal to $E = \frac{1}{2} \sum_{i=1}^{n} \omega_i$. Anharmonic ZPE of products is a better choice, which is almost always smaller than the harmonic ZPE.

2.2.4   Final Conditions

The total available energy in the reaction is distributed as the internal energies and the translation energies of products. For the reaction with more than one product, the

relative velocity between fragments is also an important property of the reaction. Here we choose a chemical reaction forming two products C and D as an example.

The relative velocity between two products is the difference between the velocities of the center of mass of products. The vector between the center of mass of products C and D is:

$$R = (X_D - X_C)\hat{\mathbf{i}} + (Y_D - Y_C)\hat{\mathbf{j}} + (Z_D - Z_C)\hat{\mathbf{k}} \tag{2.18}$$

and the relative velocity is:

$$\dot{\mathbf{R}} = \dot{R}_x\hat{\mathbf{i}} + \dot{R}_y\hat{\mathbf{j}} + \dot{R}_z\hat{\mathbf{k}} \tag{2.19}$$

where X_C and $\dot{X}_C$ are the center of mass position and velocity of product C. Then the product relative translation energy can be calculated as:

$$E_{\text{rel}} = \frac{1}{2}\mu_{CD}\dot{\mathbf{R}} \cdot \dot{\mathbf{R}} \tag{2.20}$$

where μ_{CD} is the reduced mass of C and D.

The internal energy of product C is:

$$E_{\text{int}} = T_C + V_C \tag{2.21}$$

where T_C and V_C are the kinetic and potential energies of product C respectively. The potential energy V_C can be easily calculated using potential energy surface.

$$T_C = \frac{1}{2}\sum_{i=1}^{n} m_i(\dot{x}_i'^2 + \dot{y}_i'^2 + \dot{z}_i'^2) \tag{2.22}$$

Note that the velocity of product C here is in the center-of-mass frame by $\dot{x}_i' = \dot{x}_i - \dot{X}_C$.

The separation of vibrational and rotational energies is not trivial for the polyatomic

molecules. The rotational energy can be calculated classically by:

$$E_{\text{rot}} = \frac{1}{2}\left(\frac{J_x^2}{I_x} + \frac{J_y^2}{I_y} + \frac{J_z^2}{I_z}\right) \tag{2.23}$$

where the angular moment $\mathbf{J}$ of products can be easily calculated classically. The vibrational energy can be determined after calculating the internal energy and rotational energy.

Chapter 3

Vibrational Calculation

The theoretical modeling of molecular vibrations is an important topic in many related fields. The vibrational studies usually relate to solve the molecular Hamiltonian, sum of the kinetic energy and potential energy, which is a very challenging task for the poly-atomic system. Many different models and techniques are reported to solve the anharmonic molecular vibration problems. In this section, we will mainly talk about two techniques. First, the diffusion Monte Carlo (DMC) technique is introduced to numerially solve for the ground state vibrational properties of molecular systems. [25–27] Next, we consider the quantum mechanical approach to solve the nuclear Schrödinger equation using variational theory. The MULTIMODE program is mostly applied in the vibrational calculations, which implements the vibrational self-consistent field (VSCF) and vibrational configuration interaction (VCI) approaches. We will employ the PES that are fitted using the *ab initio* electronic energies to calculate the potential energy efficiently.

3.1 Diffusion Monte Carlo

Diffusion Monte Carlo (DMC) method is widely used to accurately calculate the ground vibrational state energy and wavefunctions of molecular systems. DMC method also has been adapted to solve the first excited state, which will not be discussed here. We begin the derivation of DMC approach from the time-dependent Schrödinger equation. For simplicity, we only consider the one-dimensional system for now. The Schrödinger equation is expressed as:

$$i\hbar\frac{\partial\Psi}{\partial t} = \frac{\hbar^2}{2m}\frac{\partial^2\Psi}{\partial x^2} + V(x)\Psi \tag{3.1}$$

where $V(x)$ is the potential energy. The solution of Schrödinger equation is:

$$\Psi(x,t) = \sum_{n=0}^{\infty} c_n\phi_n(x)e^{-i\frac{E_n}{\hbar}t} \tag{3.2}$$

where $\phi_n(x)$ and E_n are the eigenstates and eigenvalues of the time-independent Schrödinger equation of $\hat{H}\phi_n(x) = E_n\phi_n(x)$.

Two transformations are performed in DMC approach. First, the energy scale is shifted from $V(x)$ to $V(x) - E_R$ and E_n to $E_n - E_R$. Then the real time is transformed to imaginary time using $\tau = it$. The obtained imaginary time Schrödinger equation is

$$\hbar\frac{\partial\Psi}{\partial\tau} = \frac{\hbar^2}{2m}\frac{\partial^2\Psi}{\partial x^2} - [V(x) - E_R]\Psi \tag{3.3}$$

and the corresponding solution becomes:

$$\Psi(x,\tau) = \sum_{n=0}^{\infty} c_n\phi_n(x)e^{-\frac{E_n-E_R}{\hbar}\tau} \tag{3.4}$$

Now consider the imaginary time wavefunction for the ground vibrational state, where

$n = 0$, three different situations can occur when $\tau \to \infty$.

1. If $E_0 > E_R$, the wavefunction $\Psi(x, \tau)$ exponentially vanishes to 0

2. If $E_0 < E_R$, the exponential term in $\Psi(x, \tau)$ diverges to infinity

3. If $E_0 = E_R$, $\Psi(x, \tau)$ converges to ground state wavefunction $c_0\phi_0$

The final convergence is the basis for DMC approach to compute the ground vibrational state energy and wavefunction. The formula of DMC process can be derived from diffusion-branching process. The imaginary time Schrödinger equation can be analogous to the diffusion equation

$$\frac{\partial C}{\partial t} = D\frac{\partial^2 C}{\partial x^2} - kC \tag{3.5}$$

by letting $D = \frac{\hbar^2}{2m}$ and $k = [V(x) - E_R]/\hbar$. The second-derivative part of Equation 3.5

$$\frac{\partial C}{\partial t} = D\frac{\partial^2 C}{\partial x^2} \tag{3.6}$$

is the Einstein equation, which can be simulated using the random work process and the diffusion constant is given by $D = \frac{(\Delta x)^2}{2\Delta\tau}$. In the random walk process, each walker takes a random step with the step size chosen based on Gaussian probability density

$$P(\Delta x) = \frac{1}{\sqrt{2\pi}\sigma}\exp\left[-\frac{(\Delta x)^2}{2\sigma^2}\right] \tag{3.7}$$

where $\sigma = (2D\Delta\tau)^{1/2}$. For the imaginary time Schrödinger equation, we have $\sigma = (\hbar\Delta\tau/m)^{1/2}$.

The first order part in diffusion equation

$$\frac{\partial C(x, t)}{\partial t} = -kC(x, t) \tag{3.8}$$

can be solved easily by

$$C(x, t + \Delta t) = C(x, t)e^{-k\Delta t} \tag{3.9}$$

By analogy, we can get the similar solution of Schrödinger equation

$$\Psi(x, \tau + \Delta\tau) = \Psi(x, \tau)e^{-(V(x)-E_R)\Delta\tau} \tag{3.10}$$

This first-order derivative part can be simulated by a branching process. We define a weight function $W(x) = \exp[-(V(x) - E_R)\Delta\tau]$. In the branching process, $W(x)$ is calculated for each walker. The random walkers with $W(x) > 1$ create offspring at the same position and walkers with $W(x) < 1$ are removed. The DMC approach can also be derived using Feynman path integral. The derivation details can be found in Ref 26, which will not be discussed here.

The actual steps in the DMC simulation can be summarized as follows. The simulation step size, total propagation time and the number of random walkers are pre-determined. All random walkers initially start from the reference configuration. In the diffusion step, the coordinate of random walker j at i-th step is propagated as:

$$x_{i+1}^j = x_i^j + \sigma\rho_i^j \tag{3.11}$$

where $\sigma = \sqrt{\hbar\Delta\tau/m}$ and ρ_i^j is the random value selected from Gaussian probability with mean 0 and standard derivation 1. The weight function $W(x)$ is calculated for each new configuration, along with an integer $m = \min\left(int[W(x_{i+1}^j) + \mu], 3\right)$. Here μ is a random number between 0 and 1, and int is a function returning the integer value. The vanish and birth of given walker is determined based on m value. If $m = 0$, the walker is removed; if $m = 1$ the walker is accepted at new configuration; if $m = 2, 3$, then $m - 1$ walkers are

added at that configuration. After the birth-death process, the new reference energy E_R is updated as

$$E_R = < V > -\alpha \frac{N_i - N_0}{N_0} \qquad (3.12)$$

where $< V >$ represents the average potential energy of all of the random walkers at ith step and α is the parameter which is generally chosen as the inverse of time step. Then we continue the DMC propagation step. In DMC, usually the first few thousand steps are used to equilibrate the system. After a few thousand steps, the energies are accumulated to compute the final ground state energy.

Besides calculating the ground state energy, another application of DMC simulation is the visualization of ground state wavefunction,which is first applied in Ref 28. The visualization of wavefunction is based on the distribution of the final walkers. At first, all the walkers are transformed into the Eckart frame relative to the reference, which is usually a stationary point. Then a quartic kernel density estimator is applied to the coordinates of walkers to compute volumetric elements for each type of atom. These volumetric information is written to a Gaussian cube file, which can be visualized using the VMD package.

3.2   MULTIMODE

Diffusion Monte Carlo is an efficient method to numerically solve the nuclear Schrödinger equation exactly. However, this method is restricted to the ground vibrational state and limited excited states. Now we focus on another quantum approach that will allow us to calculate the large range of excited states. This approach is based on the variational theory, which is implemented in the MULTIMODE (MM) program.[29,30] The method uses

the Watson Hamiltonian in normal coordinates, which makes some approximations of the potential representation to reduce the computation cost. This program has been applied to a variety of fairly large polyatomic molecules.

3.2.1 Hamiltonian and Potential

For the nonlinear molecules, the Watson Hamiltonian[31] is given by

$$\hat{H} = \frac{1}{2}\sum_{\alpha\beta}(\hat{J}_\alpha - \hat{\pi}_\alpha)\mu_{\alpha\beta}(\hat{J}_\beta - \hat{\pi}_\beta) - \frac{1}{2}\sum_k^N \frac{\partial^2}{\partial Q_k^2} - \frac{1}{8}\sum_\alpha \mu_{\alpha\alpha} + V(\mathbf{Q}) \tag{3.13}$$

where α and β indicates the x, y, z coordinates, $\hat{J}_\alpha$ and $\hat{\pi}_\alpha$ are the total and vibrational angular momentum respectively, $\mu_{\alpha\beta}$ is the inverse of effective moment of inertia, and $V(\mathbf{Q})$ is the potential energy in terms of normal coordinate $\mathbf{Q}$. Note that this approach is not applicable for linear molecules because one of the moments of inertia will be zero.

The key approximation in MM is to represent the full potential using hierarchical n-mode representation (nMR) in normal coordinates.[30]

$$\begin{aligned}
V(Q_1, Q_2, \cdots, Q_N) &= \sum_i V_i^{(1)}(Q_i) + \sum_{i,j} V_{ij}^{(2)}(Q_i, Q_j) + \sum_{i,j,k} V_{ijk}^{(3)}(Q_i, Q_j, Q_k) \\
&+ \sum_{i,j,k,l} V_{ijkl}^{(4)}(Q_i, Q_j, Q_k, Q_l) + \cdots + \sum_{i,\cdots,N} V_{i\cdots N}^{(N)}(Q_i, \cdots, Q_N)
\end{aligned} \tag{3.14}$$

In the expansion, the one-mode representation $V_i^{(1)}(Q_i)$ corresponds to the potential that just Q_i coordinate varies and all the other normal coordinates fixed at zero. The two-mode representation contains the one-mode term plus the $V_{ij}^{(2)}(Q_i, Q_j)$, where $V_{ij}^{(2)}(Q_i, Q_j) = V(Q_i, Q_j) - V_i^{(1)}(Q_i) - V_j^{(1)}(Q_j)$ and only Q_i and Q_j are non-zero. The remaining n-mode term $V_{i\cdots N}^{(N)}(Q_i, \cdots, Q_N)$ can be formulated in the same pattern. Because of the limitation

of computational resources, the potential expansion is usually truncated at the value smaller than 6. It will be shown later that such truncation will make the calculations of large systems more feasible.

3.2.2   Variational Calculation

To solve the eigenvalues and eigenfunction of Watson Hamiltonian, we start from the vibrational self-consistent field (VSCF) calculation.[32,33] The initial trial function is the simple product of the single wavefunction for each mode.

$$\Psi^{VSCF}_{n_1,\cdots,n_N}(\mathbf{Q}) = \prod_{i=1}^{N} \phi^{(i)}_{n_i}(Q_i) \tag{3.15}$$

where $\phi^{(i)}_{n_i}$ is the eigenstate of ith normal mode. By solving the set of coupled VSCF equations for $J = 0$, we obtain the optimal wavefunctions $\phi^{(i)}_{n_i}$.

$$\left[T_l + \left\langle \prod_{i\neq l}^{N} \phi^{(i)}_{n_i} | V + T_c | \prod_{i\neq l}^{N} \phi^{(i)}_{n_i} \right\rangle - \epsilon^{(l)}_{n_l} \right] \phi^{(l)}_{n_l}(Q_l) = 0, \; l = 1, \cdots, N \tag{3.16}$$

where

$$T_l = -\frac{1}{2}\frac{\partial^2}{\partial Q_l^2}, \; T_c = \frac{1}{2}\sum_{\alpha\beta}\hat{\pi}_\alpha\mu_{\alpha\beta}\hat{\pi}_\beta - \frac{1}{8}\sum_\alpha \mu_{\alpha\alpha}$$

As seen, the integration is over $N - 1$ normal mode coordinates. The high-dimensional integration could be quite expensive for large system. Because of n-mode representation of full potential, we can transform the multidimensional integration to the sum of all one-mode, two-mode, ..., n-mode integrations. The cost is greatly reduced in this case. The coupled VSCF equations are solved iteratively for each mode. The modal wavefunctions $\phi^{(i)}_{n_i}$ are expressed as the linear expansion of finite harmonic oscillator basis, and the goal

is to solve the unknown coefficients. Once convergence is achieved, the eigenfunctions of the VSCF Hamiltonian form an orthonormal space. The calculated eigenfunctions $\Psi_{n_1,\cdots,n_N}^{VSCF}(\mathbf{Q})$ are the VSCF states.

Several approaches exist to go beyond the VSCF description to obtain more accurate energies. One of the popular approaches is to use second-order perturbation theory to correct VSCF.[34,35] In MM, we use vibrational configuration interaction (CI) approach to go beyond the VSCF calculations by explicitly including correlation among modes.[36] In the VCI calculation, the total wave-function is expanded in terms of the virtual states of VSCF Hamiltonian. The VSCF states form the orthonormal basis function, which results in a standard eigenvalue problem.

$$\Psi(\mathbf{Q}) = \sum_m C_m \Psi_m^{(VSCF)} = \sum_m C_m \prod_{i=1}^{N} \phi^{(i)}(Q_i) \tag{3.17}$$

where $\phi^{(i)}(Q_i)$ comes from the previous VSCF iteration of each mode.

Due to the high-dimensionality of problems, the VCI scheme can usually result in large Hamiltonian matrices, and a very flexible basis set selection method is developed for the VCI scheme in MM. The VCI excitation is divided into one-mode, two-mode, until six-mode excitations at most, and the total sum of excitations in each n-mode excitation space is restricted. In addition, the maximum number of excitations for each mode is further restricted. The symmetry of molecules is usually applied when appropriate. By incorporating the symmetry, the Hamiltonian matrix can be partitioned into several diagonal blocks since the coupling between states in different symmetry is always zero.

Many modifications have been implemented into the MM program to solve various problems. One of the commonly used functionalities is to pre-specify the arbitrary normal modes of the molecule. This is particularly useful when we need to deal with large systems

and only a few specific vibration modes are of interest. Even with all the techniques to reduce the computational cost, we will usually end up with huge Hamiltonian matrix. A new technique has been implemented in the MM code and tested thoroughly, which will be discussed in detail later.[15,37]

3.2.3   Infrared Intensity

We need the dipole moment surface (DMS) for the computation of infrared intensities. Here we only consider the pure vibration transition with $J = 0$. After solving the the vibrational states from VSCF or VCI calculation, the transition dipole matrix element can be calculated using[38]

$$R^{\alpha}_{\nu\nu'} = \langle \Psi_{\nu}(\mathbf{Q}) | \mu^{\alpha}(\mathbf{Q}) | \Psi_{\nu'}(\mathbf{Q}) \rangle \tag{3.18}$$

where $\Psi_{\nu}(\mathbf{Q})$ and $\Psi_{\nu'}(\mathbf{Q})$ are the wavefunctions for the vibration state ν and ν' respectively. $\mu^{\alpha}(\mathbf{Q})$ is the dipole moment component of the molecule, where $\alpha = x, y, z$. The integration is based on the normal coordinate $\mathbf{Q}$. Thus the dipole moment is first represented using the similar n-mode representation as for the potential energy.

After calculating the transition elements $R^{\alpha}_{\nu\nu'}$, the infrared intensities of the $\nu \to \nu'$ are evaluated using the expression

$$A(E_a) = \frac{8\pi^3 N_{AV}}{3hc \times 4\pi\epsilon_0} E_a \sum_{\alpha=x,y,z} |R^{\alpha}_{\nu\nu'}|^2 (N_{\nu} - N_{\nu'}) \tag{3.19}$$

where E_a is the transition wavefunction between two states, and N_{ν} is the number of molecules in the state ν. Considering the transitions from the ground vibrational state at equilibrium distribution, the term $N_{\nu} - N_{\nu'}$ tends to 1.

Part II

Application: Reaction Dynamics Simulation

Chapter 4

Dynamic Simulations of H+HCN Reaction

4.1 Introduction

The H_2CN system has attracted wide interest and has been the focus of many theoretical studies from both classical and quantum calculations, especially the reaction $H_2+CN \rightarrow H+HCN$.[36,39–53] The construction of an accurate potential energy surface (PES) is essential to study the reaction dynamics of the system. Several PESs for H_2CN system have been constructed before. Sun and Bowman reported a semi-empirical PES based on *ab initio* calculations of the saddle points (SP).[41] Reduced dimensionality quantum reactive scattering calculation for $H_2+CN \rightarrow H+HCN$ was done with this PES, which does not describe the formation of the CNH_2 complex and then H+HNC product. In a later study, Horst et al.[43] carried out multireference configuration interaction calculations, and constructed a global PES using many-body expansion. The H_2+CN reaction was studied in detail using QCT calculations based on the PES. Later, Sumathi and Nguyen[44] reported

the doublet and quartet PESs which covered more stationary points using CCSD(T) method with 6-311++G(d,p) basis. The rate constants of various addition reactions were determined using a quantum Rice-Ramsperger-Kassel (QRRK) theory, where they noted some quantitative differences with the earlier Horst et al. results.

Previous dynamic studies were mainly focused on the reaction $H_2+CN\rightarrow H+HCN$, which has a reaction barrier of about 3-4 kcal/mol. Several studies also considered the reverse reaction.[49,50,53] To the best of our knowledge, there are quite few dynamical studies of the title association reactions of H+HCN. There have been a number of studies of the energetics of these reactions. In 1980s, Bair et al.[39,40] performed the *ab initio* calculations of various reactions starting from H+HCN using GVB-CI and POL-CI methods. Starting with the reaction of HCN with hydrogen atom, there are several interesting reactions we need to consider as follows[44]:

$$H+HCN \rightarrow H_2CN^* \qquad\qquad (R1)$$

$$H+HCN \rightarrow \mathit{cis}\text{-}HCNH^* \qquad\qquad (R2)$$

The isomerization reaction of HCNH can easily occur because of the small barrier:

$$\mathit{cis}\text{-}HCNH^* \rightarrow \mathit{trans}\text{-}HCNH^* \qquad\qquad (R3)$$
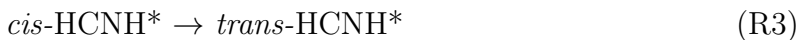
As we will show below, there is also a direct pathway from H+HCN to *trans*-HCNH*. In addition, at higher energies the reaction $H+HCN\rightarrow H_2+CN$ can happen, however, this channel is not open at the energies of interest here.

In this chapter, we present a high-quality, *ab initio* global PES of H_2CN system for

the ground doublet electronic state. Using the PES, we studied two sets of dynamic calculations of the association reactions. One is the quasiclassical trajectory (QCT) method, in which the reactant HCN has zero-point energy. This method is the standard one used in gas-phase reaction dynamics. The second one is the strictly classical trajectory (CT) method, without zero-point energy (ZPE) of the reactant. This method is widely used in condensed phase and/or large molecule molecular dynamics simulations. One focus here is the comparison of the threshold energies for various association reactions using these two methods.

In Section 4.2, we describe the computational details of the PES, including the *ab initio* calculations, PES fitting, and accuracy test of the PES. In Section 4.3, QCT and CT calculations are reported for the H+HCN association reactions. The summary and conclusions are presented in Section 4.4. Then in the last section, we present the PESs we have build for the similar systems with X_2YZ pattern. These PESs have been successfully applied for the accuracy quantum scattering calculation, which will not be discussed here.

4.2   Potential Energy Surface Construction

4.2.1   *Ab Initio Calculation*

The electronic structure calculations are performed using the F12 version of the singles and doubles coupled-cluster method that includes a triple perturbation (CCSD(T)-F12b),[54,55] with aug-cc-pvDz basis.[56,57] All the *ab initio* calculations are performed using MOLPRO[58] package.

H_2CN is an open shell system, and we are interested in the low lying doublet state. The potential energy surface for the doublet H_2CN has been studied using various *ab initio*

methods. The present CCSD(T)-F12b calculations give the $H_2+CN \leftrightarrow H+HCN$ reaction barrier of about 3.6 kcal/mol, which is in agreement with the experimental estimate of 3-4 kcal/mol.[45,46]. For the generation of fitting dataset, the majority of configurations were obtained by running classical direct-dynamics calculations, using density functional theory (DFT) with the aVDZ basis, starting from various stationary points and with a variety of total energies. Preliminary fits were done and then refined by running additional direct-dynamics calculations. Finally, CCSD(T)-F12b/aVDZ electronic energies were calculated at roughly 60,000 configurations for the PES fitting.

4.2.2   Potential Energy Surface Fitting

The potential energy surface of H_2CN system is six dimensional. In addition, the PES should be invariant with respect to permutation of the two H atoms. Thus, we utilize the monomial symmetrization to generate the fitting basis, and expand the expression of PES as follows:[3]

$$V(y_1, \cdots, y_6) = \sum_{n_1,\cdots,n_6}^{M} C_{n_1,\cdots,n_6} y_1^{n_1} y_6^{n_6} (y_2^{n_2} y_3^{n_3} y_4^{n_4} y_5^{n_5} + y_2^{n_5} y_3^{n_4} y_4^{n_3} y_5^{n_2}) \qquad (4.1)$$

where y_i is the Morse variable given by $y_i = \exp(-r_i/\alpha)$ with α fixed at 2.0 bohr, and r_i is the bond length. The internuclear distances are specified as: $r_1 = r_{HH}, r_2 = r_{NH}, r_3 = r_{CH}, r_4 = r_{CH'}, r_5 = r_{NH'}, r_6 = r_{CN}$. The threshold energy of configurations is set to 80 kcal/mol relative to the H_2CN global minimum, and 59,868 points are included for the PES fitting after the energy cutoff. The total power of polynomial is restricted to 7, and coefficients were obtained using standard weighted least-squares fitting. In order to ensure the accuracy at relatively low-energy range, weight of configurations is employed in the fitting. Weight of points with energies less than 60 kcal/mol relative to the global

minimum is equal to 1, from 60 to 70 kcal/mol the weight is 0.7, and above 70 kcal/mol

is 0.5. Figure 4.1 shows the number of configurations in different energy ranges and the

corresponding root mean square (RMS) fitting error. Most sampled points are in the

energy range from 0 to 60 kcal/mol, and as indicated the RMS fitting error up to this

energy is 0.45 kcal/mol.
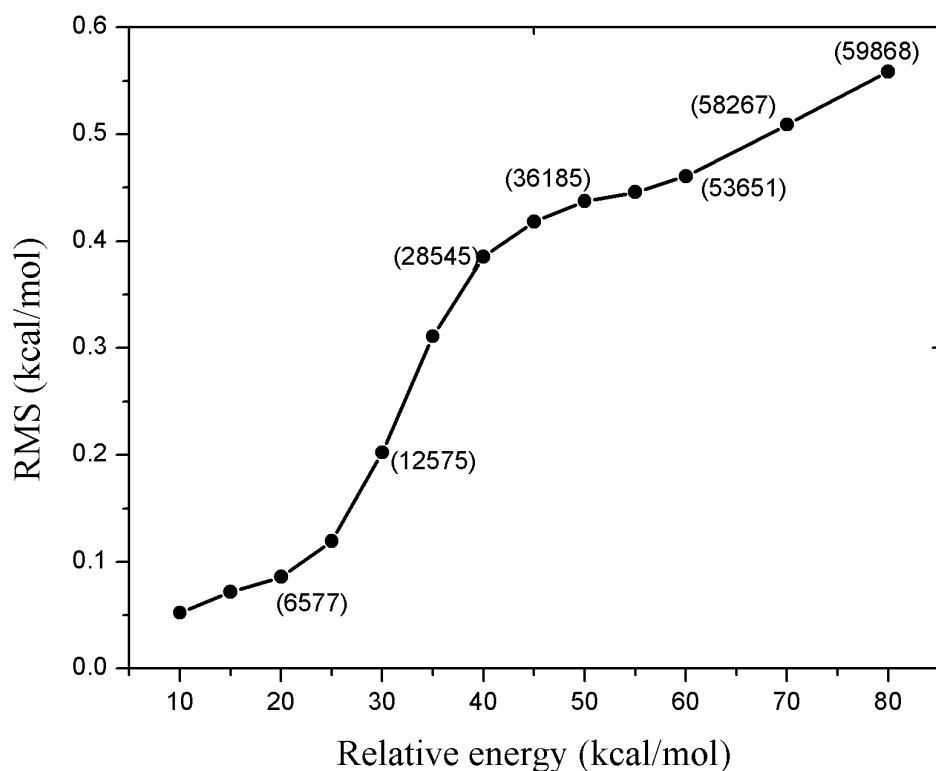
Figure 4.1: Root-mean-square (RMS) of the PES fitting error as a function of relative energy with respect to the global minimum. The numbers in parenthesis are the number of configurations in the energy range.

4.2.3 Properties of PES

Fifteen stationary points have been reported previously and confirmed in the present work. The comparison of energies of the stationary points from direct CCSD(T)-F12b *ab initio* optimization and from the fitted PES is shown in Figure 4.2. As seen, the PES is in very good agreement with the direct *ab initio* calculation. The PES reaction barrier of $H_2+CN\rightarrow H+HCN$ is 3.54 kcal/mol, and is in good agreement with the *ab initio* result as well as the deduced experimental value of 3-4 kcal/mol. The barriers for the association reactions R1 and R2 are 6.3 kcal/mol and 9.8 kcal/mol, respectively.
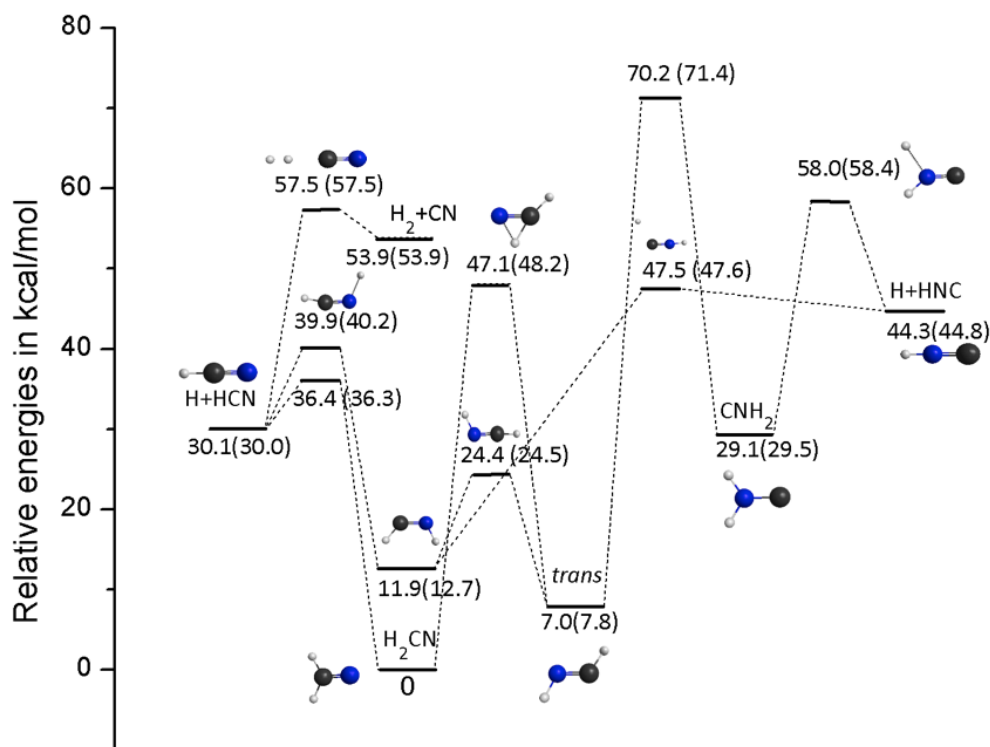
Figure 4.2:   Potential profile of all the stationary points on the PES. The energy outside the parentheses is the energy at the optimized geometry using the PES, and the value in the parentheses corresponds to the results of direct CCSD(T)-F12b calculation.

The harmonic frequencies and ZPE are calculated at the stationary points using the PES, and are compared with *ab initio* results, shown in Table 4.1. We observe very good agreement of the harmonic frequencies between the PES and *ab initio* calculation.

Table 4.1:   Harmonic vibrational frequencies ω_i (cm^{-1}) and harmonic ZPE (kcal/mol) of the indicated stationary points using the fitted PES and *ab initio* calculations.

Species		ω_1	ω_2	ω_3	ω_4	ω_5	ω_6	ZPE
H$_2$C+CN	PES	4383	2046					9.19
	ab initio	4385	2070					9.23
H$_2$C+CN→H+HCN	PES	3268	2141	568(e)	133(e)	661i		9.74
SP	*ab initio*	3214	2107	547(e)	106(e)	676i		9.47
HCN	PES	3459	2145	707(e)				10.0
	ab initio	3437	2131	732(e)				10.1
H$_2$C+CN→H$_2$CN	PES	3447	2063	930	740	587	1020i	11.1
SP	*ab initio*	3371	2021	910	721	520	1071i	10.8
H$_2$CN	PES	3071	3002	1684	1378	971	930	15.8
	ab initio	3061	2990	1680	1378	975	932	15.9
H+HCN→*cis*-HCNH	PES	3407	1997	882	763	502	1266i	10.8
SP	*ab initio*	3389	1983	768	699	526	1473i	10.5
cis-HCNH	PES	3585	2909	1737	1165	1141	961	16.4
	ab initio	3346	3004	1803	1034	901	862	15.7
trans-HCNH	PES	3844	3130	1798	1361	1097	954	17.4
	ab initio	3461	3052	1756	1198	977	913	16.2

As seen, the PES is especially accurate for stationary points relevant to the H$_2$+CN↔H+HCN reaction, which will be studied in detail in the future. Several studies have observed that CN is essentially a spectator mode,[53,59,60] demonstrating that CN distance and its vibration state change little during the reaction. A smooth plot of colinear H+HCN↔ H$_2$+CN

reaction is shown in Figure 4.3 by varying HH and CH distances and fixing CN distance at equilibrium.
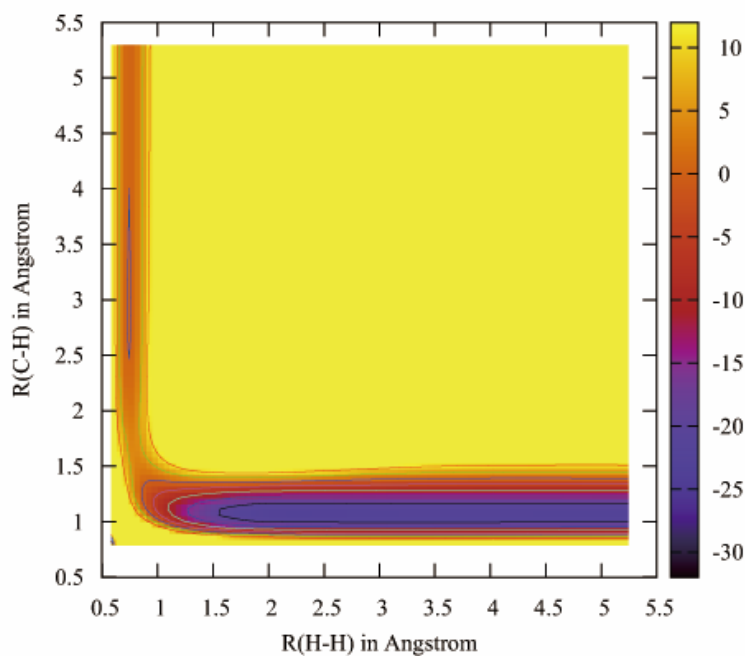
Figure 4.3: Contour plot of the H+HCN$\leftrightarrow$H$_2$+CN reaction using the PES (the energy of H$_2$+CN is set to zero). The C-H and H-H distances are changed in the plot, the C-N distance is fixed at equilibrium, and the symmetry is restricted to be colinear

4.3   Dynamic Simulations

QCT and CT calculations of the H+HCN association reactions were performed using the current PES. As usual, we determine whether or not a certain complex is initially formed based on the criterion of three turning points of the distance between the incoming

H atom and HCN. The calculations indicate that while it is easy to identify the deep complex H_2CN, it is not meaningful to distinguish the *trans*- and *cis*-HCNH isomers, because the interconversion is so rapid. Of course the initial isomer can be identified.

Standard normal-mode sampling[16] of the ground ro-vibrational state phase-space of HCN was used in the QCT calculations. For both CT and QCT calculations, the time step is 0.1 fs. The initial distance between H and HCN is 7 Å, and the number of steps is 1500. Reaction probabilities are calculated from 2000 trajectories for each impact parameter and collision energy.
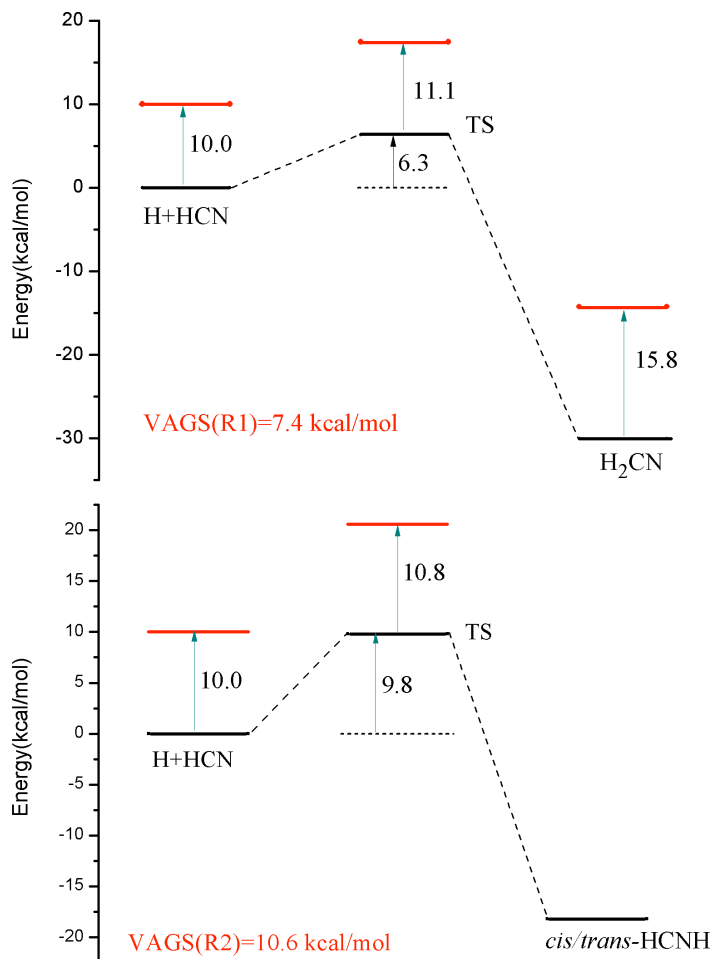
Figure 4.4:   Energies and geometries of the stationary points along the reaction paths of H+HCN→H$_2$CN and *cis/trans*-HCNH (the energy of H+HCN was set to zero). The red lines indicate the zero-point energies (ZPE)

To better understand the results of the QCT and CT calculations, we indicate the energies and barriers of the association reactions from H+HCN to H$_2$CN, R1, and *trans/cis*-HCNH, R2, complexes in Figure 4.4. The figure also shows the structure of saddle points, where the HCN is slightly bent for both R1 and R2. The standard harmonic vibrationally adiabatic ground state (VAGS) barriers are also given. Recall that these are the ener-

gies of SP plus the associated harmonic ZPEs minus the HCN ZPE. These ZPEs were obtained, as usual, in the harmonic approximation. From many previous dynamics calculations, we know that the VAGS barriers are useful estimates of the quantum and QCT threshold energies. (They are also central to a standard transition state theory treatment of the association rate constant.) There is no rigorous definition of the threshold energy for reaction with barriers. However, we adopt a frequently used one, namely the lowest collision energy where the reaction probability reaches 0.01. Based on many QCT calculations of reactions in the gas phase with barriers, the expectation is that the QCT threshold energy is close to the VAGS barrier. However, often because of a small amount of zero-point energy leak, the threshold energies are somewhat lower than this barrier. (Quantum threshold energies are almost always below the VAGS barrier, due to tunneling.) For the CT calculations (with no ZPE), our initial expectation was that the threshold energy for reaction R1 and R2 would be sharp and at the energy of the corresponding SP.

The collision energy dependence of the association probabilities of R1 and R2 for QCT and CT calculations for zero impact parameter is shown in Figure 4.5. First, we focus on the QCT results. As seen, the threshold energy of R1 is about 7 kcal/mol, in good agreement with the VAGS barrier of 7.4 kcal/mol. This also indicates a small amount of ZPE leak, which is a generally known issue in QCT calculation. The observed QCT threshold energy for R2 is roughly 10 kcal/mol, which agrees well with the VAGS barrier of 10.8 kcal/mol.
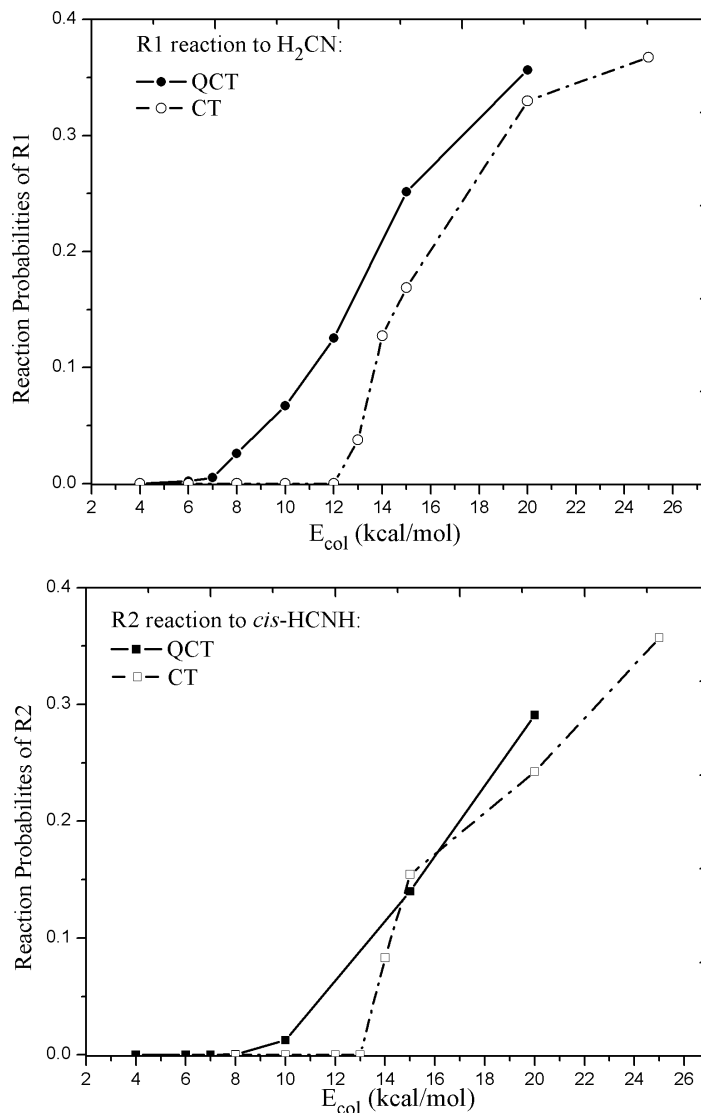
Figure 4.5: Reaction probabilities of R1 and R2 as a function of collision energy, with impact parameter equal to zero.

Next, we investigate the CT results. Recall that in this case, HCN is initially fixed at equilibrium geometry, without any vibration. Since ZPE is not included in the CT calculation, we expected the threshold energy to be exactly the SP energy. However, for both R1 and R2 reaction, the observed threshold energies are significantly higher. For R1,

the observed threshold is 12 kcal/mol, which is almost twice as large as the saddle point barrier of 6.3 kcal/mol. The same result appears for R2. For R2, threshold energy of CT is about 13 kcal/mol, much larger than the saddle point barrier of about 9.8 kcal/mol.

To investigate the large differences of threshold energies in the CT and QCT calculations, we consider the reaction R1 in more detail. Specifically, we calculated two relaxed one-dimensional potentials that are of relevance to the QCT and CT reactions. For the QCT calculation the relevant path is a fully relaxed one where the potential is minimized as a function of R, the distance of H to the center of mass of HCN. The second path is one where the HCN geometry is fixed at the equilibrium structure. These two paths are shown in Figure 4.6. As seen, the fully relaxed path connects the reactants to the R1 SP and then finally to the H_2CN global minimum. The barrier on this path is just the saddle point energy, as expected. The QCT threshold energy is totally consistent with this barrier on this path. As already noted, the HCN reactant is slightly bent at the barrier and this bending is easily achieved using QCT sampling of initial conditions. By contrast, the constrained path displays a ridge at about 12 kcal/mol, which is in good accord with the observed CT threshold energy. Note that this ridge develops at a smaller value of R than that of SP.
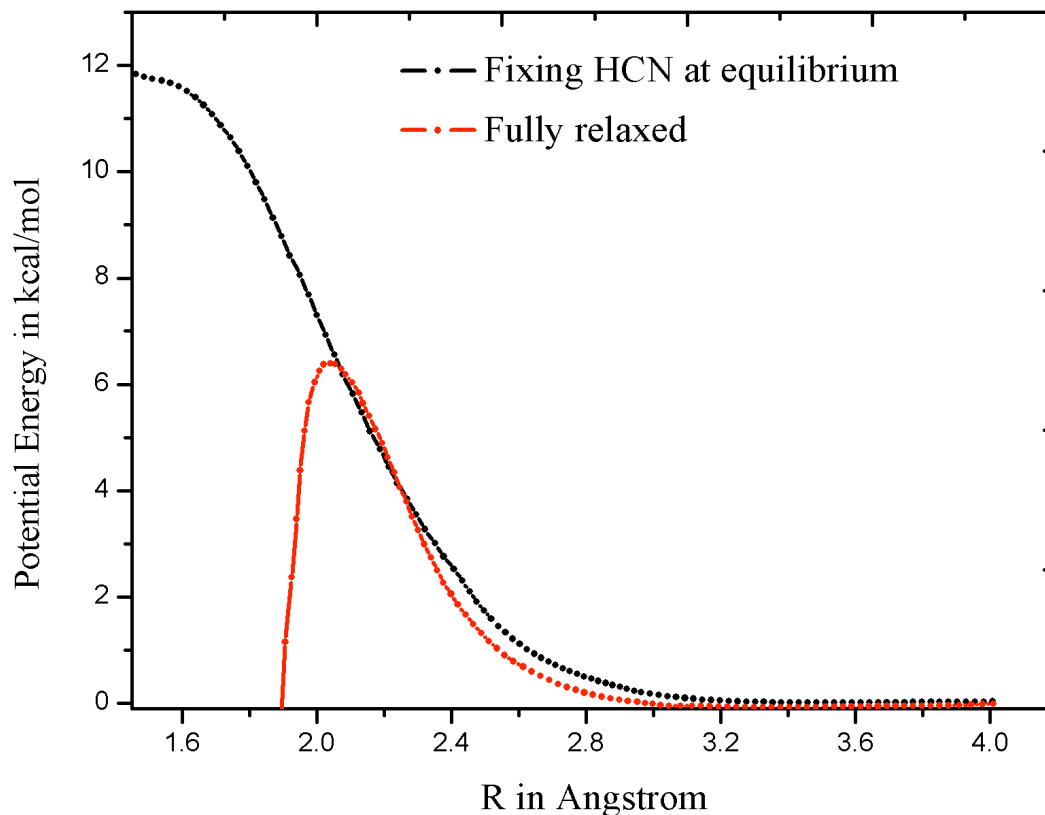
Figure 4.6: Relaxed potential energy cut for H-HCN (the energy of H+HCN was set to be zero). R is the distance between H and the center of mass of HCN. For the red curve, the energy is achieved by relaxing all the other internal degrees of freedom. For the black curve, HCN is fixed at the equilibrium, and the orientation between H and HCN is relaxed.

Clearly in an actual CT trajectory the H_2CN well is accessed at collision energy above 12 kcal/mol, but we believe this occurs after first visiting this ridge region at roughly 12 kcal/mol. To verify this we examined a CT trajectory at collision energy of 13 kcal/mol, where the reaction probability of R1 is not zero but small. We monitored $R(t)$, the HCN bond angle, $\theta(t)$, and the potential, $V(t)$ of the CT trajectory, as shown in Figure 4.7. As seen, as R decreases to roughly 3.5 Å, θ remains at the equilibrium value of 180°. As the

H atom approaching, the potential energy keeps increasing until reaching barrier height of about 10 kcal/mol, which is smaller than the 12 kcal/mol threshold energy. θ decreased even as the potential remains flat and R also remains flat. This is the "ridge. Notice that the value of R at the beginning of the ridge is 1.6 Å, which is in good agreement with this value at the start of the plateau region of the CT potential cut in Figure 4.6. After entering the ridge region, there are, not surprisingly, some distortion of HCN and in fact a slight increase in R, as the H_2CN potential well is accessed at roughly 7.5 fs. Based on this result as well as the potential cuts in Figure 4.6, we assign a critical value of R for reaction to occur for the CT calculations of roughly 1.6 Å. This is less than the value R at the SP, which is roughly 2 Å.
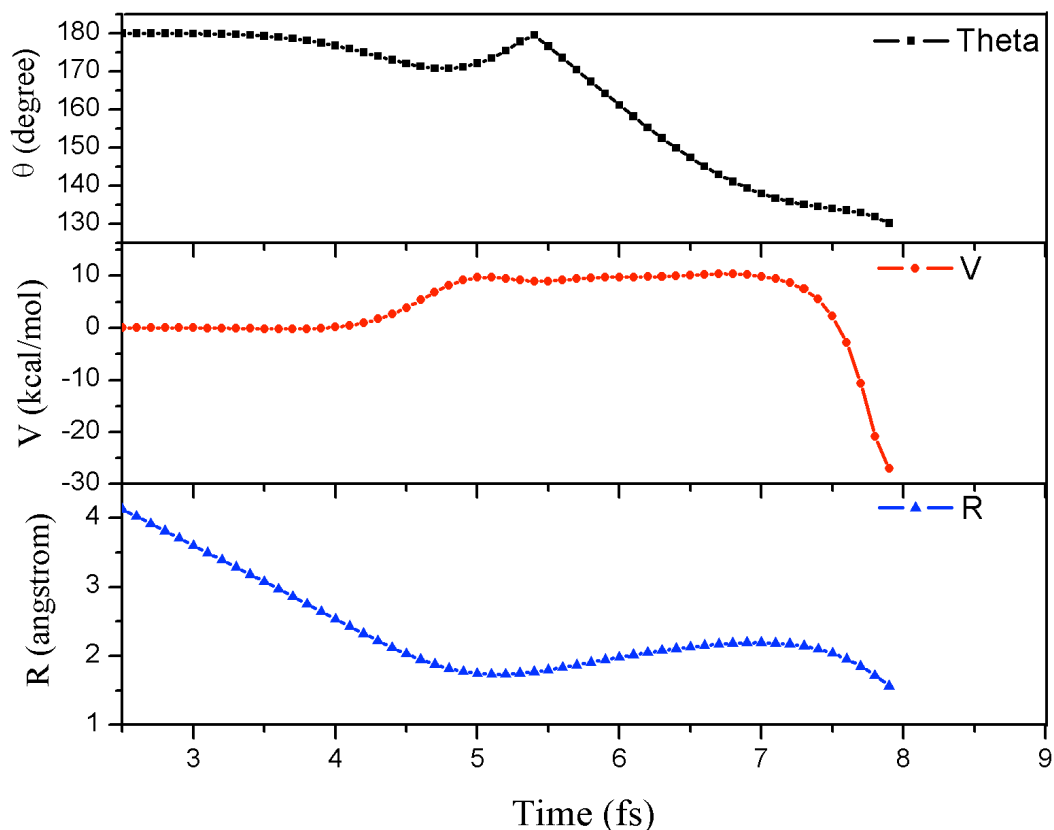
Figure 4.7: The tracking of classical trajectory (CT) as a function of reaction time at collision energy of 13 kcal/mol. R is the distance between the incoming H atom and the center of mass (COM) of HCN; V is the potential energy and θ is the bent angle of HCN.

We then further tested the assignments of the critical values of R for the QCT and CT calculations by investigating the reaction probabilities as a function of impact parameter at a collision energy well above the threshold energies. Here, we use a simple, spherically symmetric textbook model to predict the maximum impact parameter for a reaction with well-defined critical distance for reaction to occur, which we denote generically as R_b. If we make the reasonable assumption that the effective barrier at R_b is the sum of the potential V_b plus the centrifugal potential, then using $E_{col} = V_b + b^2 E_{col}/R_b^2$, where E_{col} is

the collision energy, it is trivial to get the following equation for the maximum reaction impact parameter b_{max}, i.e, to surmount the effective barrier.

$$b_{max} = R_b\sqrt{(1 - V_b/E_{col})} \tag{4.2}$$

$b_{max} \approx R_b$ if $E_{col} \gg V_b$. Aside from this limit we need to know R_b and V_b to predict b_{max}. Considering that R_b is larger and V_b is smaller for QCT than for CT, we can get an immediate qualitative conclusion that b_{max}-QCT is larger than the b_{max}-CT, where the meaning of the new notations should be obvious. A quantitative examination of this conclusion is shown in Figure 8 for E_{col} of 20 kcal/mol. As predited, b_{max}-CT is smaller than b_{max}-QCT. The latter is roughly 1.8 Å, and agrees well with the calculated value of 1.75 Å from the above equation with the QCT parameters inserted into it. The prediction is 1.0 Å using CT parameters of 1.6 Å for R_b and 12 kcal/mol for V_b, which is not in agreement with observed b_{max}-CT of 1.6 Å. This is not surprising given that instead of a well-defined barrier and critical distance for the CT calculations there is a broad ridge. Thus, while the above equation works quite well for the QCT case, it only works qualitatively for the CT case. Nevertheless, even a correct qualitative prediction does add further evidence to the conclusion that the CT dynamics is not governed by the SP.
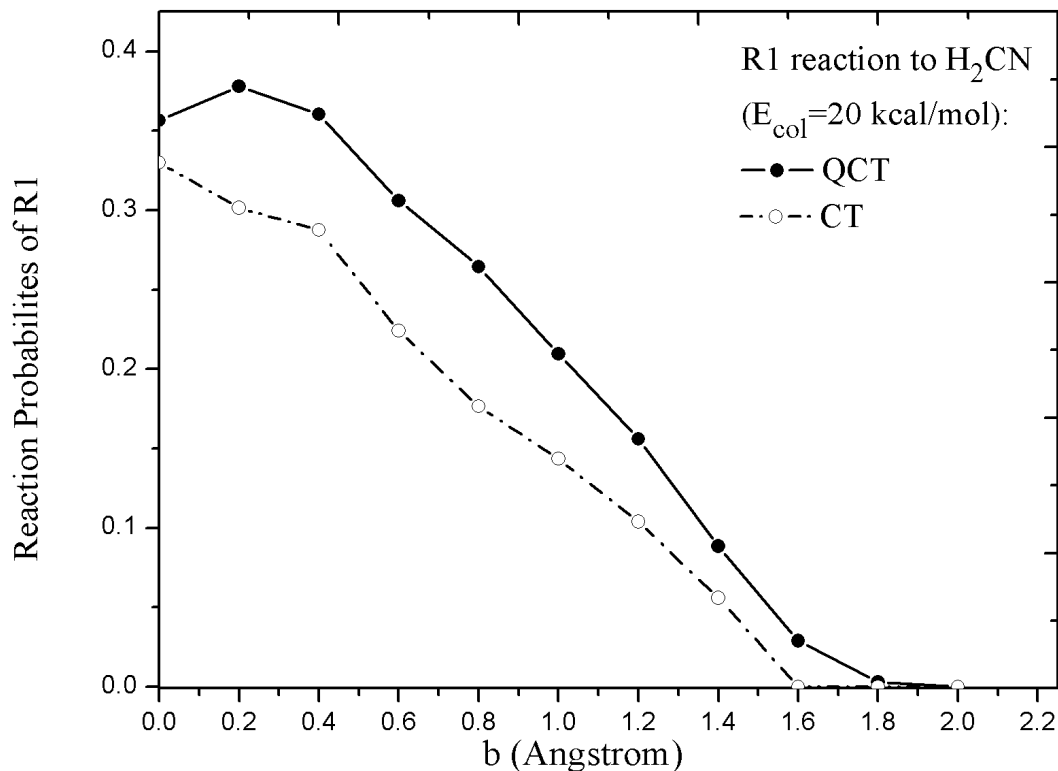
Figure 4.8:   Reaction probabilities of R1 from the CT and QCT calculations as a function of the impact parameter at E_{col} =20 kcal/mol

Similar analysis is performed for the R2 reaction forming the *trans-* and *cis-*HCNH, and we find analogous results. The geometry and energy of R2 SP have been shown in Figure 4.4. The barrier does indeed govern the QCT threshold, as noted already. Interestingly, instead of the usual mechanistic picture where the *cis-*SP is crossed first followed by isomerization to *trans-*HCNH, we noticed some trajectories initially directly formed the *trans* isomer when examining QCT trajectories. To investigate this, we determined two relaxed paths from the *trans-* and *cis-*HCNH to H+HCN respectively, as shown in Figure 4.9. As seen, the two curves are virtually superimposable from the pre-barrier region to the asymptotic region. Thus, the labeled *cis-*SP is evidently the saddle point

for both isomers. However, we do note that the isomerization from H_2CN to *trans*-HCNH
is difficult because of the high barrier, as seen in Figure 4.2.
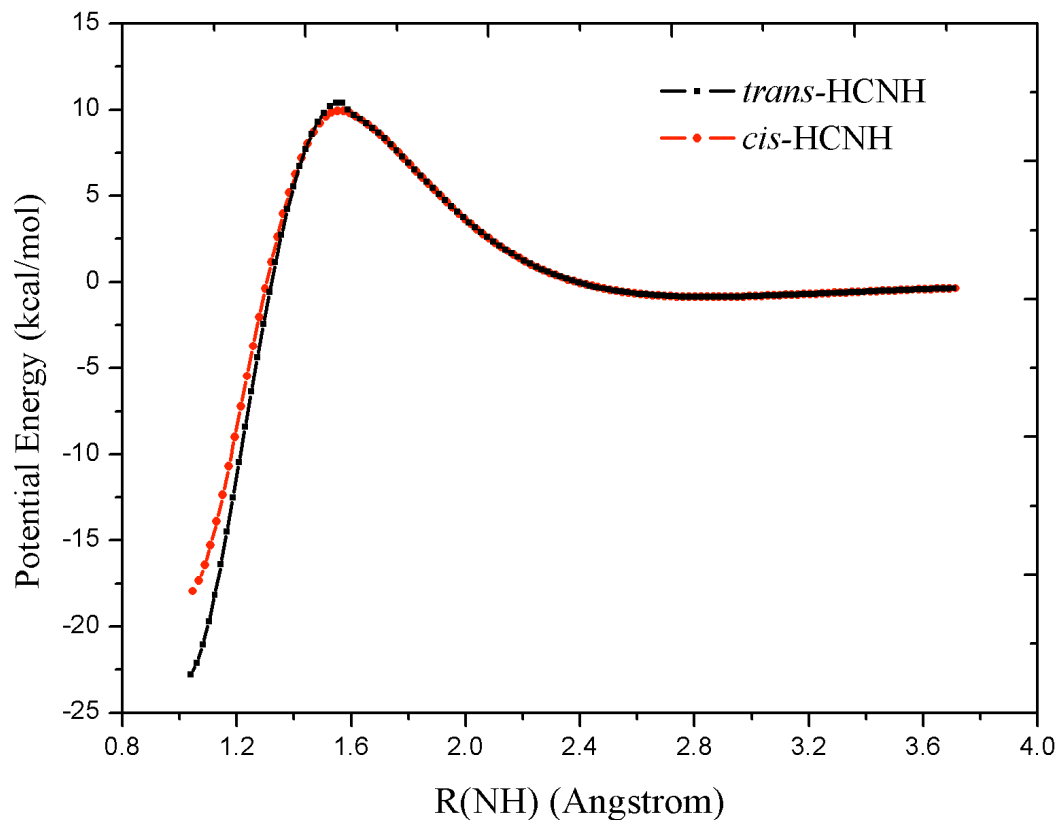
Figure 4.9: Relaxed potential energy curves from *trans/cis*-HCNH as a function of NH
distance (the energy of H+HCN was set to zero). The red curve starts from cis-HCNH;
the black curve starts from trans-HCNH. The NH distance is increased and the energy
is relaxed with respect to all the other degrees of freedom

Finally, we note that at relatively high collision energies of about 15 kcal/mol, we
observed trajectories where the two H atoms can exchange. This undoubtedly happens
at lower collision energies too. However, because we did not propagate the trajectories
long enough for subsequent dissociation of the energetically excited complexes we did not

observe this.

4.4   Summary and Conclusion

We presented a new global full-dimensional potential energy surface for the H_2CN system. The PES was constructed by fitting roughly 60,000 CCSD(T)-F12b/aVDZ electronic energies. The permutation invariance of the two H atoms is included using the monomial symmetrization method. The PES totally covers 15 stationary points, and is especially accurate along the $H_2+CN \rightarrow H+HCN$ reaction path. Excellent agreement is achieved for the energies and normal-mode analysis frequencies comparison between the PES and the direct CCSD(T)-F12b calculations

QCT and CT calculations of the association reactions of H+HCN were performed using the PES. We calculated the reaction probabilities of association reactions as a function of collision energy, and the impact parameter. QCT and CT results show large differences in the threshold energy, with CT giving larger threshold energy. In addition, at a given collision energy the CT calculations give a smaller maximum impact parameter for reaction than the QCT ones. These differences were analyzed in detail and it was concluded that these differences are due to different barriers of relevance to the QCT and CT calculations. In the case of the QCT calculations the saddle point barrier is the relevant barrier. This is the usual QCT result, consistent with many QCT calculations of reaction dynamics. The new result of the significantly higher threshold energy is seen in the CT calculations.

For this polyatomic reaction the origin of this difference is evidently the distorted geometry of the reactant HCN at the saddle point. In the CT calculations, with no initial zero-point energy, HCN evidently remains colinear as H atom approaching, and

does not distort to "in time" to achieve the saddle point geometry. By contrast, the QCT calculations, with initial ZPE in the HCN, do sample bent configuration of the HCN and thus accessing the SP geometry does occur easily. The fact indicates the importance of including the ZPE in reaction dynamics studies. In addition, the reaction channel from H+HCN directly to *trans*-HCNH is discussed in detail for the first time, which shows the same saddle point with the reaction to *cis*-HCNH.

4.5   PES Construction of Similar Systems

As known, H_2 is the most abundant molecule in the interstellar medium, and the interaction and reactions between H_2 and other species play important roles in modeling the chemistry of diffuse clouds. The CN radical and CO molecule are two abundant molecular species in the interstellar environment. The interactions of H_2-CN and H_2-CO have been studied many times in the literature. Different from the H_2CN reaction studies mentioned above, here we are mainly interested in the long range interaction between two species instead of the total potential energy. Besides, because the systems are usually in very cold interstellar environment, we require quite high accuracy of the constructed PES. The process for constructing the interaction PES will be briefly discussed using the H_2-CO case.

To construct the PES, the computations were performed on a six-dimensional (6D) grid using Jacobi coordinates. R is the distance between the center of mass of CO and H2. r_1 and r_2 are the bond lengths of CO and H_2, respectively. θ_1 is the angle between r_1 and R, θ_2 is the angle between r_2 and R, and ϕ is the out-of-plane dihedral or twist angle. In the potential energy computations, the bond lengths are taken over the ranges $1.7359 \leq r_1 \leq 2.5359$ bohr and $1.01 \leq r_2 \leq 1.81$ bohr, both with a step-size of 0.1 bohr.

For R, the grid extends from 4.0 to 18.0 bohr with step-size of 0.5 for $R < 11.0$ bohr and 1.0 for $R > 11.0$ bohr. All angular coordinates were computed with a step-size of 15° with $0° \leq \theta_1 \leq 360°$ and $0° \leq \theta_2, \phi \leq 180°$. Additional points were added in the region of the van der Waals minimum.

The H_2-CO has the same symmetry group with H_2CN, therefore the same monomial symmetrized basis function can be used for the PES fitting of H_2-CO. In total, 398,218 configurations are used for the fitting, and the RMS error of the PES is 14.22 cm^{-1}, which is by far the most accurate PES for the H_2-CO system. The PES is used in the exact, full-dimensional dynamics computations for the rovibrational quenching of CO due to H_2 impact. The further details of PES construction and quantum dynamics calculations can be found in Ref 10. Using the similar approach, we built the surfaces for the interaction energy of H_2-CN and H_2-SiO systems as well, and details are skipped here.

Chapter 5

Unimolecular Dissociation of *syn*-CH$_3$CHOO

Ozonolysis of alkenes is an important class of atmospheric reactions.[61] The ozonolysis is believed to proceed through a 1,3-cycloaddition of O$_3$ to the double bond of alkenes to produce a primary ozonide, which decomposes to a carbonyl compound and carbonyl oxide, known as Criegee intermediates.[62] The energized Criegee intermediates undergo unimolecular decay forming OH and vinoxy radicals, collisional stabilization, and/or bimolecular reactions with water, NO$_2$, SO$_2$, organic acids, or other atmospheric species.[63–66] Ozonolysis of internal alkenes, such as trans-2-butene producing the CH$_3$CHOO Criegee intermediate, contribute significantly to the atmospheric OH budget as a result of their high OH yield.[67,68]

Recent experiments have focused on these important intermediates. The simplest Criegee intermediate, CH$_2$OO, has been directly detected in the gas phase.[69–71] The simplest alkyl-substituted Criegee intermediate, which has two conformers *syn*- and *anti*-CH$_3$CHOO, were directly observed in the gas phase very recently.[72] The CH$_3$CHOO

intermediate is thoroughly studied in our researches, including the dynamic simulations of the unimolecular dissociation of *syn*-CH_3CHOO and the vibrational analysis of both *syn*- and *anti*- CH_3CHOO isomers.

In this chapter, the unimolecular dissociation of a prototypical Criegee intermediate, a key step in the non-photolytic generation of atmospheric OH radicals, is characterized through the translational and internal energy distributions of the OH and vinoxy products. We have collaborated with experimental studies to understand the dynamic details. Experimentally, CH overtone excitation of CH_3CHOO is utilized to drive 1,4-H atom transfer and isomerization to vinyl hydroperoxide prior to dissociation. The kinetic energy release to OH products is ascertained through velocity map imaging based on a novel OH ionization scheme. Theoretically, quasi-classical trajectories are performed on a new full-dimensional, *ab initio* potential energy surface, and initiated from several critical configurations along the reaction pathway.

5.1   Introduction

Alkene ozonolysis is the principal non-photolytic source of atmospheric OH radicals, which initiate the oxidative breakdown of most trace species in the troposphere.[73] This is the dominant source of OH radicals in the nighttime and accounts for about 1/3 of the OH radicals in the daytime.[73–76] The present study examines the unimolecular dissociation pathway of a prototypical alkyl-substituted Criegee intermediate, specifically the more stable *syn*-conformer of CH_3CHOO, leading to OH radical products.[72,77,78] This is achieved using a combination of experimental and theoretical methods to characterize the kinetic energy release and internal energy distributions of the OH and vinoxy (CH_2CHO) products. The experiments are conducted using a novel, state-selective ionization scheme

for OH radicals[79] coupled with its initial application in velocity map imaging (VMI) to ascertain the angular and velocity distributions of the OH products. The theoretical approach is based on running ensembles of quasi-classical trajectories (QCT) from different initial configurations, all using a new, full dimensional *ab initio* potential energy surface (PES). Combining these challenging experimental and theoretical studies provides a detailed investigation of the dissociation dynamics of *syn*-CH$_3$CHOO, the key step for non-photolytic generation of OH radicals in the atmosphere.

5.2 Potential Energy Surface

The calculations are performed on a newly constructed PES. The PES for the dissociation dynamics of *syn*-CH$_3$CHOO system is quite challenging due to the high dimensionality and the multi-reference character in the region of dissociation to OH + vinoxy. The bound region of *syn*-CH$_3$CHOO is well described using a single-reference method,[13] and the same method is utilized for the isomerization TS and VHP regions. The energies are calculated using the CCSD(T)-F12b method with the aug-cc-pVDZ basis for the C and O atoms and the cc-pVDZ basis for H atoms (HaDZ),[54,55] using the MOLPRO 2010 package.[58] As noted previously,[80] a multi-reference method is needed for the dissociation from VHP to OH and vinoxy radicals. Thus, energies were obtained using CASPT2/cc-pVDZ theory with an active space of up to 12 electrons in 10 orbitals employed, as implemented in MOLCAS package.[81] Finally, the CASPT2 energies were shifted with respect to the CCSD(T)-F12b results using the energy of fragments (which were obtained separately using CCSD(T)-F12b/HaDZ) for the fitted PES. As a result, the exit channel region is almost certainly less accurate than other regions of the PES.

The *ab initio* points are efficiently sampled along the dissociation channel to provide

accurate description of the PES. Most geometries are determined by running classical direct dynamic starting from different stationary points with B3LYP/pVDZ methods, which excludes the dissociation region. Then CCSD(T)-F12b/HaDZ calculations were carried out for the single-reference points and fitted to generate a preliminary PES. Since the preliminary PES does not have enough sampling in the dissociation region, it gave unreasonable energies whenever entering the multi-reference area. The geometries in this region can be easily determined by running classical trajectories using the preliminary PES. Additional geometries in the multi-reference region were chosen and energies calculated using the CASPT2 method. The calculated CASPT2 results were shifted according to CCSD(T)-F12b energies and added to the dataset for PES fitting. After repeating this procedure several times, the PES can achieve an accurate description of all the regions in the decomposition channel.

In total, 157,278 points were calculated with energies up to 70 kcal/mol relative to then *syn*-CH$_3$CHOO minimum, including 22,797 CASPT2 energies and 134,481 CCSD(T)-F12b energies. The PES is 18 dimensional, and is invariant with permutation of like atoms. The invariant polynomial fitting method is employed,[3] in which the polynomials are functions of Morse variables, given by $y_i = \exp(-r_i/\alpha)$, with α fixed at 2.0 bohr. The maximum total power of the fitting polynomials is 5, and the fitting root mean square (RMS) error is 61.5 cm^{-1}. The fitting RMS error in different energy ranges is given in Figure 5.1.
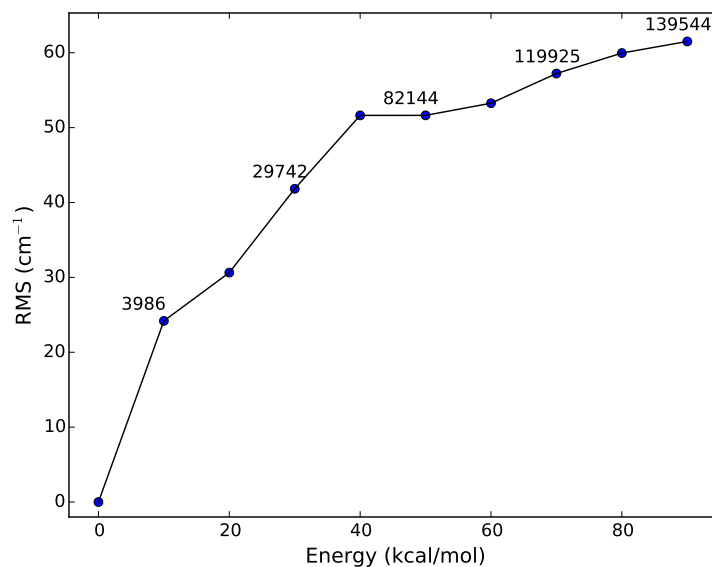
Figure 5.1: Root mean square error of the fitted potential energy surface vs. relative energy with respect to vinyl hydroperoxide. The values in the figure are the number of configurations in the corresponding energy range.

The optimized geometries, electronic energies, and harmonic frequencies of stationary points are computed using the PES. The electronic energies of stationary points as well as their zero-point energies (ZPE) are given in Table 5.1. A comparison of harmonic frequencies between the PES and direct CCSD(T)-F12b results are given in Table 5.2. As seen, there is excellent agreement between the PES and direct *ab initio* calculations.

Table 5.1: Potentials and harmonic zero-point energies (ZPE) of stationary points computed using the potential energy surface (PES), and the comparison with *ab initio* calculations. Energies are given with respect to *syn*-CH$_3$CHOO in kcal/mol

	Energy		ZPE	
	PES	*ab initio*	PES	*ab initio*
syn-CH$_3$CHOO	0.00	0.00	37.15	37.22
TS	18.66	18.68	34.87	35.03
CH$_2$=CHOOH	-19.25	-19.25	37.27	37.37
OH+CH$_2$CHO	6.82	6.86	31.70	32.00

An overview of stationary points and pathways describing the dissociation of *syn*-CH$_3$CHOO to OH + CH$_2$CHO products is shown in Figure 5.2. There is a transition state (TS) separating syn-CH$_3$CHOO from vinyl hydroperoxide (CH$_2$=CHOOH, VHP).[77] This TS has a 5-membered ring-like structure associated with intramolecular 1,4-H atom transfer and isomerization to VHP. VHP then undergoes O-O bond cleavage to form OH + vinoxy products, although not via a simple, barrierless O-O bond breaking process, i.e., a monotonic increase in potential starting from VHP to the products along a path where the O-O bond length increases. There is a submerged, first-order saddle point (submerged SP), as reported previously, and an associated shallow, constrained (O-O bond length fixed) minimum in the exit channel.[80] A second pathway is also indicated; this is a "least-motion path" starting from VHP to a positive-energy barrier (second-order SP) and a stable product complex in the exit channel. QCT calculations of the dissociation dynamics are initiated from each of these configurations, specifically isomerization TS, VHP, and also from the submerged SP and positive barrier in the exit channel. The latter

Table 5.2:   Harmonic frequencies (cm^{-1}) of stationary points computed using the potential energy surface (PES), and the comparison with *ab initio* calculations.

mode	*syn*-CH$_3$CHOO		TS		CH$_2$=CHOOH		OH+CH$_2$CHO	
	PES	ab initio	PES	ab initio	PES	ab initio	PES	ab initio
ν_1	206	202	1671i	1702i	164	150	425	413
ν_2	301	308	458	494	230	237	501	500
ν_3	441	448	492	534	337	335	710	728
ν_4	680	678	674	722	597	617	946	969
ν_5	731	721	796	750	703	702	959	970
ν_6	930	922	817	860	825	841	1136	1160
ν_7	980	978	925	895	887	880	1374	1404
ν_8	1044	1031	951	968	965	961	1470	1477
ν_9	1107	1115	1042	1034	993	974	1606	1608
ν_{10}	1283	1317	1187	1211	1181	1162	2914	2977
ν_{11}	1405	1397	1311	1278	1289	1317	3083	3155
ν_{12}	1457	1449	1375	1350	1369	1393	3232	3277
ν_{13}	1461	1467	1536	1493	1465	1430	3757	3745
ν_{14}	1546	1527	1622	1555	1673	1695		
ν_{15}	2953	3029	1676	1859	3137	3182		
ν_{16}	3101	3085	3141	3095	3189	3204		
ν_{17}	3143	3161	3152	3194	3281	3288		
ν_{18}	3216	3204	3240	3210	3783	3777		

calculations are done to determine the relevance of these possible exit channel pathways in the dynamics run from the TS and VHP configurations.
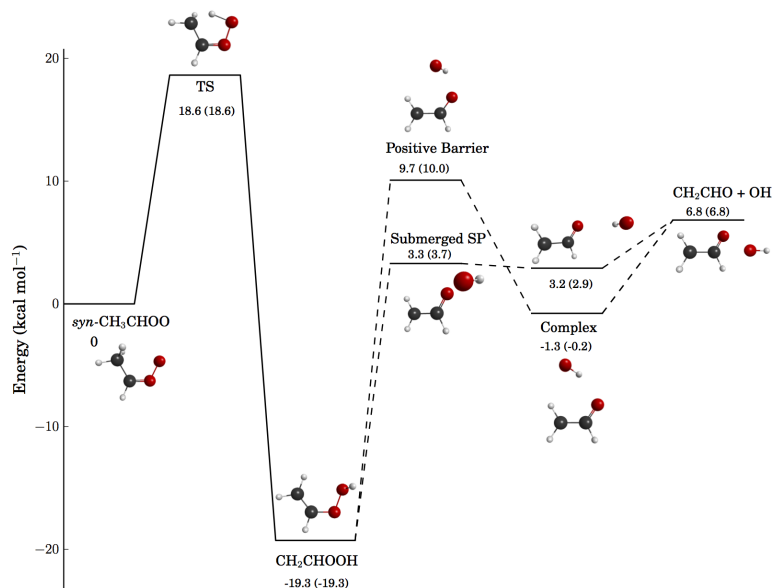
Figure 5.2: Energy profile of stationary points along the reaction coordinate from *syn*-CH₂CHOO to OH + vinoxy (CH₂CHO) radical products. The reaction proceeds over a transition state (TS) associated with 1,4-H atom transfer and isomerization to vinyl hydroperoxide (CH₂=CHOOH, VHP), followed by passage through an exit channel region with submerged saddle point (SP) or positive barrier and associated product complex prior to dissociation. The energies (kcal/mol) obtained at optimized geometries on the PES are in very good agreement with values in parenthesis taken directly from *ab initio* calculations (CCSD(T)-F12b or CASPT2).

A submerged first-order saddle point (submerged SP) was located on the PES that is very similar to one reported in the literature.[80] A 1-D potential energy curve is obtained by starting from the submerged SP and increasing the O-O distance towards fragments and decreasing it towards the VHP minimum, and then minimizing the energy with respect to other degrees of freedom. The potential along this constrained path is shown in Figure 5.3, which includes a shallow minimum also indicated in Figure 5.2. An additional

1-D potential curve along a constrained pathway is shown in Figure 5.3. This is obtained by starting at the VHP minimum and increasing the O-O distance along the bond axis vector, and again minimizing the potential with respect to the other degrees of freedom. This leads to a potential curve with a positive energy barrier (a second order saddle point) followed by a stable, i.e., true minimum, product complex.

The pathway through/near the submerged SP is more relevant based on running full dimensional dynamics. As a result, direct CASPT2 calculations are performed using the geometries in the submerged SP pathway to test the PES. The comparison is shown in Figure 5.3 where good agreement is seen.
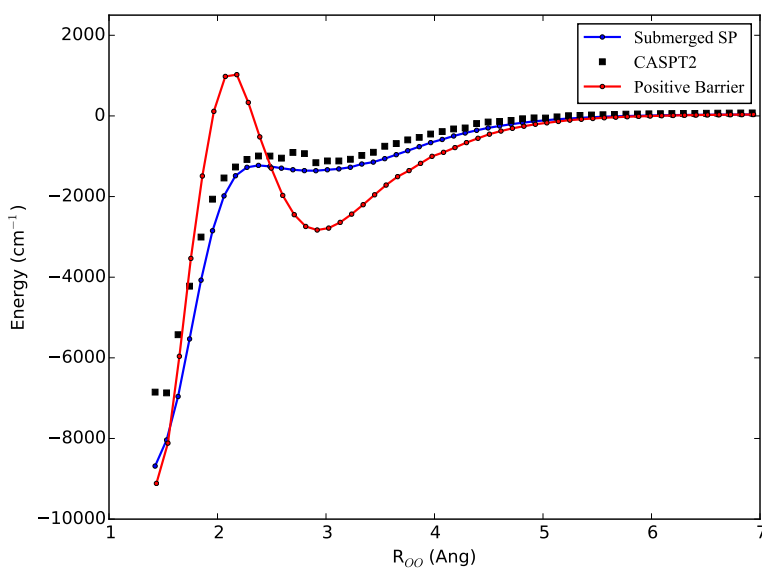
Figure 5.3:   1-D potential energy curves that pass through the positive barrier (red) and submerged SP (blue) from the VHP well to the OH + vinoxy products. The positive barrier curve is optimized by restricting the O-O vector and relaxing all other degrees of freedom starting from the VHP minimum. The submerged SP is a first-order saddle point optimized using the PES. The minimum energy path is optimized from the submerged SP to products and also to the VHP well. The points (black squares) are the direct CASPT2 energies using the optimized geometries in the submerged SP cut.

Clearly then, the actual, multi-dimensional dynamical pathway(s) to OH + vinoxy products following excitation of *syn*-CH$_3$CHOO to the transition state region is not obvious a priori based on the schematic reaction pathways shown in Figure 5.2. On one hand, the products could be formed directly via simple unimolecular dissociation after surmounting the TS barrier. In this case, one would anticipate that most of the available energy would be released as translational energy of the recoiling fragments.[82] On the other hand, the deep VHP well separating the TS from products could cause energy randomization and possibly result in a long-lived VHP intermediate prior to decay to products.[83,84] An intriguing additional factor to consider is the presence of exit channel barriers and associated product minima. The present study focuses on the outcomes, specifically the release of excess energy to internal and translational degrees of freedom, following unimolecular decay of syn-CH$_3$CHOO from an experimental and theoretical perspective as a means of elucidating the dynamical pathway(s) to OH products.

5.3   Dynamic Studies in Experiment and Theory

Experimentally, IR excitation of *syn*-CH$_3$CHOO in the CH overtone region is utilized to initiate unimolecular dissociation to OH + vinoxy radical products.[77] The present experimental study focuses on IR excitation at 6081 cm^{-1}, which provides sufficient energy to surmount or tunnel through the barrier for 1,4-H atom transfer and isomerization to VHP, and the resultant dissociation to OH products that are detected. The 6081 cm^{-1} feature was previously assigned as a zeroth-order bright state of *syn*-CH$_3$CHOO with in-plane carbonyl oxide CH stretch (ν_1) character. This feature involves CH stretch of the H atom in the anti-position relative to the carbonyl oxide group.

The QCT method is employed to study the unimolecular decay dynamics of *syn*-

CH$_3$CHOO from a complementary theoretical perspective. The initial energy for the QCT simulation is chosen to be 6000 cm^{-1} above the zero-point energy (ZPE) of *syn*-CH$_3$CHOO to model the experimental study. As shown in Figure 5.2, the TS for isomerization from *syn*-CH$_3$CHOO to VHP is 18.6 kcal/mol and ZPE correction lowers the barrier to 16.2 kcal/mol (5663 cm^{-1}). This agrees well with an effective barrier of $\leq$ 16.0 kcal/mol (5603 cm^{-1}) established experimentally based on the lowest-energy feature observed that leads to OH products.[77] As a result, the energy available to the fragments is about 5500 cm^{-1} in both the theoretical and experimental studies. In order to reduce the computational expense, QCT calculations are not initiated from *syn*-CH$_3$CHOO. Instead, trajectories are initiated from the TS configuration, the VHP minimum energy structure, and the two exit channel geometries indicated in Figure 5.2. The total angular momentum is zero for all trajectories.

Standard normal-mode sampling[17,18] was used to prepare the initial states of TS. To perform the normal-mode sampling at TS, the harmonic ZPE was given for each normal mode, except the imaginary frequency mode, and extra energy (the total energy minus the TS barrier height plus the local ZPE) of 337 cm^{-1} was given as translation along the imaginary frequency mode in the direction forming VHP. In addition, large ensembles of the trajectories were initiated from the VHP minimum energy configuration. For trajectories starting from VHP, micro-canonical sampling[19] was used to distribute total energy between the vibration modes of the VHP. The trajectories were propagated for a maximum of 60,000 steps with 0.1 fs time step (6 ps). More than 80% trajectories starting at TS dissociated in 6 ps.

About 40,000 trajectories were obtained that dissociate to OH and vinoxy products from each set of initial configurations. The relative translational energy, and the rotational and vibrational energies of OH and vinoxy radicals were calculated using these trajec-

tories. The classical vibrational energies of the fragments were examined to see if they were below the respective anharmonic ZPEs. The anharmonic ZPE of OH was evaluated as 1865 cm^{-1} using the discrete variable representation (DVR) method. The anharmonic ZPE of vinoxy was evaluated as 9279 cm^{-1} using the MULTIMODE program.[30] At total energy of the simulations, which is in the threshold region, most trajectories yield OH products with less than their ZPE. This violation of ZPE can have significant consequences on the translational energy distribution and thus such trajectories, roughly 90% of the large ensembles of trajectories, were discarded. Figure 5.4 shows the total kinetic energy release (TKER) distributions arising from all trajectories originating at the TS with normal mode sampling and the subset of trajectories where the OH and vinoxy products have at least their respective zero-point energies. The TKER distribution resulting from all trajectories extends to unphysically large values (beyond the 5500 cm^{-1} of available energy) and is broader than that with the hard-ZPE constraint. Qualitatively, the TKER distributions with and without the hard-ZPE constraint are in good accord at low energies (below 2000 cm^{-1}) through the peak of the distribution. As expected, imposing the hard-ZPE constraint yields much better agreement with the experimental results. After applying this hard-ZPE constraint, 4399 trajectories starting from TS using normal-mode sampling and 4624 trajectories starting from VHP using micro-canonical sampling were included in the following analysis.
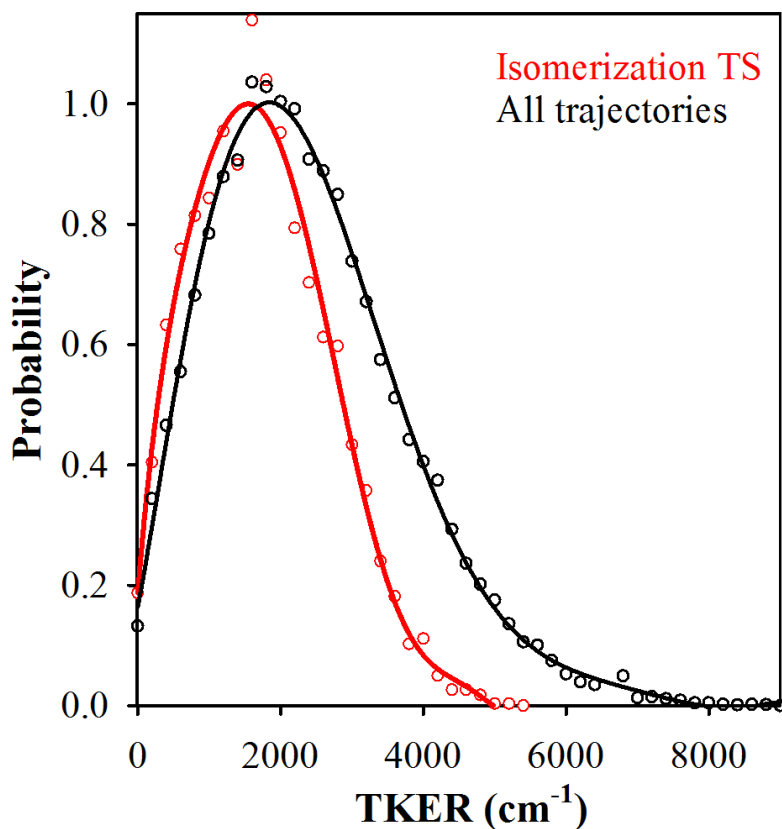
Figure 5.4:   Relative translational energy distribution between the OH and vinoxy fragments resulting from QCT calculations starting from the isomerization TS configuration using normal mode sampling. Shown are the total kinetic energy release (TKER) distributions arising from all trajectories (black) and the subset of trajectories where the OH and vinoxy products have at least their respective zero-point energies (red).

The role of the two barriers in the exit channel is explored by initiating ensembles of trajectories from these configurations. Micro-canonical sampling is applied at the two barriers with the total energy (6000 cm^{-1} relative to the ZPE of syn-CH$_3$CHOO) randomly distributed in the vibration modes. More than 80,000 dissociation trajectories are obtained for QCT starting at each barrier. After applying the hard-ZPE constraint, 3188

and 6360 trajectories starting at the positive barrier and submerged SP, respectively, are used for the analysis.
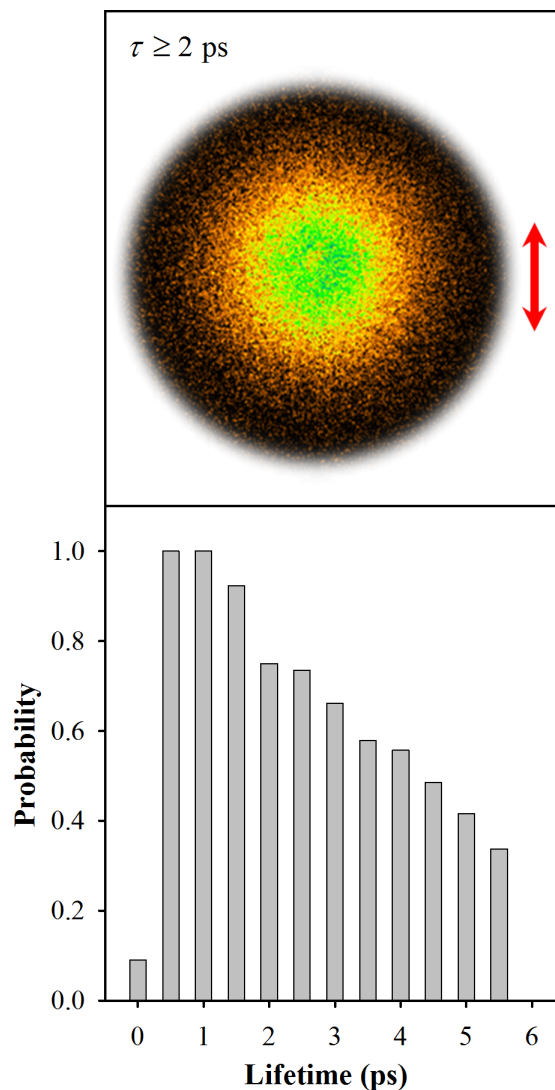
Figure 5.5:   Lifetime for OH radical production from velocity map imaging and trajectory calculations. a, Raw VMI of OH products following CH overtone excitation of syn-CH$_3$CHOO using vertical polarization (arrow) for the IR laser. The isotropic angular distribution indicates that unimolecular dissociation of *syn*-CH$_3$CHOO is slower than its rotational period ($\geq$ 2 ps). b, Distribution of dissociation lifetimes from trajectories started at the isomerization transition state. The most probable lifetime is set to unity.

Following IR activation of *syn*-CH$_3$CHOO, the OH products arising from unimolecular

dissociation are state-selectively detected with the UV probe laser in the experiment. A two-dimensional ion image of the OH product velocity distribution is obtained, using a VMI apparatus described previously,[85,86] as shown in Figure 5.5. The angular distribution is isotropic, indicating that dissociation occurs more slowly than the rotational period of *syn*-CH₃CHOO of ≥ 2 ps, based on experimental rotational constants.[87] The TKER distribution resulting from IR excitation at 6081 cm^{-1}, shown in Figure 5.6, is a broad and unstructured distribution with a most probable (peak) TKER of 600 cm^{-1} and breadth of 1340 cm^{-1} (FWHM). On average, the translational energy release is 1110 cm^{-1} or 20% of the available energy. Note that the VMI experiments probe OH ($\nu = 0, N = 3$) fragments accounting for 202 cm^{-1} of internal energy.

Theoretically, the translational energy distributions, obtained starting from the isomerization TS configuration using normal mode sampling and from the submerged SP configuration using micro-canonical sampling, are shown in Figure 5.6. Essentially the same results are obtained using micro-canonical sampling for trajectories starting at the VHP configuration as shown in Figure 5.7. The peak in the translational energy distribution from the isomerization TS is roughly 700 cm^{-1} higher than that from the submerged SP (ca. 870 cm^{-1}), the latter of which is in good agreement with experiment. On average, the translational energy release is about 30% of the available energy, specifically 1830 cm^{-1} from the isomerization TS and 1660 cm^{-1} from the submerged SP trajectories. In both cases, most of the available energy appears in internal excitation of the products, as elaborated below. This finding is in very good agreement with the experimental results, although the submerged SP trajectories are in better quantitative agreement. After surmounting the TS for H atom transfer, the QCT results demonstrate that unimolecular dissociation of *syn*-CH₃CHOO proceeds through the VHP intermediate to OH + vinoxy products, and likely samples configurations that are close to the submerged SP.
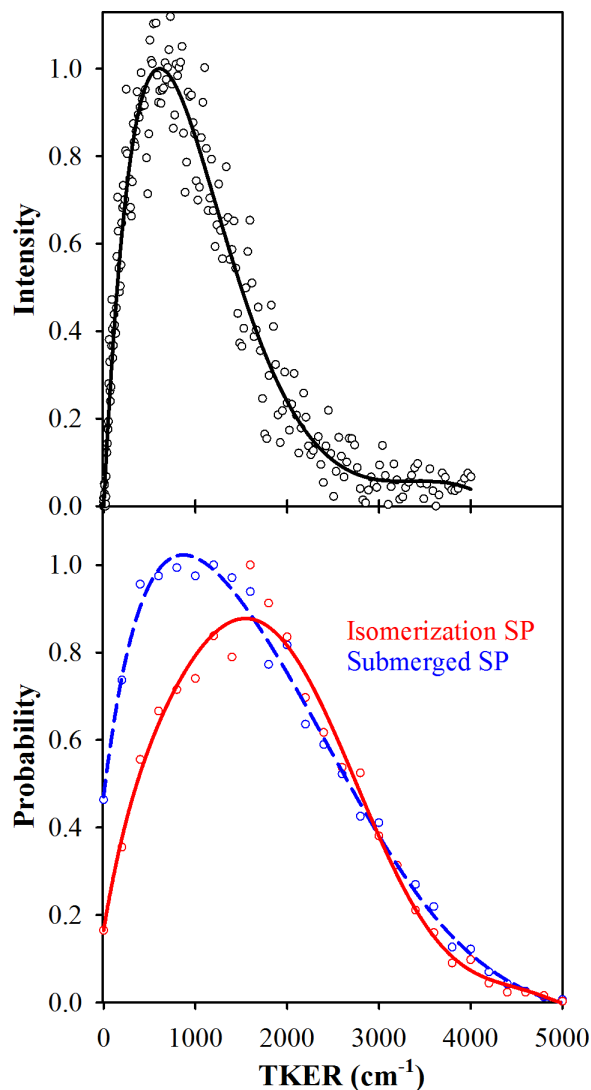
Figure 5.6:   Comparison between experimental and theoretical determinations of the total kinetic energy release (TKER). a, TKER distribution deduced from VMI of the OH products following CH overtone excitation of the *syn*-CH$_3$CHOO feature at 6081 cm^{-1}. b, Corresponding relative translational energy distribution of the products obtained from trajectories starting from the isomerization transition state (red). Trajectories starting from a submerged exit channel saddle point (blue) is shown for comparison. The peak intensity and most probable translational energies are set to unity.
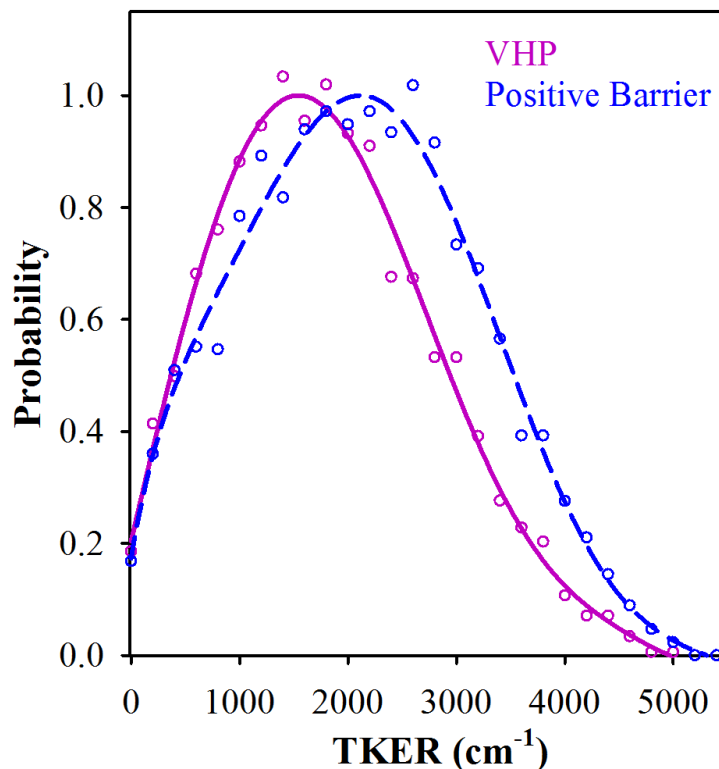
Figure 5.7: Relative translational energy distribution between the OH and vinoxy fragments resulting from QCT calculations using micro-canonical sampling starting from the VHP (purple) configuration. QCT calculations using micro-canonical sampling starting from the positive barrier (blue) configuration in the exit channel is shown for comparison. The peak probability is set to unity.

The resultant translational energy distribution from the positive exit channel barrier configuration, shown in Figure 5.7, peaks at 2600 cm^{-1} and is much hotter than the calculated and experimental results shown in Figure 5.6. This higher translational energy release is anticipated, given that the exit channel barrier lies about 1100 cm^{-1} above the product asymptote.

Furthermore, trajectories starting at the TS and propagated with a 0.1 fs time step to OH + vinoxy products are found to have a distribution of lifetimes ranging over a few

ps timescale as shown in Figure 5.5. In particular, more than 80% of the trajectories dissociate within 6 ps. As will be discussed later, the picosecond timescale is associated with IVR within the highly energized VHP species prior to O-O bond scission and dissociation to OH + vinoxy products.

The rovibrational energy distribution of the OH products was measured directly. No OH products could be detected in $\nu = 1$. A comprehensive OH $X^2\Pi_{3/2}(\nu = 0, N)$ rovibrational product state distribution was obtained previously upon IR overtone excitation of the 5984 cm^{-1} feature,[77] and is reproduced in Figure 5.8. A similar distribution was obtained for a subset of OH ($\nu = 0$) product rotational states upon excitation of the 6081 cm^{-1} feature, the focus of the present study. The OH rotational distribution peaks at $N = 3$, and this quantum state was probed in the VMI experiments. The average OH rotational energy was determined to be 560 cm^{-1} and accounts for about 10% of the available energy.

The rovibrational energy distribution of the OH fragments is also calculated from trajectories starting from the TS with normal-mode sampling as shown in Figure 5.8 (analogous results are obtained starting from VHP with micro-canonical sampling). The OH products are formed primarily in their ground vibrational state ($\nu = 0$). Less than 1% are produced with vibrational energy greater than or equal to the $\nu = 1$ fundamental. This result agrees well with experiment, where only $\nu = 0$ OH is detected. The computed OH product rotational distribution is peaked at N=3 and "cold", and in excellent accord with the experimental results. A similar OH rotational distribution is obtained for the submerged SP (Figure 5.8) and also from the positive barrier configuration.
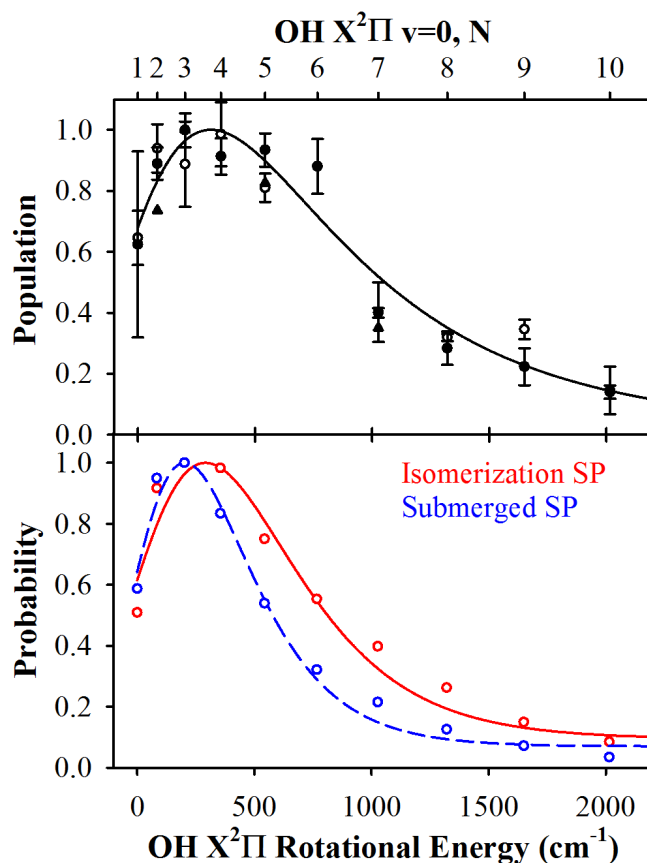
Figure 5.8: OH radical rotational state distributions. a, Rotational energy and corresponding state distribution of OH X$^2\Pi$ ($\nu = 0, N$) products following IR overtone excitation of *syn*-CH$_3$CHOO at 5987.5 cm^{-1}. [Adapted with permission from Figure S1 of Ref. 77] The Π(A') and Π(A") Λ-doublet states are indicated by filled and open circles. b, OH population distribution resulting from QCT calculations starting from the isomerization transition state (red). QCT calculations starting from a submerged exit channel saddle point (blue) is shown for comparison. The peak population and most probable OH product state are set to unity.

The rotational and vibrational distributions of the vinoxy radical products are also evaluated from trajectories starting at the TS with normal-mode sampling as shown

in Figure 5.9 (analogous results are obtained starting from VHP with micro-canonical sampling). In both cases, the vinoxy radicals are produced with significant rotational and vibrational excitation with average energies of 800 and 1700 cm^{-1}, respectively. A detailed analysis of the vibrational distribution has not been undertaken because of the high dimensionality and also coupling between vibrational modes, but will be examined in the future. Nevertheless, the QCT calculations clearly show that approximately half (ca. 45%) of the available energy is accommodated as internal excitation of the vinoxy radical products.
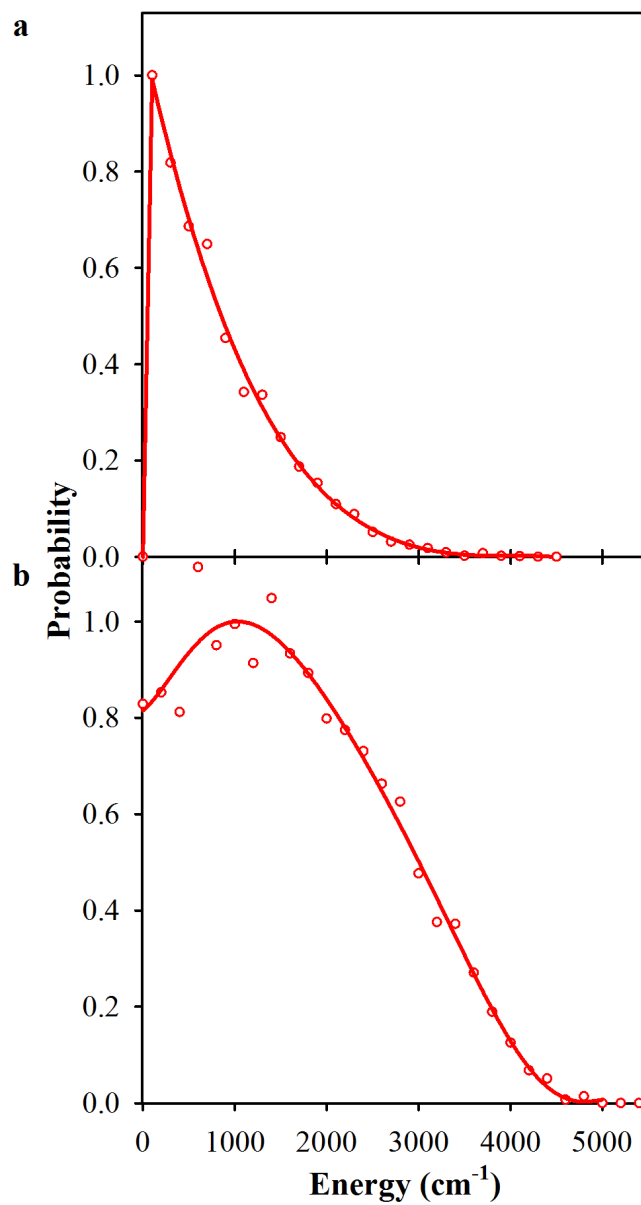
Figure 5.9:   Calculated internal energy distributions of the vinoxy (CH$_2$CHO) products. a, Rotational and b, vibrational distributions derived from QCT simulations starting from the isomerization transition state. The most probable rotational and vibrational energies are set to unity.

Significant insight on the dissociation dynamics is gained by looking at representative trajectories, even though individual trajectories show a large variation in the relative translational and rovibrational energies of the OH and vinoxy products. Snapshots of one typical trajectory are illustrated in Figure 5.10. From inspection of the sample trajectory starting at the TS, one can see that the bridging H atom is quickly transferred to the terminal O atom at 14 fs, resulting in isomerization and producing highly energized VHP. The large internal excitation of VHP is randomly distributed in different vibrational modes, and VHP also undergoes internal rotation to some extent as indicated at 1.4 ps. The time scales are different in each trajectory, but most notably the system spends significant time (ps) undergoing IVR within the VHP intermediate well region of the PES. Once the energy along the reaction coordinate is sufficient to surmount an exit channel barrier or saddle point, in this trajectory at 2 ps, VHP rapidly decomposes to OH and vinoxy products. The presence of a shallow minimum in the exit channel, shown in Figure 5.2, causes the H atom of OH to preferentially point toward the O atom of vinoxy prior to dissociation in many trajectories as seen at 2.1 ps. The picture emerging from the trajectory calculations agrees well with the experimental observation of an isotropic spatial distribution for the OH products and $a \geq 2$ ps timescale for dissociation (Figure 5.5).
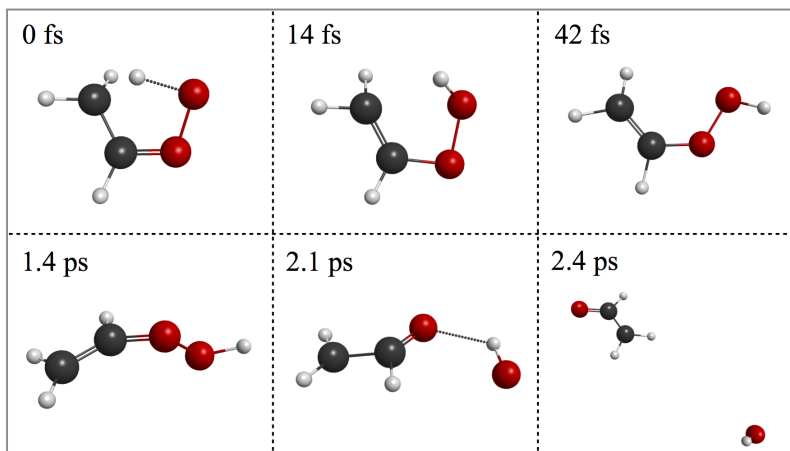
Figure 5.10:   Snapshots of a representative trajectory starting from the transition state for 1,4-H atom transfer from *syn*-CH$_3$CHOO to vinyl hydroperoxide (VHP). The highly energized VHP intermediate undergoes extensive intramolecular vibrational redistribution (IVR) on a picosecond timescale before dissociation to OH + vinoxy (CH$_2$CHO) products.

5.4   Summary

Overall, the agreement between experiment and theory is quite good, demonstrating that dissociation of *syn*-CH$_3$CHOO occurs on $a \geq 2$ ps timescale with most of the available energy resulting in internal excitation of the vinoxy products, and much less in translational excitation and minimal OH rotational excitation. The slightly different translational energy release obtained from experiment and QCT calculations suggests that the dissociation dynamics may be quite sensitive to the saddle point region in the exit channel. This

is illustrated by starting trajectories from the submerged SP and positive exit channel barrier configurations. The exit channel region of the PES is challenging to compute because of its intrinsic multi-reference electronic character, and is likely to be the origin of the small differences in the TKER distributions obtained from the experiment and theory. Nevertheless, the QCT calculations show that the unimolecular dissociation of *syn*-CH$_3$CHOO is quite complicated following H atom transfer and isomerization to VHP: intramolecular vibrational energy redistribution occurs within VHP on a few picosecond timescale and an exit channel saddle point impacts the translational energy release to OH + vinoxy products. The final step in OH production from the *syn*-CH$_3$CHOO is not a simple, barrierless O-O bond breaking process.

5.5   Prompt Decay with High Internal Energy

Ozonolysis of alkenes, such as trans-2-butene, release ca. 50 kcal/mol of excess energy to form internally excited *syn*-CH$_3$CHOO Criegee intermediates (along with carbonyl products),[61] which may undergo prompt unimolecular decay to OH products. A significant portion of the Criegee intermediates will be collisionally stabilized under atmospheric conditions, and the resultant thermalized distribution of syn-CH$_3$CHOO will more slowly isomerize to VHP and dissociate to OH products.[88] Unimolecular dissociation to OH products is a main loss process for thermalized *syn*-CH$_3$CHOO and, more generally, stabilized Criegee intermediates that decompose via the VHP channel;[89] overall, this is an important source of OH radicals in the atmosphere. The dynamical pathway(s) explored in the work discussed above upon activation of syn-CH$_3$CHOO near the isomerization TS correspond to critical energetic regions of the multi-dimensional PES that are sampled in alkene ozonolysis reactions.

Even though it is difficult to further increase the excitation energy experimentally, we can simulate the prompt decay process of *syn*-CH$_3$CHOO in theory at higher energy. Previously, the initial energy is 6000 cm^{-1} in order to directly compare with experimental measurement. In this section, we further increase the initial energy by 25 kcal/mol, which increases the initial energy to 42 kcal/mol. Note that because the energy limitation of the PES, it is not feasible to use higher energy for the dynamic simulations. Similarly, we performed the QCT calculations from the isomerization TS and VHP minimum using micro-canonical sampling at given energy. Then we performed the product analysis using the dissociation trajectories after applying the hard-ZPE constrain. Totally, 7284 and 7448 trajectories starting from VHP and isomerization TS respectively are included in the following analysis.

Dissociation trajectories starting from the TS are studied in detail. Similar to the reaction path at low energy, most trajectories quickly isomerize to VHP, then the O-O bond breaks forming the OH and vinoxy radical. Besides, we observe a different prompt pathway starting from TS, which forms OH radical in a very quick process. In the new reaction path, the bright H atom first quickly transfer to the corresponding O atom, instead of isomerizing to VHP, the OO bond directly breaks without passing the VHP minimum. Since the dissociation occurs right after H atom transfer, the OH radical is expected to form with higher vibrational energy. Besides, the dissociation occurs right after surmounting TS, it is anticipated that more available energy will release to the translation energy of the fragments for the new pathway.

The rotational and vibrational energies of OH and vinoxy radicals are calculated, and shown in Table 5.3. Note that in the previous simulations at lower energy, the rotational and vibrational energies of products are almost identical for the trajectories starting from the TS and from the VHP, which indicate all trajectories dissociate through

the VHP minimum. As seen in Table 5.3, obvious differences of the analysis results are observed between the trajectories starting from the TS and from VHP. Because of the existence of new reaction path, as expected, we observe higher relative translation energy release of the fragments, and higher percentage of OH radical is excited to the first vibrational excited state. The relative translation energy distributions calculated using trajectories starting from isomerization TS and from the VHP are shown in Figure 5.11. The obvious broadening of translation energy distributions from isomerization TS indicates the existence and effect of the prompt decay reaction path.

Table 5.3:   The analysis results of dissociation trajectories starting from the isomerization TS and from the vinylhydroperoxide (VHP), including the percentage of excited OH radical, the average relative translation energy of fragments and the internal energy of vinoxy.

	OH at $\nu = 1$	Ave. Trans. Eng.	Vinoxy Eng.
TS	8.1%	4771 cm^{-1}	6744 cm^{-1}
VHP	5.3%	4165 cm^{-1}	7820 cm^{-1}
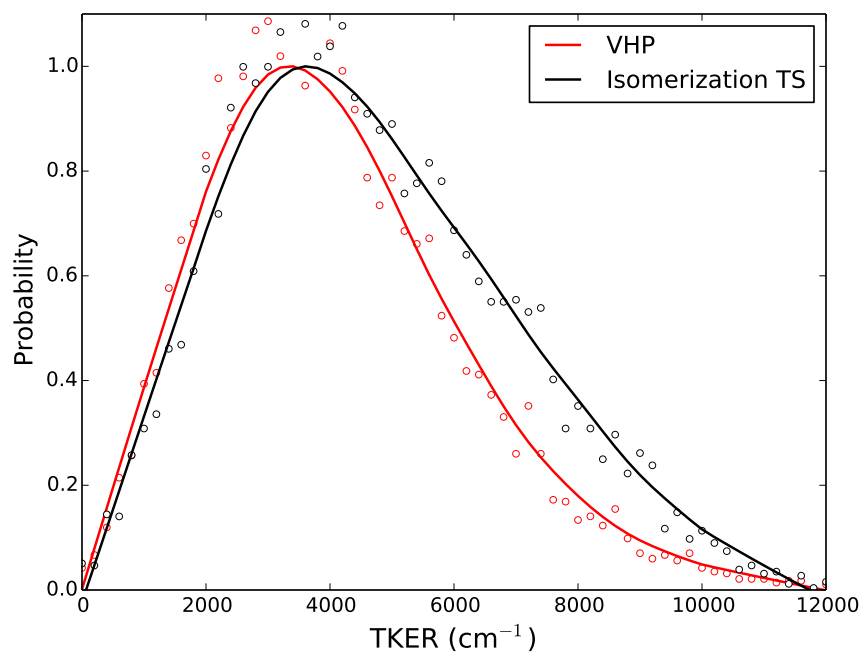
Figure 5.11: Relative translational energy distribution between the OH and vinoxy fragments resulting from QCT calculations starting from the isomerization TS (black) and from VHP (red) configurations.

Chapter 6

Mode-specific tunneling of

cis-HOCO Dissociation to H+CO$_2$

So far, the reaction dynamic simulations are all based on the classical trajectory calculations. One of the drawbacks of classical simulations is the absence of the tunneling effect, which usually results in smaller reaction rates and longer lifetimes in the calculation. Quantum dynamic simulation is required to include the tunneling effect. However, rigorous quantum calculations is highly computationally expensive, thus they are usually restricted to fairly small systems with no more than four atoms.

In this chapter, we present a one-dimensional (1D) model to describe the tunneling effect of the unimolecular dissociation of *cis*-HOCO to H+CO$_2$, using a recent projection theory that makes use of a tunneling path along the imaginary-frequency normal mode, Q_{im}, of a relevant saddle point. The tunneling probabilities and lifetimes are calculated for the ground vibrational state of *cis*-HOCO and highly excited overtones and combination bands of the modes that have large projections onto the Q_{im} path. To go beyond the harmonic approximation, which is important for the OH stretch, energies and classical

turning points are calculated using the anharmonic 1D potential. The tunneling lifetimes are calculated for a number of combination states of the OCO bend and CO stretch, which are in good accord with those estimated in a previous five-degree-of-freedom quantum wavepacket simulation of the dissociative photodetachment of HOCO$^-$. The present results are also consistent with the interpretation of the tunneling of *cis*-HOCO to H+CO$_2$ seen in recent experiments.

6.1   Introduction

The OH+CO $\rightarrow$ H+CO$_2$ reaction is one of the most important reactions in combustion and has attracted extensive experimental studies and theoretical research. The bimolecular reaction involves both *trans*- and *cis*-HOCO as reaction intermediates,[90–92] and as a result there has also been considerable interest in the vibrational dynamics of these species.[93–96] One of the most interesting issues concerning the reaction is the tunneling of *cis*-HOCO to H+CO$_2$. There are several indirect indications of tunneling, including the acceleration of the reaction by OH excitation[97] and the large H/D isotope effect[98,99]. More recently, Continetti and co-workers have provided direct evidence of this tunneling in experimental studies of the dissociative photodetachment of HOCO$^-$.[100–103] In their coincidence experiments, most dissociation to H+CO$_2$ occurs above the maximum electron kinetic energy limit predicted according to the energy of the dissociation barrier. The observations indicate that nearly all dissociation of *cis*-HOCO to the H+CO$_2$ channel is by deep tunneling through the barrier at the energy of the experiment.

Tunneling in the unimolecular dissociation of *cis*-HOCO to H+CO$_2$ has been studied theoretically by various methods. In 2006, Zhang *et. al*[104] performed full-dimensional wave packet calculations of the photodetachment of HOCO$^-$ quantum mechanically, us-

ing an early (2003) potential energy surface (PES).[92] However, since that PES is not sufficiently accurate to describe the H+CO$_2$ dissociation channel, this work did not find any evidence for the tunneling process of this reaction. More recently, Ma *et al.*[105] reported a five-degree-of-freedom wave packet quantum calculation of the tunneling resonances of relevance in the photodetachment of HOCO$^-$ with a more accurate *ab initio* permutationally invariant PES[91,106]. These calculations were highly computationally intensive, owing to the very long lifetimes of these resonances. Thus, they were not converged quantitatively; however, bounds were established for the resonances of relevance to the experiments. The lifetimes of these were in the range of microseconds or less in accord with the estimated lifetimes reported experimentally. In addition, these calculations showed that the OCO bend and the interior CO stretch of *cis*-HOCO were highly excited[105] in the photodetachment experiment. This result was qualitatively expected by simply comparing the equilibrium structures of the HOCO$^-$ and *cis*-HOCO, as noted earlier in the experiments.

Rigorous quantum approaches, i.e., numerical solutions of the full-dimensional Schrödinger equation, becomes less feasible as the lifetimes increase and so deep tunneling is a still a major challenge for these approaches. Several 1D reaction-path models do exist that can describe the deep tunneling behavior. Johnson *et al.*[107] considered one based on the OH distance and calculated the relaxed potential from *cis*-HOCO to the formation of H+CO$_2$ as a function of this distance. This potential was used to interpret the experimental results and tunneling lifetimes were reported using this potential. Using the model, the internal energy of CO$_2$ product was predicted in fairly good agreement with the experimental data. As noted, in this model the OH distance was taken as the reaction coordinate. The assumption was based on the fact that the imaginary-frequency normal mode of the saddle-point barrier was dominated by the OH stretch. However, as these authors

noted the model did not consider the effects of other modes and so over-emphasized the contribution of OH stretch. The calculated lifetimes of tunneling states associated with overtones of the OH stretch were thus almost certainly too short. More comment will be given below.

Here we apply a recent normal-mode "reaction-path" approach to mode-specific tunneling based on the what we have termed the Q_{im}-path.[108] This approach has been applied and tested for vibrational ground-state tunneling with surprisingly good accuracy, considering the simplicity of the method.[108–111] In this approach, the imaginary-frequency normal mode of a relevant saddle point (SP), Q_{im}, is chosen as the path variable, and the relaxed potential, $V(Q_{im})$, i.e., the potential fully relaxed with respect to other SP normal modes, is taken as the potential along this path. The Q_{im} approach was shown to accurately describe tunneling in the D+H$_2$ reaction[109] and the tunneling splitting in malonaldehyde and vinyl[110,111]. Recently, Wang and Bowman[108] extended the approach to describe mode-specific tunneling in malonaldehyde and achieved semi-quantitative agreement with experiment. The central component of this extension is the projection of the normal modes of a minimum onto the Q_{im} path. The effect of mode excitation is mapped onto the change of the turning points on $V(Q_{im})$, relative to those for the ground vibrational state, and the resulting change in tunneling probability is then easily calculated, semi-classically. Here we apply this approach for the first time to a unimolecular dissociation to investigate the tunneling process of *cis*-HOCO $\rightarrow$ H+CO$_2$. Three modes of *cis*-HOCO, the OCO bend, interior CO stretch and OH stretch, are found to have large projections on the Q_{im} path, and so the tunneling probabilities and lifetimes are calculated for the fundamentals, overtones and combination states of these three modes. As noted above, the OCO bend and interior CO stretch modes are excited in the photodetachment experiment and so the present work is highly relevant to this experiment.

For the modes with zero or very small projection, vibrationally adiabatic (VA) theory could be applied, as was done in Ref. 108, to predict whether the mode excitation will enhance the tunneling process or not. We do use this theory, qualitatively, below.

Several full-dimensional PESs have been reported for HOCO recently. Wang and Bowman[94] reported a semi-global PES, which can accurately describe the isomerization between the *cis*- and *trans*- isomers and the vibrational states of both. But this PES does not include the *cis*-HOCO dissociation channel. In another study, Li *et. al*[91] developed a global permutation invariant PES which included all the reaction channels and stationary points. However, the frequencies of *cis*-HOCO were not very accurate, e.g., the frequency of OH stretch is about 250 cm^{-1} in error compared to the direct *ab initio* result. Since the Q_{im} turning points are determined based on the frequencies of *cis*-HOCO, the differences of frequencies can affect the calculated tunneling results. Most recently, Chen *et. al*[112] published an accurate full-dimensional PES of HOCO by fitting roughly 80,000 electronic energies obtained with the high-level UCCSD(T)-F12a/aug-cc-pVTZ method. This PES describes the properties of *cis*-HOCO and the dissociation channel quite accurately. Therefore, we use this PES to obtain the Q_{im} path, $V(Q_{im})$ potential, and normal mode vectors of *cis*-HOCO and the SP. A plot of $V(Q_{im})$ is given in Figure 6.1 along with a comparison of directly *ab initio* UCCSD(T)-F12a/aug-cc-pVTZ energies. As seen, the PES is in excellent agreement with these high-level energies. Note that the Q_{im} value at the global minimum is -56.0 bohr. We explain the meaning of the labeled horizontal lines shown in this figure below.
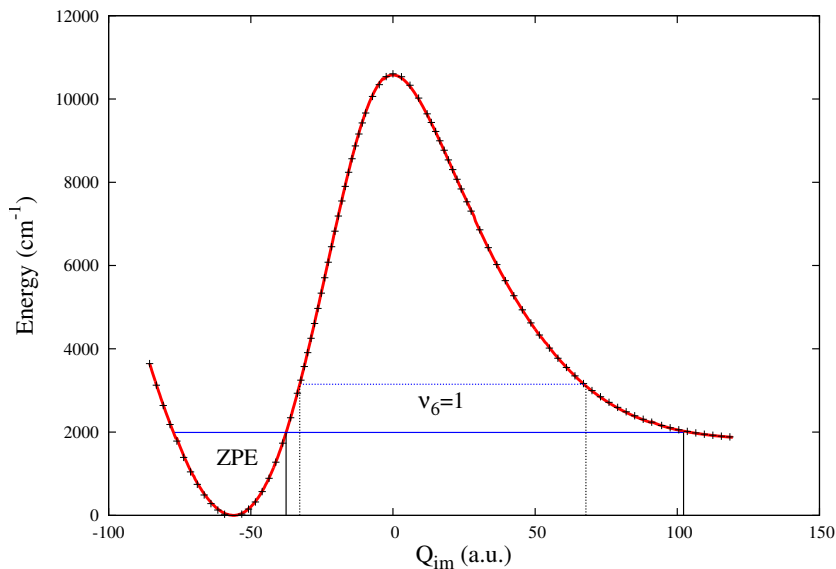
Figure 6.1:   Potential along the Q_{im} path along with directly calculated UCCSD(T)-F12a/aug-cc-pVTZ energies (+). The horizontal lines indicate the turning points related to the zero-point state and the fundamental excitation of mode ν_6, the OH stretch of *cis*-HOCO. See text for more details.

6.2   Method

Given a 1D potential of the form shown in Figure 6.1, the deep tunneling rate is given semiclassically by the well-known expression

$$k = \frac{\omega}{2\pi}e^{-2\theta}, \ \theta = \frac{1}{\hbar}\int_{a_1}^{a_2} dQ_{im}\sqrt{2(V(Q_{im}) - E)}, \tag{6.1}$$

where ω is the vibration frequency of $V(Q_{im})$, typically the harmonic frequency at the minimum (what we use here), a_1, a_2 are the classical turning points, and $e^{-2\theta}$ is the tunneling probability. To complete the model, one needs a criterion to determine these turning points, specifically for the ground vibrational state of *cis*-HOCO. A reasonable

criterion is based on the energetics of the dissociation dynamics, which in this case is that the harmonic zero-point energy (ZPE) of *cis*-HOCO exceeds the energy of the products H+CO$_2$ (with harmonic ZPE) by roughly 130 cm^{-1}. Thus, the ground-state turning points were determined using the harmonic ZPE of *cis*-HOCO, as indicated in Figure 6.1. (We note that effects of anharmonicity on the *cis*-HOCO and CO$_2$ ZPEs could in principle be accounted for; however, as the theory we use is not fully anharmonic we do not consider those effects here.) Finally, as indicated, the effect of exciting mode 6, the OH-stretch of *cis*-HOCO, is predicted from the projection model to change the turning points so as to clearly decrease the tunneling integral and thereby increase the tunneling rate. The theory that gives this result has been given previously[108] and so we just summarize it next.

The goal of the projection model is to determine how excitation of normal mode Q_i of the *cis*-HOCO changes the ground vibrational-state turning points. This is done straightforwardly by relating the normal modes of the minimum to those of the saddle point and more relevantly to the imaginary-frequency normal mode Q_{im} since that is the path variable in the theory. The relationship is given by:[108]

$$Q_{im} \;\; = \;\; -56.0 + \sum_{i=1}^{3N-6} \mathbf{q}_{im}^T \mathbf{q}_i Q_i(n_i), \qquad (6.2)$$

where the constant -56.0 (in mass-scaled atomic units) is specific to *cis*-HOCO, i.e., it is just the value of Q_{im} at the minimum of *cis*-HOCO (see Figure 6.1)

As seen, the magnitude of the projection $\mathbf{q}_{im}^T \mathbf{q}_i$ is a key element in relating Q_{im} to Q_i, where $\mathbf{q}_{im}$ is the mass-scaled unit vector of the imaginary-frequency normal mode of the saddle point and $\mathbf{q}_i$ are the corresponding vectors of the minimum. It should be noted that independently this projection element was reported previously by two groups

in very different contexts to give a qualitative correlation between mode excitation and increased reactivity (not tunneling) in atom-diatom[113] and atom-triatom reactions[114] and increased tunneling splittings in a symmetric double well.[115]

Using this equation, it is trivial to obtain an expression for the change in turning point corresponding to the excitations of mode i relative to the ground state. This is given by:[108]

$$\Delta Q_{im}^{tp}(n_i) = |\mathbf{q}_{im}^T \mathbf{q}_i|(|Q_i^{tp}(n_i)| - |Q_i^{tp}(n_i = 0)|), \tag{6.3}$$

where, in the harmonic approximation, the turning points are given by $Q_i^{tp} = \pm\sqrt{(2n_i + 1)/\omega_i}$. Here we choose the positive sign to be consistent with the left potential well. (The change in the Q_{im}-turning point with excitation of the fundamental of OH-stretch mode is shown in Figure 6.1) Thus, excitation of modes with substantial projections cause a positive change of Q_{im}, which results in a decrease of θ, and thus a faster tunneling rate and shorter lifetime. In contrast, the excitation of modes with zero or very small projection on $\mathbf{q}_{im}$ are predicted to have no enhancement of the tunneling. As noted above, and numerically demonstrated for malonaldehyde, such modes may be accurately described by separable vibrational adiabatic (VA) theory.[108] Finally, we note that for combination bands the change in the turning point ΔQ_{im}^{tp} is simply the sum of the changes for the relevant modes and their excitations.

Clearly, this is a simple theory to implement in full-dimensionality and one cannot expect "exact" results from this theory. However, *with an accurate potential*, which we do use, we can anticipate semi-quantitative accuracy, especially when considering the many orders-of-magnitude range of the effects of mode excitations on the tunneling rate.

The normal-mode vectors and frequencies of the *cis*-HOCO and SP are given in Table 6.1. From our calculation, mode 1 (torsion), mode 4 (HOC bend), and mode 5 (terminal

CO stretch) of *cis*-HOCO have almost zero projections onto Q_{im}. In contrast, modes 2 (OCO bend), 3 (interior CO stretch) and 6 (OH stretch) have large projections; the values are 0.264, -0.462 and 0.844 respectively. Thus, we focus on these three modes and only briefly comment on the other modes, using qualitative VA theory. Note that the projection of the OH stretch is the largest of all modes and thus the OH distance is reasonable zeroth-order choice for the reaction path, as was done in Ref. 108. However, that is not done here.

Table 6.1: Normal mode vectors and frequencies (cm^{-1}) of the *cis*-HOCO minimum and the saddle point (SP) of dissociation.

cis-HOCO			SP		
mode	freq	vector	mode	freq	vector
ν_1	578.3		ν_1	1956.6i	
ν_2	601.7		ν_2	534.9	
ν_3	1083.3		ν_3	654.3	
ν_4	1308.0		ν_4	940.7	
ν_5	1858.1		ν_5	1300.5	
ν_6	3644.1		ν_6	2174.2	
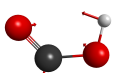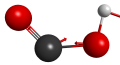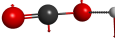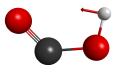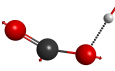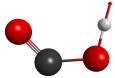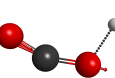
6.3   Results and Discussion

As mentioned above, we focus on modes 2, 3 and 6, the OCO bend, the interior CO stretch and the OH stretch, respectively, as these modes have large projections onto the Q_{im} path. We consider fundamental, overtone and combination excitations and calculate the tunneling probabilities and lifetimes. For combination states the change in turning points is obtained as the sum of the changes for each mode excitation. For modes 2 and 3 the harmonic model described above is adequate, as these modes are described reasonably well by this approximation. However, as expected, mode 6, the OH stretch, is highly anharmonic and so a simple anharmonic treatment of that mode was made. Specifically, to calculate the excited overtone (up to $\nu = 4$), we solve the 1D Schrödinger equation with a grid-based discrete variable representation (DVR) using the 1D potential along the OH stretch normal mode. The 1D potential, vibrational energies and turning points are shown in Figure 6.2. The tunneling probabilities and lifetimes of the OH stretch are calculated using the anharmonic outer turning points.
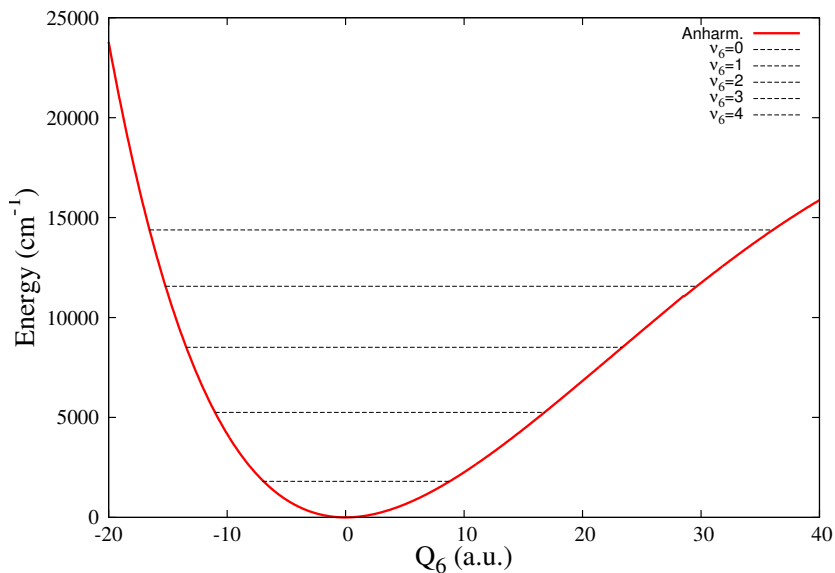
Figure 6.2: One dimensional potential along the OH stretch of *cis*-HOCO. The horizontal lines indicate the anharmonic vibrational energies and turning points of the OH ground and excited states.

The results for the fundamental and overtone excitations are given in Table 6.2 and shown graphically in Figure 6.3 as a function of the energy. In Table 6.2 and Figure 6.3, we do see a large enhancement of tunneling with excitation of these three modes. (Note the tunneling lifetime is just 1/k.) As seen in Figure 6.3, the energy distributed in different modes has different effects on the tunneling process, and the OCO bend mode shows the largest enhancement to the tunneling as a function of the vibrational energy. This is a direct consequence of equation 6.3.

Table 6.2:   The change of turning point (a.u.), tunneling probability and lifetime (s) for mode excitations of *cis*-HOCO, relative to the ground state. Note the vibrations of mode 2 and 3 are treated using the harmonic approximation, while the OH stretch vibration is described anharmonicly.

ν	Mode 2: OCO-bend			Mode 3: Interior CO-stretch			Mode 6: OH-stretch		
	ΔQ_{im}^{tp}	Prob.	Lifetime	ΔQ_{im}^{tp}	Prob.	Lifetime	ΔQ_{im}^{tp}	Prob.	Lifetime
1	3.68	8.04E-17	1.71E+03	4.81	8.22E-16	1.67E+02	6.68	3.13E-14	4.39E+00
2	6.22	1.30E-14	1.05E+01	8.13	4.58E-13	3.00E-01	12.32	6.05E-10	2.27E-04
3	8.28	6.06E-13	2.26E-01	10.82	5.19E-11	2.64E-03	17.61	1.46E-06	9.41E-08
4	10.07	1.44E-11	9.52E-03	13.15	2.27E-09	6.06E-05	23.03	8.64E-04	1.62E-10
5	11.66	2.08E-10	6.59E-04	15.23	5.28E-08	2.60E-06			
6	13.11	2.14E-09	6.41E-05	17.13	7.66E-07	1.79E-07			
7	14.46	1.68E-08	8.15E-06	18.89	7.63E-06	1.80E-08			
8	15.72	1.07E-07	1.29E-06	20.53	5.67E-05	2.42E-09			
9	16.90	5.62E-07	2.44E-07	22.08	3.19E-04	4.30E-10			
10	18.03	2.52E-06	5.46E-08	23.55	1.42E-03	9.67E-11			
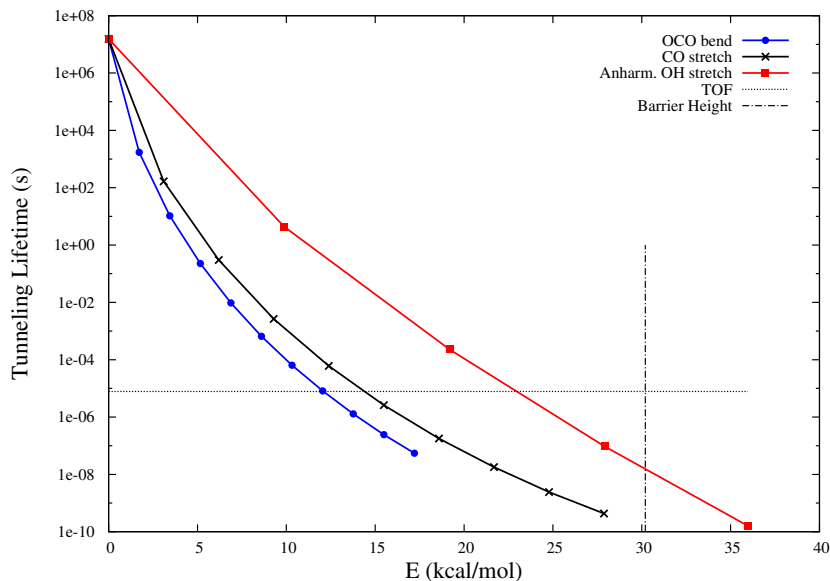
Figure 6.3:   Tunneling lifetimes (s) as a function of energy (kcal/mol) in excitations of the OCO bend, the interior CO stretch and the OH stretch. Each "data" point represents an excitation level in the indicated mode. The horizontal line indicates the time of flight (TOF) of the photodetachment experiment, and the vertical line indicates the dissociation barrier height. Anharmonicity is considered for the OH stretch as described in the text.

Next we consider the connections to the Continetti and co-workers photodetachment experiment.[102,103,107] As noted by that group, the modes of *cis*-HOCO excited by the photodetachment of *cis*-HOCO anion are mode 2, the OCO bend, and mode 3, the interior CO stretch, and negligible excitation of mode 6. In the experiment, *cis*-HOCO dissociation can be observed if the tunneling lifetime is shorter than the time of flight (TOF), about 7.8 μs. As shown in Figure 6.3, which considers just the pure overtones, if just mode 2 and mode 3 are excited, with energies of roughly 12 and 15 kcal/mol, respectively, (much smaller than the reaction barrier of about 30.2 kcal/mol) the tunneling lifetime is smaller than the TOF and so the prediction is that dissociation from these states would be observed in these experiments. Further quantitative predictions for

combination states are made below.

Additional calculations were done for the states likely excited experimentally; for this we are guided by the Ma *et al.* quantum simulation of *cis*-HOCO$^-$ photodetachment.[105] They presented a calculated stick Franck-Condon spectrum for the photodetachment to *cis*-HOCO and also estimated lifetimes of the resonances in their spectrum. Qualitatively, the lifetimes of the prominent peaks assigned to combination bands of modes 2 and 3, are in accord with a microsecond lifetime estimated from the experiment based on the flight time. Based on the assignments of the prominent peaks in this spectrum,[105] the tunneling probabilities and lifetimes of those combination states are calculated using our model and are given in Table 6.3. Here the notation of states is changed to be consistent with the simulation and experiment as well, where mode 4 is the interior CO stretch and mode 5 is the OCO bend. Generally speaking, we get good agreement with the quantum estimates, especially for the shorter lifetimes. Also, it should be re-stated that the the 5D wave packet calculations used a slightly different PES from the one we use. Considering the simplicity of the 1D model, the level of agreement with quantum calculations is quite encouraging and gives us some confidence in the new predictions made here.

Table 6.3:   The tunneling probabilities and lifetimes (s) of *cis*-HOCO combination states, and comparison with previous quantum wavepacket calculation using a similar PES. Note experimental notation is used for the interior CO stretch (denoted mode 4 here) and the OCO bend (denoted mode 5 here).

States	Prob.	Lifetime	Wavepacket[a]
5^4	1.44E-11	9.52E-03	$\tau < \mu$s
5^5	2.08E-10	6.59E-04	$\sim\mu$s
5^6	2.14E-09	6.41E-05	μs $> \tau >$ns
$4^1 5^3$	2.08E-09	6.59E-04	$\sim\mu$s
$4^1 5^4$	3.14E-08	4.37E-06	μs $> \tau >$ns
$4^1 5^5$	3.10E-07	4.43E-07	μs $> \tau >$ns
$4^1 5^6$	2.21E-06	6.22E-08	μs $> \tau >$ns
$4^2 5^2$	1.43E-08	9.63E-06	μs $> \tau >$ns
$4^2 5^3$	2.84E-07	4.83E-07	μs $> \tau >$ns
$4^2 5^4$	3.09E-06	4.44E-07	μs $> \tau >$ns
$4^2 5^5$	2.33E-05	5.90E-09	$\sim$ns

[a] Ref. 105

For the three modes with zero projection, the VA theory could be valid to predict the excitation effect. In VA theory, instead of the 1D potential shown in Figure 6.1, the effective potential is used. This potential is given by $V(Q_{im})$ plus the local vibrational energy of a given mode. If the effective potential barrier is increased, qualitatively, the tunneling probability will decrease. In the harmonic approximation, the change of the effective potential barrier is determined by the difference between the harmonic frequency

of the minimum normal mode and the correlated normal mode of SP. According to our calculation, the three zero projection modes of *cis*-HOCO, mode 1, 4 and 5, have large overlap with one of the SP modes, mode 3, 4 and 6 respectively. Differences of the harmonic frequencies of these modes are +76, -367 and 316 cm^{-1}. Mode 5, the terminal CO stretch, shows a large positive value, and VA theory predicts that its excitation will inhibit the tunneling process. In contrast, the excitation of mode 4, HOC bend, is predicted to mildly enhance the tunneling. It was found that for the OH+CO $\rightarrow$ H+CO$_2$ reaction, the CO vibrational excitation reduced the reaction rate.[116] If we assume that the CO excitation will mostly project onto the terminal CO stretch of *cis*-HOCO, then our VA prediction of terminal CO stretch inhibiting the tunneling process is consistent with the observation in the experiment.

As far as we know, no experimental results are available for the tunneling effect of *cis*-HOCO with OH stretch excitation. Previously, Johnson and Continetti[107] presented a 1D effective potential (and barrier) from direct *ab initio* calculations and also one modified based on their experiment. The estimated lifetimes for the OH fundamental and first overtone are on the order of 10^{-8} and 10^{-12} s, respectively for the former potential. For the latter, modified potential the corresponding lifetimes are longer than 10^{-5} s and about 10^{-10} s for the overtone. As seen, our calculated tunneling lifetimes are longer than these results. The difference in the case of using the *ab initio* 1D potential can be traced to the assumption of the OH stretch as the reaction coordinate. In the projection model this would imply a unit projection of that normal mode eigenvector onto $\mathbf{q}_{im}$. The projection is large, i.e., 0.84, but assuming a projection of unity would lead to a significant overestimate of the effect of excitation of that mode on the tunneling rate.

6.4   Summary and Concluding Remarks

In summary, we applied a new projection theory to calculate mode-specific tunneling lifetimes of the dissociation of *cis*-HOCO to H+CO$_2$. For modes with large projections on the Q_{im} reaction path, we calculated the tunneling probabilities and lifetimes from fundamental excitations to highly excited overtones as well as combination excitations of the OCO bend and interior CO stretch. The combination states were previously shown in five-dimensional quantum simulations to be the dominant ones in the photodetachment experiment leading to vibrationally excited *cis*-HOCO and subsequent tunneling to form H+CO$_2$. The present calculations of lifetimes agree well with the estimates from these quantum calculations using a recent PES, which is somewhat less accurate for this dissociation channel than the one used here. Predictions of the lifetimes of overtone excitation of the (anharmonic) OH stretch indicate that the second overtone (and possibly the first overtone) may have a lifetime sufficiently short to show the effect of tunneling in spectroscopic measurements where the OH stretch can be pre-excited. For the modes with zero projections and which have dominant overlap with one saddle point normal mode, vibrationally adiabatic theory was applied qualitatively. For the CO stretch, in the OH+CO reaction this theory qualitatively explains the inhibition of the reaction upon excitation of this stretch.

It is worth emphasizing that the projection theory assumes a separable model for the vibrational eigenstates of *cis*-HOCO and so mode-mixing is clearly absent in the current model. Strong mixing can clearly affect the assignments and lifetimes of actual molecular eigenstates/resonances. However, if an eigenstate analysis uses uncoupled normal-mode functions as a zero-order basis the present analysis could still be quite useful since each basis function has a lifetime associated with it and could be used in a more general theory.

Such an analysis is feasible, albeit computationally much more intensive than the current model.

Finally, with the availability of full-dimensional *ab initio* potential energy surfaces, such as the one used here, the calculation of lifetimes of *cis*-HOCO vibrational states by other methods will hopefully be done. As mentioned in the Introduction, exact approaches are very computationally demanding. However, having benchmark results would be extremely worthwhile to test approximate methods. These include reduced dimensionality quantum approaches, e.g, the 5 degree-of-freedom one already applied to *cis*-HOCO (albeit with a different PES[105]), and a 3 degree-of-freedom one applied earlier to HOCO resonances[117]. Several transition-state-based approaches could also be used to obtain mode-specific lifetimes. These include reaction-path vibrationally adiabatic theory,[118,119] and semi-classical transition-state-theory.[120] The latter theory has been applied recently with good success to a calculation of the rate constant of the OH+CO reaction to H+CO$_2$.[121] That semi-classical theory is ideally suited for tunneling near the top of the barrier but "is qualitatively incorrect for deep tunneling" as recently pointed out.[122] Suggestions for extending the theory to that region, which is of relevance to the present study, were made[122] and it would be interesting to apply those to *cis*-HOCO dissociation. It should be noted that in these transition state theories the modes are those of the transition state and not of the quasi bound molecule, in contrast to the present projection model. Thus, a mapping of the transition state modes to the molecular modes (more precisely the molecular vibrational eigenstates) is needed to make direct comparison with the experiment. Reaction-path vibrationally adiabatic theory is one reasonable way to do this in principle. However, there can be non-adiabatic effects associated with that theory for excited states. These have been described in detail in several applications of that theory to bimolecular reactions, specifically examining reactant mode-specific effects.[123,124] Nev-

ertheless an application of the transition-state based theories to *cis*-HOCO mode-specific dissociation would be very interesting and a comparison with the present calculations would be very valuable.

Part III

Application: Vibrational Calculation

Chapter 7

Anharmonic rovibrational calculations of singlet cyclic C_4

7.1 Introduction

Small carbon clusters C_n are important intermediates in the interstellar space, and tetracarbon is one of the most important species. Larger clusters, notably C_{60}, have unusual and technologically important electrical and physical properties. They are challenging theoretically, owing to substantial multi-reference character and low-lying electronic states. There are large amounts of literature on the electronic spectroscopy of small carbon clusters but less on the vibrational spectroscopy. This is important for possible detection of the clusters in the interstellar medium. Previous work dealing with small carbon clusters is summarized in the reviews of Weltner and Vanzee[125] and Orden and Saykally.[126] For the C_{2n} clusters, such as C_4, C_6 and C_8, *ab initio* calculations predict two low-energy structures, linear $\left(^3\sum_g^-\right)$ and monocyclic $\left(^1A_g\right)$. For C_4, it has been known that the linear and cyclic isomers are almost isoenergetic, with the highest level calcula-

tions of previous studies finding the cyclic isomer to be the lower energy structure.[127,128]

Experimentally, coulomb explosion imaging[129,130] and electron photodetachment[131] provided evidence of the existence of cyclic C_4 isomer. In the latter experiments, three distinct photo detachment wavelengths indicated three different structures for the C_4 anions and the neutrals. However, these experiments did not report any determination of vibrational excitations, and as far as we know, no experimental spectroscopic data of the cyclic C_4 are available in the literature.

Theoretical methods have been utilized to study the C_4 vibrations. Based on an MP2/6-311G* study, Martin et $al.$[132,133] suggested that a 1284 cm^{-1} matrix IR feature[134] belongs to cyclic C_4. In a later study, Martin et $al.$[135] constructed a CCSD(T)/cc-pVTZ quartic force field (QFF) for cyclic C_4, and re-evaluated the assignment of the 1284 cm^{-1} feature. The estimate for the ν_6 mode of cyclic C_4, 1320$\pm$10 cm^{-1}, raised doubts about the earlier assignment. More recently, Senent et $al.$[136] reported MRCI+Q/cc-pVTZ QFFs for both the linear and cyclic C_4. Their computed vibrational perturbation theory (VPT2)[137] fundamentals of cyclic C_4 showed differences as large as 50 cm^{-1} when compared to Martin's results. In addition, Martin et $al.$ reported a strong Fermi resonance between ν_6 and $\nu_3 + \nu_5$ for cyclic C_4, which contributes to a significant anharmonicity for the ν_6 mode.

We report a new ab $initio$ QFF constructed at the CCSD(T)/cc-pCV5Z level, and a semi-global potential energy surface (PES) fitted from CCSD(T)-F12b/aug-cc-pVTZ (aVTZ) energies for the singlet cyclic C_4. The vibrational configuration-interaction (VCI) calculations are performed using the MULTIMODE (MM)[29,30,36] program, and VPT2 analyses are performed with the SPECTRO[140] program. Consistent, reliable and highly accurate vibrational (and ro-vibrational) energy levels and spectroscopic constants are generated for the singlet cyclic $^{12}C_4$ and ^{13}C isotopologues. Such QFF+VPT2/VCI and

PES+VCI calculations have been widely used to determine the ro-vibrational spectroscopic constants and vibrational fundamentals of many astronomically interesting molecules in recent years.[38,135,142,143]

7.2 Computational Methods

All the *ab initio* calculations for the electronic ground state energies are performed using the coupled-cluster single and double excitations with a perturbation treatment of triple excitations, CCSD(T), with MOLPRO.[58] The linear C_4 system shows a strong multiconfigurational character, however, the non-dynamical correlation effects are not significant for the configurations around cyclic C_4, with the $\mathscr{T}_1$ diagnostic[144] smaller than 0.02.

7.2.1 Quartic Force Field

Initially, the QFF construction is calculated using energies which are extrapolated to the complete basis set (CBS) limit. However an unstable vibrational fundamental of the out-of-plane mode, ν_4 is found on those QFFs fitted from CBS-limit energy extrapolations. This mainly results from the carbon-carbon multiple bond sensitivity with respect to the basis set superposition error.[145] In order to avoid any extrapolations that would magnify the errors, only the CCSD(T)/cc-pCV5Z calculation is applied and reported. Six symmetry-adapted internal coordinates have been defined with step size 0.005Å/rad. The CCSD(T) single point calculations are carried out on 114 symmetry-unique geometries with cc-pCV5Z basis. The cc-pCV5Z energies are further refined by adding the CCSD(T) core-correlation effects using the Martin-Taylor basis[146] or cc-pCVXZ (X=T,Q) basis.

Next, for each set of *ab initio* calculations, 225 symmetry-redundant geometries are fitted to 52 non-zero force constants (up to quartic level) in the six symmetry-adapted

internal coordinates. The average root mean square (RMS) fitting errors range from 0.82E-6 cm^{-1} to 1.67E-5 cm^{-1}. Spectroscopic constants, vibrational energy levels, and vibrationally averaged geometries are computed using VPT2 with the SPECTRO program. Coriolis coupling between ν_2 and ν_3 is included in vibration-rotation interaction analysis. A Fermi resonance polyad $\nu_1{=}2\nu_5$ and $\nu_2{=}2\nu_5$ is included in the perturbation treatment. Significance of the Fermi resonance $\nu_6{=}\nu_3{+}\nu_5$ is also checked. See more details in the Results Section.

The fitted force constants can be directly used for SPECTRO calculations, but are not appropriate for VCI calculations. In order to ensure correct limiting behavior of the potential, Morse-cosine coordinates are required for a VCI calculation using the QFF potential. The fitted force constants are converted to Cartesian derivatives at the exact QFF minimum by the INTDER 2005 program.[147] Then it is transformed back to a new set of force constants defined with 5 C-C bond stretches and 1 torsion coordinate. In this way, the diagonal quadratic and cubic force constants for the 4 single C-C bond stretches are determined which are necessary to derive the appropriate alpha value for the Morse function.[148] With this alpha value, a new coordinate space includes the symmetry-adapted Morse functions (for stretches), cosine (for bending angles) and sine (for torsion angles) coordinates, while the symmetry-adaption formula and the order and the symmetry type of 6 coordinates are the same as defined before.[135] The same set of 225 energies are re-fitted with these symmetry-adapted Morse/cosine/sine basis to get a new set of 52 non-zero coefficients which now can be used in the VCI calculations.

7.2.2 Semi-global PES and MULTIMODE Calculations

As already noted, we also developed a limited potential energy surface for the singlet cyclic C_4, on which we compute ro-vibrational energies variationally. The electronic structure energies are computed using the CCSD(T)-F12b[54,55] method, with aVTZ basis. For the generation of PES points, the majority of the configurations are obtained by running classical direct-dynamics calculations, using density functional theory (DFT) with the aug-cc-pVDZ basis. Additional points are generated by randomly sampling around the cyclic C_4 minimum. Finally, 2,914 CCSD(T)-F12b/aVTZ electronic energies are used for the PES fitting. The PES of C_4 is six dimensional, and is invariant with respect to all permutations of the four C atoms. We use the invariant polynomial fitting method,[3,149] in which the polynomials are functions of Morse variables with alpha value fixed at 2.0 bohr. The coefficients in the potential expression are obtained using standard weighted least-squares fitting subroutines. The total power of fitting polynomial is restricted to 7, the number of coefficients is 123, and the overall root mean square (rms) fitting error is about 30 cm^{-1}. Figure 7.1 shows the number of configurations in different energy ranges and the corresponding rms fitting error. Most of the configurations are sampled around the cyclic C_4 minimum, plus 52 additional points at energies 30 - 75 kcal/mol relative to the minimum. These high energy points are necessary to ensure the PES behave properly at high energy region. Since the number of high energy points is small, overall PES accuracy around minimum is not affected. Even though the $\mathscr{T}_1$ diagnostic is relatively large for the 52 high energy points, i.e. 0.022 - 0.028, their impacts on the lower energy part of PES are not significant. As we focus on the vibrational states below 3000 cm^{-1}, the contaminations from other (higher) electronic states are estimated less than 1 cm^{-1}. The fitting RMS below 5000 cm^{-1} and 10,000 cm^{-1} are about 14 cm^{-1} and 25 cm^{-1},

respectively.
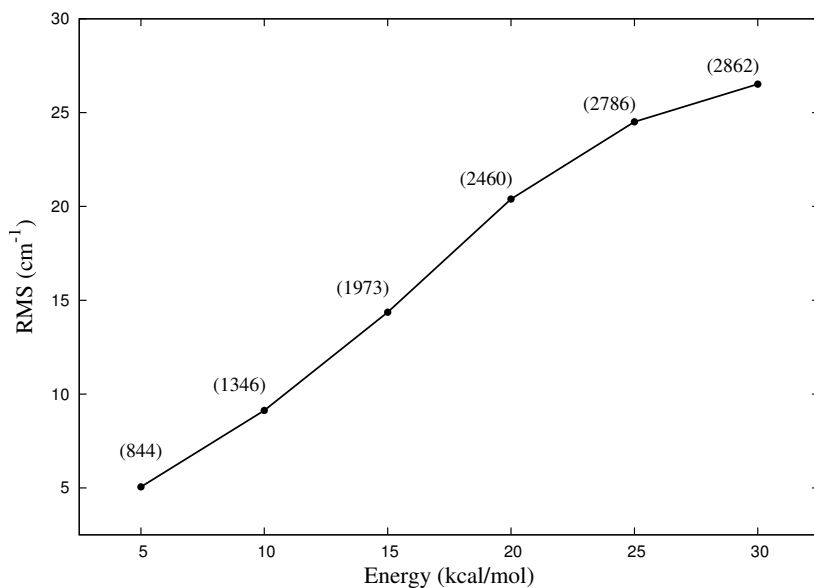
Figure 7.1: Root-mean-square (RMS) of the PES fitting error vs. relative energy with respect to cyclic C$_4$ minimum. The numbers in parenthesis are the number of configurations in the energy range.

Ro-vibrational calculations are performed using the MULTIMODE (MM) program.[30,36] For C$_4$, the exact potential is six dimensional, however, our tests of 4MR and 5MR calculations demonstrate that the 4MR convergence for most energy levels discussed here is better than 1 cm^{-1}. See more details in the Results Section, where 4MR and 5MR results are presented.

In MM calculation, each (CI) basis function is restricted by the maximum excitation quanta on each mode, and the maximum sum of excitation quanta on all modes. In our calculation, 26 primitive harmonic-oscillator basis are included with 18 Gauss Hermite integration points for each mode. The maximum quanta for single mode are tested from

8 to 12, and we obtained the convergence within in 0.1 cm^{-1}. For $J > 0$, the procedure is more complicated since there are $2J + 1$ rotational functions. Detailed description can be found in previous studies.[30,36]

7.3   Results

The equilibrium structure, rotational constants, and the harmonic frequencies of the cyclic C_4 are listed in Table 7.1. The definition of structural parameters is consistent with that in Ref 135. As shown in Table 7.1, our CCSD(T)-F12b/aVTZ structure is very similar to the CCSD(T)/pVQZ structure in Ref. 135. However, the R_{12} and R_{13} from the previous MRCI+Q study[136] are longer than the CCSD(T)/CV5Z values by 0.007 Åand 0.015 Å, respectively. It is not unusual to see MRCI overestimate the bond lengths and its deviations are mainly caused by the *ab initio* method limitations (compare to the error compensation in CCSD(T) method), basis set incompleteness and the core correlation effects. Such structure deviations consequently lead to the large deviations in the MRCI vibrational frequencies. The harmonic frequency differences between the CCSD(T)-F12b/aVTZ PES and the CV5Z QFF are 2-10 cm^{-1}; these relatively smaller differences are reasonable considering the *ab initio* method and basis differences. The QFF harmonic frequencies are typically a little higher than the PES values, and this is a result of including core-correlation in the QFF calculation but not in the PES computations. The CV5Z QFF force constants are tabulated in Table 7.2.

Table 7.1: Computed equilibrium geometries (Å), rotational constants (cm^{-1}), and harmonic frequencies (cm^{-1}) of cyclic C_4 from the PES and *ab initio* calculations.

	PES	CCSD(T)-F12b	QFF	Ref.	
		/aVTZ	CV5Z	CCSD(T)[a]	MRCI[b]
Equilibrium geometires					
R_{12}	1.4481	1.4494	1.4439	1.4492	1.4510
R_{13}	1.5121	1.5110	1.5057	1.5125	1.5204
A_e	1.2277	1.2295	1.2383		1.2149
B_e	0.4599	0.4586	0.4623		0.4599
C_e	0.3346	0.3345	0.3366		0.3336
Harmonic frequencies					
ZPE	2736.8	2730.5	2751.3	2731.4	2815.9
$\omega_1(a_g)$	1267.9	1264.3	1272.2	1262.7	1306.6
$\omega_2(a_g)$	947.4	942.5	949.6	944.2	989.5
$\omega_3(b_{1g})$	1029.4	1030.8	1038.9	1030.8	1079.1
$\omega_4(b_{1u})$	299.4	301.4	306.1	304.7	284.3
$\omega_5(b_{2u})$	537.1	534.3	539.9	534.5	523.1
$\omega_6(b_{3u})$	1392.3	1386.6	1396.0	1385.9	1449.2

[a] Ref. 135 CCSD(T)/pVQZ calculation

[b] Ref. 136 MRCI+Q/pVTZ calculation

Table 7.2: CCSD(T)/CV5Z QFF force constants in symmetry coordinates of cyclic C$_4$. All force constants are given in aJ/Å$^n \cdot rad^m$ where n and m are the orders of bond length coordinates and angle-related coordinates.

ij	F_{ij}	ij	F_{ij}	ij	F_{ij}
11	5.513082	21	-0.503134	22	1.770448
33	0.737645	44	0.068348	55	3.815147
66	4.730368				

ijk	F_{ijk}	ijk	F_{ijk}	ijk	F_{ijk}
111	-15.6237	211	1.1212	221	-3.3525
222	3.5236	331	-3.9763	332	-1.7894
441	-0.1205	442	0.3723	551	-14.2755
552	0.6873	653	7.9852	661	-14.6209
662	0.2381				

$ijkl$	F_{ijkl}	$ijkl$	F_{ijkl}	$ijkl$	F_{ijkl}
1111	36.18	2111	-2.42	2211	6.02
2221	-10.21	2222	15.92	3311	5.94
3321	4.70	3322	1.04	3333	10.55
4411	0.20	4421	-0.89	4422	0.19
4433	-0.37	4444	0.43	5511	37.77
5521	0.16	5522	-5.64	5533	10.68
5544	-0.47	5555	41.66	6531	-20.20
6532	-4.32	6611	35.92	6621	-0.29
6622	0.82	6633	9.45	6644	-0.20
6655	40.01	6666	29.57		

The computed fundamental frequencies of ^{12}C$_4$ using the PES and QFF with both VPT2 and VCI are presented in Table 7.3. In addition, the fundamental IR intensities are computed using MP2/aVTZ methods under double-harmonic approximation. In the order of ν_1 to ν_6, the IR intensities are 0.00, 0.00, 0.02, 50.22, 33.28 and 210.08 respectively. The MM-PES calculations are performed using both 4-mode representation (4MR) and 5-mode representation (5MR). The 4MR VCI results agree with 5MR to within 0.3 cm^{-1}. In addition, we test the convergence with respect to the number of the contracted basis functions and the allowed mode excitations. Less than 0.2 cm^{-1} differences are found for fundamentals, which clearly indicates the VCI basis convergence. In Table 7.3, both VCI (MM-4MR) and VPT2 results are given for the CV5Z QFF. Agreement on six vibrational fundamentals is 0 - 3 cm^{-1}, except ν_2 where the VPT2 energy is about 7 cm^{-1} higher than VCI energy. The ν_2 is in-plane breathing mode altering the bond angles within the original symmetry. The anharmonicity of ν_2 fundamental increases by -4.4 cm^{-1} from -9.8 cm^{-1} (CVTZ) to -12.9 cm^{-1} (CVQZ) and -14.2 cm^{-1} (CV5Z), but the ν_2 harmonic frequency rises faster by 9.3 cm^{-1} from 940.3 cm^{-1} (CVTZ), 944.1 cm^{-1}(CVQZ) to 949.6 cm^{-1} (CV5Z). This partially indicates the deficiency of current CV5Z QFF work, although it is already the most self-consistent and reliable QFF. Carbon-Carbon multibond sensitivities may contribute to this VCI vs. VPT2 discrepancy.

Table 7.3: Computed zero-point energy (ZPE) and fundamentals (cm^{-1}) of cyclic $^{12}C_4$ using different methods

	Harm.	MM-PES		Harm.	MM-4MR	VPT2	Refs.		
	PES	4MR	5MR	QFF	QFF	QFF	CCSD(T)[a]	CCSD(T)[b]	MRCI[c]
ZPE	2736.84	2716.37	2716.36	2751.34	2729.76	2726.35	2713.6	2698.1	
$\nu_1(a_g)$	1267.88	1250.26	1250.26	1272.25	1256.66	1256.36	1248.6	1241.4	1285.9
$\nu_2(a_g)$	947.39	928.32	928.24	949.60	928.62	935.44	926.9	920.7	949.4
$\nu_3(b_{1g})$	1029.39	994.34	994.27	1038.85	1002.40	1002.93	998.7	989.3	981.5
$\nu_4(b_{1u})$	299.44	301.02	300.96	306.10	300.62	302.87	302.3	300.3	279.2
$\nu_5(b_{2u})$	537.15	520.86	520.81	539.91	520.59	522.60	520.2	511.6	522.5
$\nu_6(b_{3u})$	1392.33	1308.91	1308.64	1395.97	1316.57	1314.54	1313.5	1294.2	1378.0

[a] Ref. 135 CCSD(T)/pVTZ variational calculation

[b] Ref. 135 CCSD(T)/pVTZ perturbation calculation

[c] Ref. 136 MRCI+Q/pVTZ perturbation calculation

The VCI fundamental frequencies using the PES differ by less than 9 cm^{-1} compared to the VCI and VPT2 results using the QFF. The differences may partially result from the *ab initio* method, while they could also partially come from the fitting of PES and QFF. Comparing the results in detail, we find that the harmonic frequency of the torsion mode ω_4 on the PES is about 7 cm^{-1} lower than that on the QFF, but the VCI ν_4 fundamentals are almost the same, 301.02 cm^{-1} (PES) vs. 300.62 cm^{-1} (QFF). Conversely, we see enlarged differences of mode 6 for which the harmonic frequency difference is 3.6 cm^{-1} while the MM fundamentals differ by 7.6 cm^{-1}. The PES vs. QFF harmonic frequency differences of the other 4 fundamentals are similar to their corresponding PES vs. QFF variational fundamentals. Comparing to previous studies, overall consistency with Martin's CCSD(T) fundamentals is very good. By contrast, the results of the previous MRCI+Q QFF calculation have about 60 cm^{-1} deviations for some modes. They are mostly the results of the large differences in the MRCI+Q structure and harmonic

frequencies (see Table 7.1), which is mainly attributed to the *ab initio* method and basis limitations.

Martin *et al.* reported the Fermi resonance $\nu_6 = \nu_3 + \nu_5$ raises ν_6 by 9 cm^{-1}.[135] To investigate this, we examined the force constants in Table 7.2. The off-diagonal cubic constant F_{653} is unusually large, 7.9852 aJ/Å^{2}rad. It leads to an exceptionally large k_{356} = -295.9 cm^{-1}. In off-diagonal quartic constants, F_{6531} is also unusually large, i.e. -20.2 aJ/Å^{3}rad, which leads to k$_{1356}$ = -55.0 cm^{-1}. They are highly consistent with the two corresponding normal coordinate QFF constants reported in Ref. 135: -295.0 cm^{-1} and -54.8 cm^{-1}, respectively. This agreement confirms the consistency of both studies. Note that the k_{356} value quoted in Ref. 135 was actually for k_{166}. Combined together, they render significant anharmonicities for ν_6, i.e.$\sim$ 80 cm^{-1}. From the eigenvector analysis of final VCI (MM) states, ν_6 is found strongly coupled with $\nu_3 + \nu_5$. The $\nu_3 + \nu_5$ CI basis contributes about 23% of the ν_6 fundamental wavefunction.

However, on the CV5Z QFF, the regular VPT2 ν_6 fundamental estimated without the explicit Fermi resonance $\nu_6 = \nu_3 + \nu_5$ treatment is 1313.15 cm^{-1}, i.e. just 1.4 cm^{-1} lower than the value we report in Table 7.3, which is estimated with explicit Fermi resonance treatment. The other component, $\nu_3 + \nu_5$, is 1.5 cm^{-1} higher, 1561.53 cm^{-1} (regular VPT2) vs. 1560.14 cm^{-1} (explicit Fermi resonance treatment), vs. 1555.15 cm^{-1} (MM-QFF 4MR). In addition, two more Fermi resonances (Type I) have been explicitly treated together as a polyad: $\nu_1=2\nu_5$ and $\nu_2=2\nu_5$. Compare to VPT2 without including these resonances, ν_1 is reduced by 0.5 cm^{-1} and ν_2 is raised by 1.0 cm^{-1}. Therefore, all the Fermi resonance effects we observed on CV5Z QFF fundamentals are smaller than those reported in Martin *et al.*. It is well known that the resonance effects can vary from one QFF to another. Although the ν_1, ν_2 and ν_6 given in Table 7.3 are computed with the Fermi resonances explicitly included, the regular VPT2 results are considered similarly

reliable.

Combination and overtone excitations of C_4 given in Table 7.4 are computed with regular VPT2, i.e. no explicit Fermi resonance treatment is included. We obtain good overall consistency between the VCI (MM) and VPT2 levels computed on the CV5Z QFF. For most energy levels, the agreement is within 10 cm^{-1}, and usually the VPT2 energies are higher. For the lowest state energies given in Table 7.4, the 3-5 cm^{-1} differences between MM and VPT2 are totally consistent with the fact that our VPT2 treatment does not go beyond second-order vibrational perturbation theory. There are only two exceptions: $\nu_3 + \nu_6$ and $\nu_5 + \nu_6$. For $\nu_3 + \nu_6$ and $\nu_5 + \nu_6$, the MM-QFF energies are higher than the VPT2-QFF energies by 13-20 cm^{-1}, while the VPT2-QFF energies agree well with the corresponding MM-PES energies. This could be accidental. For the MM-PES results, we obtain good agreement between the 4MR and 5MR results as well. Comparing the MM-QFF to MM-PES, most differences are within 5 - 15 cm^{-1}. In addition, we note the strong coupling of $2\nu_6$ with $2\nu_3 + 2\nu_5$ and $\nu_6 + \nu_3 + \nu_5$. The MM calculations give two $2\nu_6$ states separated by about 200 cm^{-1}, as shown in Table 7.4. The leading CI coefficients in both $2\nu_6$ states are about 0.67. In this situation, assignment of $2\nu_6$ becomes problematic due to the severe mixing, and the labels are considered somewhat arbitrary.

Table 7.4: Low-lying combinations and overtones of cyclic ^{12}C$_4$ (cm^{-1})

Assignment	MM-PES		MM-QFF	VPT2-QFF
	4MR	5MR	4MR	
$2\nu_4$	606.69	606.58	603.21	608.67
$\nu_4 + \nu_5$	822.06	821.93	818.93	824.44
$2\nu_5$	1036.72	1036.61	1035.27	1037.84
$\nu_2 + \nu_4$	1232.92	1229.41	1225.84	1232.20
$\nu_3 + \nu_4$	1290.72	1290.48	1296.18	1299.06
$\nu_2 + \nu_5$	1439.13	1438.76	1435.14	1444.90
$\nu_3 + \nu_5$	1549.74	1549.66	1555.15	1561.52
$\nu_1 + \nu_4$	1556.93	1553.26	1559.61	1561.33
$\nu_6 + \nu_4$	1605.78	1604.97	1611.58	1611.72
$\nu_1 + \nu_5$	1773.20	1773.09	1779.88	1785.04
$\nu_6 + \nu_5$	1787.13	1786.16	1797.19	1784.11
$2\nu_2$	1853.43	1853.11	1855.11	1861.14
$\nu_3 + \nu_2$	1918.21	1918.01	1925.05	1923.23
$2\nu_3$	1984.99	1984.69	2000.95	2003.75
$\nu_1 + \nu_2$	2176.93	2173.39	2183.01	2184.35
$\nu_2 + \nu_6$	2218.54	2216.13	2225.79	2234.58
$\nu_1 + \nu_3$	2232.38	2232.20	2245.38	2245.56
$\nu_3 + \nu_6$	2247.65	2246.83	2264.19	2244.26
$2\nu_1$	2495.22	2495.17	2508.59	2508.82
$\nu_1 + \nu_6$	2547.08	2546.36	2561.28	2560.05
$2\nu_6$ [1]	2589.08	2587.19	2607.76	2617.20
$2\nu_6$ [2]	2794.38	2793.19	2810.37	

[1] Lower energy component of ν_6 overtone

[2] Higher energy component of ν_6 overtone

We can obtain the rovibration energies of cyclic C_4 from the MM and the SPECTRO calculations. The rovibration energies of $J = 1$ and $J = 2$ levels computed with MM-PES and VPT2-QFF approaches are given in Tables 7.5, where we give $E_\nu(J = 1, 2) - E_\nu(J = 0)$. In addition to spectroscopic constants, SPECTRO also computes the ro-vibrational energy levels through diagonalizing the rotational energy matrices for both S and A reduced Hamiltonians. The vibrationally-dependent spectroscopic constants can be found in the SM. Note the differences between S-reduced and A-reduced Hamiltonian energy matrices are much smaller than 1E-6 cm^{-1}, so we do not need to label them. MM calculation employs a different method, in which the ro-vibrational energies are obtained by diagonalizing the full ro-vibrational Watson Hamiltonian matrices with nMR potential representation. We can derive the effective rotational constants from the MM ro-vibrational energies. Cyclic C_4 is not a rigid symmetric top, so there is no exact expression that relates the ro-vibrational energies of MM with the effective rotational constants. An approximate expression to represent the energy levels of the asymmetric rigid rotor is given by:[150]

$$E = \frac{1}{2}(A + C)J(J + 1) + \frac{1}{2}(A - C)E_\tau \qquad (7.1)$$

where E_τ is tabulated according to the asymmetry parameter κ, which is defined as $(2B - A - C)/(A - C)$. κ is equal to about -0.72 for the cyclic C_4, and the values of E_τ can be found in Ref. 150.

Table 7.5: Ro-vibrational energies of $J = 1$ and $J = 2$ from 4MR MM calculation with the PES and VPT2 calculation with the QFF, and the energies are shown as $\nu_{i(J=1,2)} - \nu_{i(J=0)}$. (cm^{-1})

		$1_{1,0}$	$1_{1,1}$	$1_{0,1}$	$2_{2,0}$	$2_{2,1}$	$2_{1,1}$	$2_{1,2}$	$2_{0,2}$
MM	ZPE	1.6701	1.5449	0.7898	5.6533	5.6400	3.3748	2.9994	2.3561
	ν_1	1.6668	1.5412	0.7872	5.6462	5.6318	3.3686	2.9909	2.3479
	ν_2	1.6670	1.5405	0.7884	5.6421	5.6285	3.3707	2.9914	2.3515
	ν_3	1.6661	1.5395	0.7857	5.6422	5.6280	3.3652	2.9853	2.3435
	ν_4	1.6674	1.5426	0.7920	5.6366	5.6278	3.3760	3.0017	2.3670
	ν_5	1.5919	1.4675	0.7866	5.3521	5.3376	3.2907	2.9176	2.3454
	ν_6	1.6578	1.5327	0.7861	5.6165	5.5995	3.3588	2.9817	2.3432
VPT2	ZPE	1.6912	1.5653	0.7950	5.7321	5.7179	3.4071	3.0295	2.3708
	ν_1	1.6850	1.5593	0.7933	5.7095	5.6953	3.3974	3.0203	2.3658
	ν_2	1.6889	1.5620	0.7947	5.7213	5.7068	3.4052	3.0245	2.3697
	ν_3	1.6870	1.5608	0.7917	5.7181	5.7038	3.3965	3.0180	2.3608
	ν_4	1.6626	1.5371	0.7974	5.6164	5.6018	3.3829	3.0064	2.3776
	ν_5	1.7177	1.5920	0.7915	5.8413	5.8276	3.4263	3.0493	2.3609
	ν_6	1.6845	1.5591	0.7924	5.7088	5.6947	3.3949	3.0184	2.3630

According to this expression, effective A and C can be calculated through linear least square fitting from the MM-PES ro-vibrational energies. Here if the effective rotational constants from SPECTRO are substituted into this expression to calculate the ro-vibrational energies, good consistency can be obtained by comparing with the MM-PES energies, with differences less than 0.4 cm^{-1}. The differences are partly due to the simple approximation in the formula, they are also traced to differences in the equilibrium

structures between the QFF and PES.

Finally, we consider the cyclic C_4 isotopologues. The MM and SPECTRO results for the two single ^{13}C-substituted isotopologues are shown in Table 7.6, including the zero-point structure, 6 vibrational fundamentals, and vibrationally averaged rotational constants. As seen, good consistency is found between the three approaches for both isotopologues. We expect similar consistency for the fundamentals. The VPT2/QFF isotopic shifts are explicitly included as it is usually more accurate than the absolute values of fundamental frequencies. Compare to $^{12}C_4$, the shifts are relatively small for the bend and torsion modes, decreasing by less than 5 cm^{-1}. For the stretching modes, for example mode ν_1 and ν_6, the differences can be as large as about 13 cm^{-1} for single ^{13}C isotopologues. Note the same Fermi resonance treatments are included in the VPT2 analysis on both isotopologues, although their effects are small, i.e. about 1 cm^{-1}.

Table 7.6: The VPT2 zero-point vibrationally averaged structures (Å, deg), rotational constants (cm^{-1}), zero-point energy (ZPE) (cm^{-1}), fundamentals (cm^{-1}) of single ^{13}C isotope substituted cyclic C_4, and shifts of vibration energies compared to $^{12}C_4$ based on VPT2 results.

	Zero-point			Vibrational Energies				Shift
				Harm-QFF	MM-PES	MM-QFF	VPT2-QFF	
$^{13}CCCC$	$R_{12}=R_{14}$	1.4492	ZPE	2721.98	2687.64	2699.84	2697.62	-28.73
	$R_{23}=R_{34}$	1.4494	ν_1	1258.93	1237.12	1243.34	1243.59	-12.77
	$\angle_{123}$	62.960	ν_2	941.08	920.77	920.37	922.18	-13.26
	A_0	1.1825	ν_3	1023.51	980.25	987.80	988.67	-14.26
	B_0	0.4605	ν_4	303.13	298.09	297.66	299.96	-2.91
	C_0	0.3309	ν_5	534.39	515.66	515.22	517.38	-5.22
			ν_6	1382.92	1296.76	1303.83	1302.39	-12.15
$C^{13}CCC$	$R_{12}=R_{23}$	1.4493	ZPE	2726.96	2692.60	2704.75	2702.47	-23.88
	$R_{34}=R_{14}$	1.4493	ν_1	1260.34	1238.56	1243.90	1244.33	-12.07
	$\angle_{143}$	62.965	ν_2	938.59	917.23	917.54	919.34	-10.77
	A_0	1.2308	ν_3	1033.43	989.33	996.97	997.88	-5.05
	B_0	0.4424	ν_4	303.13	298.10	297.67	299.98	-2.89
	C_0	0.3249	ν_5	534.60	515.96	515.50	517.67	-4.93
			ν_6	1383.82	1299.15	1306.24	1304.52	-10.02

7.4   Summary and Conclusions

We reported a CCSD(T)-F12b/aug-cc-pVTZ potential energy surface and a CCSD(T)/cc-pCV5Z quartic force field of the singlet cyclic C_4. Three different methods were adopted to calculate the vibrational states of cyclic C_4: variational calculations (VCI) using MUL-TIMODE with the PES and the QFF, and second-order perturbation calculation using

SPECTRO with the QFF. Even though the PES and QFF were constructed using different *ab initio* methods and basis sets, the VCI calculations of PES and QFF are in very good agreement with each other for fundamentals, overtones, and combinations. On the CV5Z QFF, the VPT2 fundamentals agree excellently with the variationally calculated energies. From the VCI calculations, the coupling between the mode ν_6 and $\nu_3 + \nu_5$ combination is quite strong, but VPT2 calculations with the Fermi resonance treatment explicitly included only change the ν_6 fundamental by 1.4 cm^{-1}. The other two Fermi resonance effects are less than 1 cm^{-1}. So we use regular VPT2 analysis for the combinations and overtones. In addition, ro-vibrational energies for $J = 1$ and $J = 2$ were computed using 4MR MM calculations on the PES and VPT2 calculations with the QFF. Spectroscopic constants including vibrationally averaged structures were determined by VPT2 method and reported for the main isotopologue as well as two ^{13}C singly-substituted isotopologues. The accuracy of vibrational fundamentals is estimated to be better than 5 cm^{-1}. Rotational constant deviations should be within 0.1-0.5%. Other quartic centrifugal distortion constants may carry 5-10% deviations. The results reported in this study may help in identification of cyclic C$_4$ in future experimental analyses or astronomical observations.

Chapter 8

Infrared Spectra of CH$_3$CHOO

8.1 Introduction

In Chapter 5, we presented the importance of Criegee intermediates in the atmosphere, and the reaction dynamics studies of unimolecular decay of *syn*-CH$_3$CHOO. The Criegee intermediates have also been studied many times from the spectroscopic perspective. The simplest Criegee intermediate, CH$_2$OO, has now been detected with ultraviolet depletion[70], ultraviolet absorption[151], infrared absorption[152] and microwave spectroscopy[153,154]. The kinetics of reactions of CH$_2$OO with various atmospheric species have been directly investigated with some of these detection methods.[71,155–158].

The methyl substituted Criegee intermediate, CH$_3$CHOO, is an intermediate of ozonolysis with 2-alkenes (such as trans-2-butene) and serves as a prototype to understand various fundamental issues in larger Criegee intermediates. CH$_3$CHOO exists in two conformers, *syn*-CH$_3$CHOO and *anti*-CH$_3$CHOO, with the former more stable than the latter by $\sim$ 15 kJ/mol.[88] Because of a large barrier $\sim$ 160 kJ/mol, the interconversion between *syn*-CH$_3$CHOO and *anti*-CH$_3$CHOO is unlikely. Taatjes et al.[72] produced CH$_3$CHOO and

detected both CH$_3$CHOO conformers with photoionization. The conformer-dependent reactivity of *syn-* and *anti-* conformers were detected with specific atmospheric compounds. The ultraviolet depletion[78] and ultraviolet absorption spectra[151] of CH$_3$CHOO were studied in experiments, which yielded a broad feature without structure and provided no information about the conformation of the CH$_3$CHOO carrier. The microwave spectroscopy was successful in providing structural information[87], but without any vibrational insights. Liu et al.[77] employed infrared activation of cold CH$_3$CHOO to produce OH and assigned several absorption features in the region 5,600-6,100 cm^{-1} to be the CH-overtone and combination bands of *syn-*CH$_3$CHOO; no bands of *anti-*CH$_3$CHOO were identified.

So far most theoretical studies have focused on CH$_2$OO.[152,159,160] For CH$_3$CHOO, several *ab initio* calculations were reported focusing on the stationary points.[78,87,88] The only available vibrational calculation is the perturbation theory analysis and reaction path relevant to the action spectrum of *syn-*CH$_3$CHOO mentioned above.[77] It is thus desirable to thoroughly study the vibrations of the two conformers of CH$_3$CHOO in both experiment and theory.

As far as we know, no full-dimensional potential energy surface (PES) exists for CH$_3$CHOO. These are challenging systems owing to their high dimensionality. Because of high interversion barrier, *syn-* and *anti-*CH$_3$CHOO can be viewed as separate species. In this chapter, we report full-dimensional PESs and DMSs for the *syn-* and *anti-*conformers of CH$_3$CHOO in spectroscopic accuracy. Wavefunctions and energies of the zero-point state for these conformers are determined using Diffusion Monte Carlo (DMC) calculations. Vibrational self-consistent field and configuration-interaction (VSCF/VCI) calculations of the IR spectra are performed using MULTIMODE (MM) for each conformer. Here we first present the survey spectrum of energy up to 6200 cm^{-1}. In addition, we

collaborate with experimental measurement, and more accuracy and detailed calculations are performed focusing on the fundamental states of CH$_3$CHOO in the energy range of 830 - 1550 cm^{-1}.

8.2 Potential Energy Surface of CH$_3$CHOO Isomers

Following the procedure of constructing new PES, around 20,000 configurations are sampled by running classical direct-dynamics calculations starting from the minimum and methyl torsion saddle point (SP) and by randomly sampling around the stationary points. The electronic energies are calculated using the explicitly correlated coupled-cluster single and double excitation method that includes a perturbation treatment of triple excitations (CCSD(T)-F12b),[54,55] with the aug-cc-pVDZ basis for the C and O atoms and cc-pVDZ basis for H atoms, as implemented in the MOLPRO package.[58]

The PES of CH$_3$CHOO is 18 dimensional, and is invariant with permutation of the four H atoms, two C atoms, and two O atoms. The maximum polynomial order for each PES fit is 5, and the number of linear coefficients is 5801. The cut-off energy for the database for the PES fits is roughly 35 kcal/mol (12,215 cm^{-1}). We used 18,000 and 17,901 points for *syn*- and *anti*-CH$_3$CHOO PES fitting, and the fitting RMS are 0.119 cm^{-1} and 0.123 cm^{-1} respectively. Figure 8.1 shows the number of configurations in different energy ranges and the corresponding RMS error. Energies of the minimum and torsional SP, and harmonic frequencies for *syn*- and *anti*-CH$_3$CHOO are precisely described by the fitted PESs, as shown in Table 8.1 and 8.2 respectively, along with results from direct CCSD(T)-F12b calculations. The deviations with *ab initio* results of 5 cm^{-1} or less indicate the high precision of the fitted PESs.
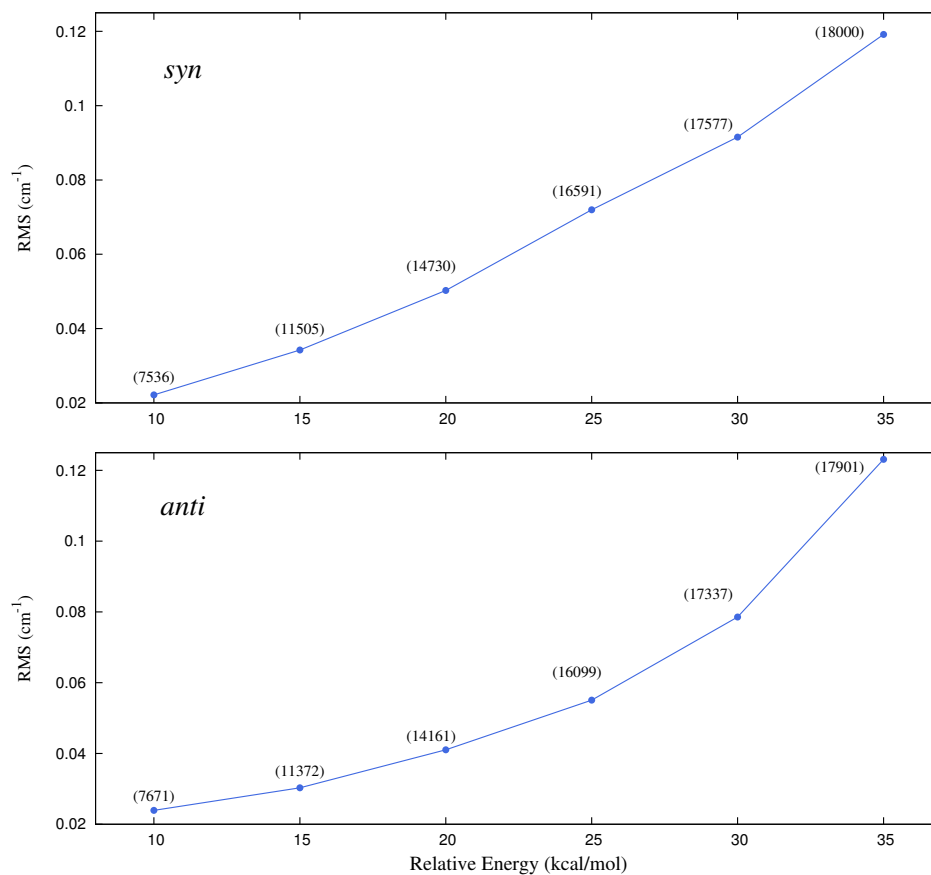
Figure 8.1: Root-mean-square (RMS) of the *syn-* and *anti-*CH$_3$CHOO PES fitting error vs. relative energy with respect to minimum. The values in parentheses are the number of configurations in the energy range.

Table 8.1: The comparison of energies (cm^{-1}) and harmonic frequencies (cm^{-1}) of *syn*-CH₃CHOO between PES and *ab initio* calculation.

			Minimum		SP	
			ab initio	PES	ab initio	PES
Eng.			0.0	0.0	730.3	730.4
mode	sym.	description				
ν_1	A′	carbonyl oxide C-H str.	3204.2	3206.0	3194.8	3196.8
ν_2	A′	methyl in-plane C-H str.	3161.2	3161.2	3177.2	3176.7
ν_3	A′	methyl out-plane sym. C-H str.	3029.5	3030.5	3040.7	3036.7
ν_4	A′	C-O str.	1527.4	1528.3	1539.7	1538.4
ν_5	A′	methyl sym. scissor	1466.5	1468.0	1487.7	1484.6
ν_6	A′	methyl umbrella	1397.7	1396.0	1388.8	1389.2
ν_7	A′	carbonyl oxide in-plane C-H wag	1316.6	1317.9	1328.9	1329.2
ν_8	A′	C-C-O bend	1115.4	1115.8	1157.8	1156.4
ν_9	A′	C-C str.	977.6	977.5	929.8	933.2
ν_{10}	A′	O-O str.	922.1	922.7	883.0	875.4
ν_{11}	A′	C-O-O bend	677.6	677.8	653.3	648.0
ν_{12}	A′	C-C-O-O ring closure	308.0	307.5	335.9	332.7
ν_{13}	A″	methyl out-plane asym. C-H str.	3084.7	3085.3	3103.7	3105.8
ν_{14}	A″	methyl asym. scissor	1449.2	1449.9	1449.8	1446.0
ν_{15}	A″	C-C-O out-plane bend	1031.3	1034.0	1037.7	1046.2
ν_{16}	A″	carbonyl oxide out-plane C-H wag	720.6	721.0	757.7	752.4
ν_{17}	A″	C-C-O-O out-plane ring dist.	447.7	448.3	430.8	435.1
ν_{18}	A″	methyl torsion	201.8	206.0	175.9i	177.1i

Table 8.2: The comparison of energies (relative to *syn*-CH$_3$CHOO) and harmonic frequencies (cm^{-1}) of *anti*-CH$_3$CHOO between PES and *ab initio* calculation.

			Minimum		SP	
			ab initio	PES	ab initio	PES
Eng.			1274.2	1274.2	1700.9	1700.9
mode	sym.	description				
ν_1	A$'$	carbonyl oxide C-H str.	3168.3	3168.6	3171.2	3167.6
ν_2	A$'$	methyl in-plane C-H str.	3154.0	3153.6	3152.4	3156.1
ν_3	A$'$	methyl out-plane sym. C-H str.	3039.2	3039.3	3047.0	3056.1
ν_4	A$'$	C-O str.	1533.8	1534.6	1507.2	1515.8
ν_5	A$'$	methyl sym. scissor	1466.0	1466.5	1483.8	1485.5
ν_6	A$'$	methyl umbrella	1419.8	1419.8	1414.7	1408.7
ν_7	A$'$	carbonyl oxide in-plane C-H wag	1321.3	1321.5	1318.1	1312.4
ν_8	A$'$	C-C-O bend	1159.2	1159.4	1147.9	1142.3
ν_9	A$'$		956.0	957.0	1002.1	1003.0
ν_{10}	A$'$		904.6	904.9	890.6	890.9
ν_{11}	A$'$	C-O-O bend	560.4	560.4	558.9	556.8
ν_{12}	A$'$	C-C-O-O in-plane wag	324.5	324.3	325.1	326.1
ν_{13}	A$''$	methyl out-plane asym. C-H str.	3103.6	3103.4	3115.6	3111.6
ν_{14}	A$''$	methyl asym. scissor	1476.8	1477.1	1470.2	1469.0
ν_{15}	A$''$	C-C-O out-plane bend	1053.7	1054.2	1053.2	1064.7
ν_{16}	A$''$	carbonyl oxide out-plane C-H wag	850.2	848.3	822.7	819.8
ν_{17}	A$''$	C-C-O-O out-plane ring dist.	251.0	251.3	242.1	242.6
ν_{18}	A$''$	methyl torsion	156.2	155.7	171.1i	171.3i

The dipole moment components for *syn-* and *anti-*CH$_3$CHOO were calculated using the MP2 method at the same geometries used to generate the PESs for *syn-* and *anti-*CH$_3$CHOO. The DMSs were also fitted using the invariant polynomial method, as discussed in Chapter 2. The RMS fitting errors for DMSs are 0.0007 a.u. and 0.0009 a.u for *syn-* and *anti-*CH$_3$CHOO respectively.

The internal methyl rotor is a potentially complex motion. Specifically, the torsional angle associated with this is motion, τ, is defined as the average of three dihedral angles H^1-C^1-C^2-H$^{2/3/4}$. The relaxed potential as a function of τ was obtained by a constrained minimization at a given τ with respect to the other 17 degrees of freedom on the PESs. The resulting relaxed potentials for *syn* and *anti-*CH$_3$CHOO are given in Figure 8.2 . The geometries at minimum and torsion SP are given as well; these are of C$_s$ symmetry. As seen, the torsion barrier height of the *syn-*conformer is larger than that of *anti*, which indicates that the interaction between protons in the methyl group and the terminal oxygen atom in *syn-*CH$_3$CHOO hinders the methyl torsion motion. These barrier heights agree well with a previous *ab initio* calculation, which gives the torsion barrier height of 748 cm^{-1} and 402 cm^{-1} for *syn* and *anti* respectively.[87]
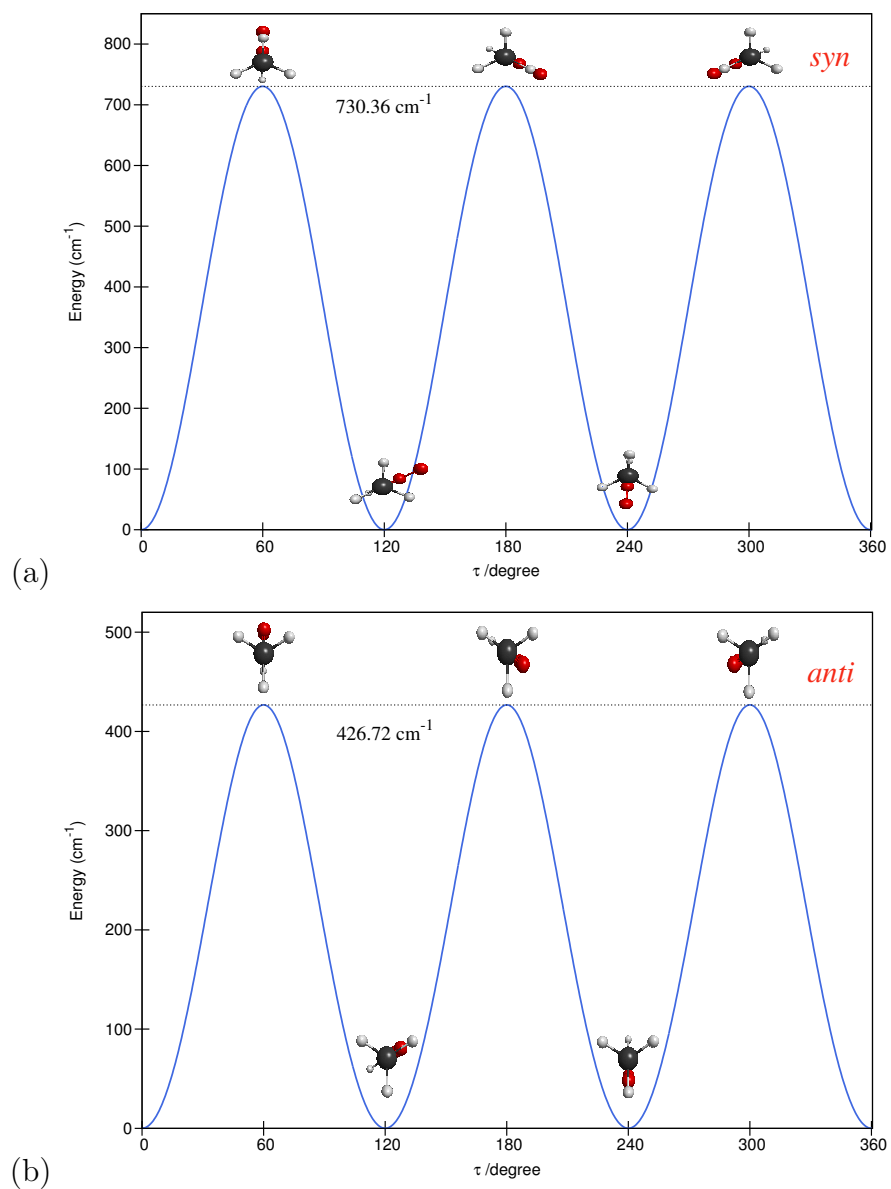
Figure 8.2:   Fully relaxed path of *syn-* and *anti-*CH$_3$CHOO along the methyl torsion angle.

8.3 Diffusion Monte Carlo

The ground vibrational-state wavefunctions and energies of the *syn-* and *anti-*conformer were determined using DMC calculations.[26,27] For each calculation, 15,000 walkers were propagated for 15,000 steps with an imaginary time step equal to 5 a.u. The reference configuration was set to the equilibrium geometry. For each DMC trajectory the first 5,000 steps were used to equilibrate the system, and the remaining 10,000 steps were used to obtain the ZPE. The final ZPE and uncertainty were then determined by calculating an average of five trajectories run for each conformer.

From the DMC calculations, the calculated ZPEs of *syn-* and *anti-*CH$_3$CHOO are 12851.7±4.3 and 12773.9±4.5 cm^{-1}, respectively, relative to their respective minima. The *syn* conformer is more stable than *anti* by 1274.2 cm^{-1} and considering the ZPEs, the energy difference between *syn* and *anti* is 1196.4 cm^{-1}. This indicates that at room temperature the *syn*-conformer is substantially more populated than the *anti* one. In addition to determining the ZPEs, the DMC calculations allow the visualization of ground state wavefunction. The wavefunction amplitude can be calculated using the walkers from DMC trajectory, and visualized as an isosurface. The isosurfaces of the ground state wavefunctions for the two conformers are shown in Figure 8.3. From the plots, we observe that the amplitude of the methyl torsion motion is localized at the minimum for both conformers, although more so for *syn* than *anti*. This is reasonable given the smaller torsion barrier height of *anti*. However, both results indicate that at least for the ground torsional state the conformers do not exhibit large amplitude torsional motion. From the perspective of spectroscopy this means that the well-known CH$_3$-torsional tunneling splittings can be neglected in the survey and fundamental IR spectrum describing transitions from the ground vibrational state. In fact, the tunneling splitting for the *syn*

conformer has been estimated experimentally to be in the kilohertz range[87], confirming

that tunneling can be neglected in calculations of survey spectra we present here.
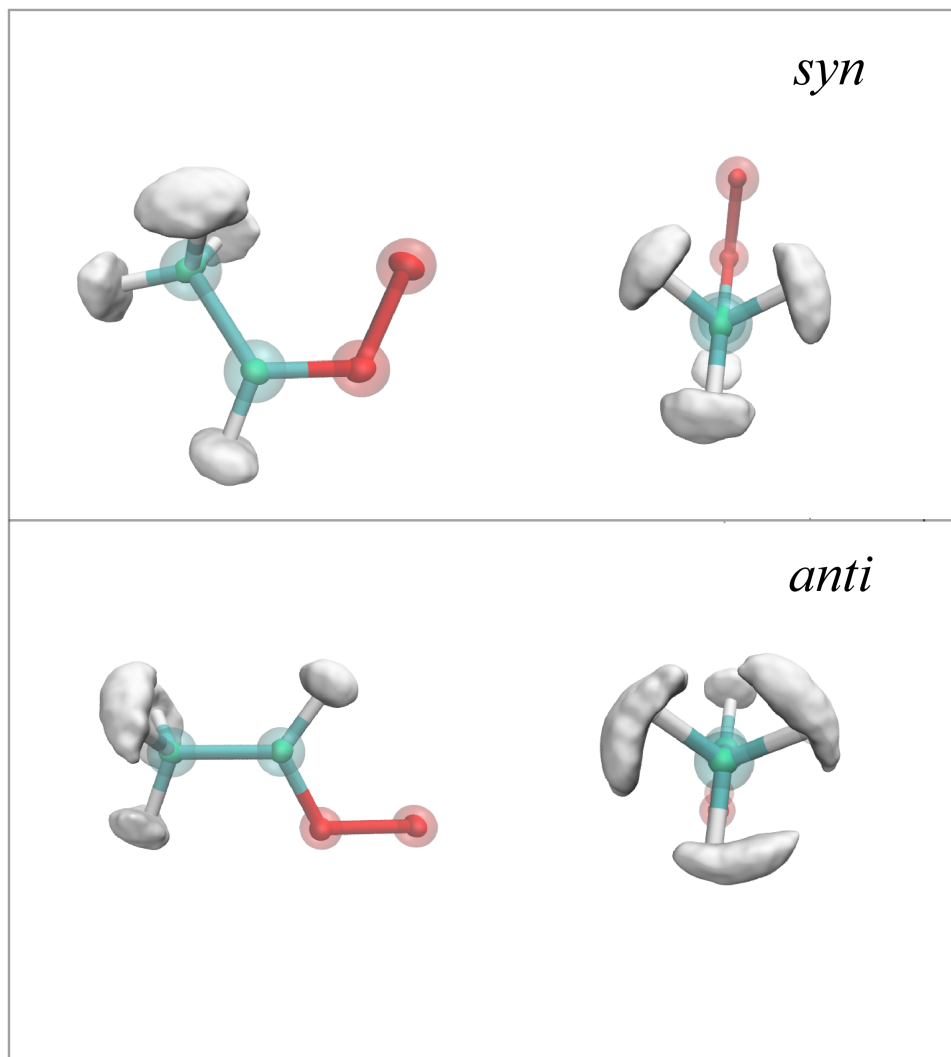
Figure 8.3:   Isosurfaces of ground state wavefunction for both *syn-* and *anti-* conformers, shown in two different views respectively.

8.4   Survey Spectrum of CH$_3$CHOO

The calculations of the IR spectra were done using the MULTIMODE program. The calculations are based on the Watson Hamiltonian in mass-scaled normal coordinates. This version is appropriate for semi-rigid molecules and so not obviously applicable to *syn*- and *anti*-CH$_3$CHOO, which have an internal methyl rotor. However, from an analysis of the DMC wavefunctions and comparisons of the MM ZPEs with the rigorous DMC, the wave function of ground torsional state is localized, and justifies the semi-rigid approach. For CH$_3$CHOO, the exact potential is 18-dimensional, and we used 4MR in the MM calculation in this study. Eleven primitive harmonic-oscillator basis were included for each mode in the initial VSCF step. Then the VCI calculation uses the virtual states as basis functions, and the number of basis functions in the computationally intensive VCI step is restricted by the maximum quanta in each mode and maximum sum of excitation of all modes. In the survey spectrum calculation, we included all the 18 modes of CH$_3$CHOO. Therefore, the size of basis set and maximum excitation were limited to relatively small values considering the expense of calculation. In the VCI, we allowed the 4-mode excitation simultaneously, and the sum of quanta in all modes was restricted to 5. C$_s$ symmetry was applied in the MM calculation. The sizes of each VCI matrix for the two C$_s$ blocks are 12,759 and 11,719.

The IR spectrum intensity was calculated using standard expression in terms of dipole transition matrix elements. These were determined by numerically integrating the matrix elements involving the calculated ground and vibrationally excited state eigenfunctions and the dipole moment components. No approximations were made to these components, and so the spectrum consists of fundamental, overtone, and combinations states.

The spectra were obtained in 18-mode VSCF/VCI calculations using the MM pro-

gram, with the so-called 4-mode representation of the potential. Note that while these are not "exact" calculations, they are expected to be within 5-10 cm cm^{-1} of exact results for this high dimensional system. One meaningful comparison that can be made is for the ZPEs from MM. These are 12859.0 cm^{-1} and 12784.5 cm^{-1} for the *syn-* and *anti-*conformers, respectively, in good agreement with DMC results. (Note the differences of roughly 8 cm^{-1} almost certainly imply differences of this magnitude or less for transition energies of relevance to the IR spectra.)

The spectra for the *syn-* and *anti-*conformers from 0 to 6200 cm^{-1} are shown in Figure 8.4. Peaks corresponding to fundamental excitations are labeled as such. Peaks in the 3000 cm^{-1} region correspond to the four CH-stretches and clearly peaks above these correspond to combination and overtone bands. These spectra show similarities and also important differences, and should be of value to experimental investigations of these spectra. In addition, expanded views of these spectra in the range 5500-6100 cm^{-1} are also given. The region of the spectrum is quite dense, and the one for *syn*-CH$_3$CHOO is of special interest as the action spectrum has been recently reported in this range.[77] That spectrum (which detects the OH product as the wavelength varies) is related to but of course not the same as the IR spectrum shown here. Nevertheless, there are some striking similarities. The intense peak around 6030 cm^{-1}, which is the overtone state of ν_1 mode, agrees well with a peak in the action spectrum. In addition, the strong absorption around 5910 cm^{-1} shows similarity with the action spectrum. A thorough analysis of the action spectrum needs to consider unimolecular dissociation dynamics of *syn*-CH$_3$CHOO, and such studies, which are highly challenging, will hopefully be conducted in the future. For completeness, the corresponding expanded view for *anti*-CH$_3$CHOO is also given. However, the barrier for dissociation to produce OH is higher than *syn*-CH$_3$CHOO and so much less OH is expected for *anti*-CH$_3$CHOO in this spectral range. Finally, it is

worth noting some similarities to the calculated spectral features in CH$_2$OO reported recently[160]. However, that calculated (and measured) spectrum did not extend beyond roughly 3100 cm^{-1}.

(a)

(b)
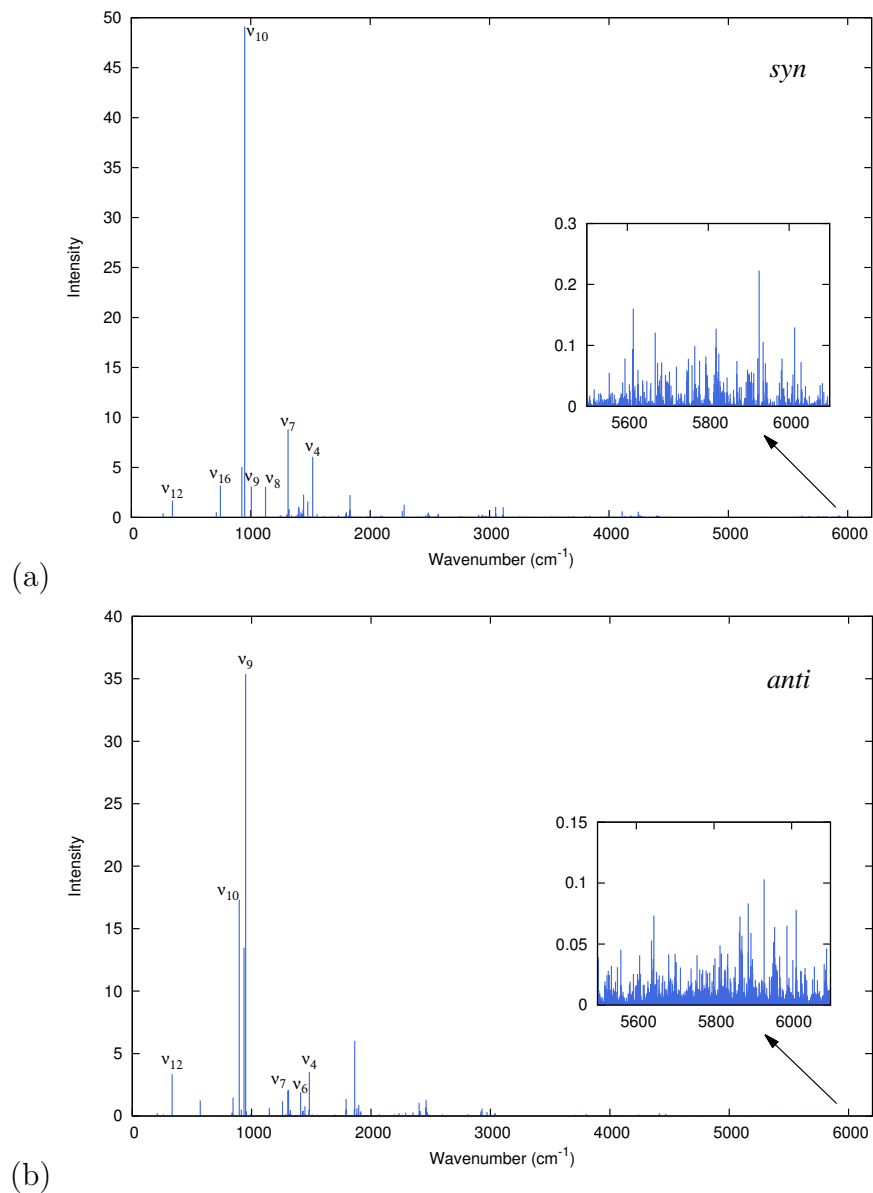
Figure 8.4:   Infrared survey vibration spectra of *syn*- and *anti*-CH$_3$CHOO in the energy from 0 to 6200 cm^{-1}. Expanded views of the spectra in 5500 - 6100 cm^{-1} range are given as well.

Rotation constants of the ground vibrational state of *syn*-CH$_3$CHOO and *anti*-CH$_3$CHOO were determined exactly from differences of rigorous $J=1$ and 0 energies. The rotation

constants of the ground vibrational state for *syn*-CH$_3$CHOO have been determined exper-
imentally,[87] and these are compared with the calculated ones in Table 8.3. As seen, abso-
lute differences between calculated ground state and experimental constants are 0.0015,
0.0033 and 0.0006 cm^{-1} for A_0, B_0, and C_0, respectively for *syn*-CH$_3$CHOO. The rotation
constants for the *syn*-conformer show significant differences compared to those for the
anti-conformer, as expected based on the large differences in the equilibrium structures.

Table 8.3: The equilibrium and zero-point rotation constants of *syn*- and *anti*-CH$_3$CHOO and comparison with previous results.

		Equ.			Zero-point	
			Ref.[1]			Exp.[2]
syn	A_e	0.5884	0.5875	A_0	0.5881	0.5866
	B_e	0.2401	0.2399	B_0	0.2412	0.2379
	C_e	0.1760	0.1758	C_0	0.1774	0.1768
anti	A_e	1.6299	1.6296	A_0	1.6249	
	B_e	0.1486	0.1485	B_0	0.1541	
	C_e	0.1398	0.1396	C_0	0.1452	

[1] Ref. 87, CCSD(T)-F12a/aVTZ calculation results.

[2] Ref. 87, rotation constants determined from pure rotation
spectroscopy of *syn*.

8.5   Spectral Analysis of CH$_3$CHOO in Fundamental Range

In experimental measurement, even though only one H atom of CH$_2$OO was replaced with a methyl group to form CH$_3$CHOO, the infrared spectrum of the latter is expected to be much more complicated, because both syn- and anti-conformers contribute to the infrared absorption. In addition, the methyl group introduces low-energy vibrational modes such as the CH$_3$ torsion (internal rotation) which are populated with several vibrational quanta even at ambient temperatures; hot bands might consequently play important roles in the observed spectrum. Furthermore, the internal rotation of the methyl moiety may introduce torsional splitting in vibrational bands. Consequently, spectral identification and simulation of observed bands of CH$_3$CHOO are expected to be difficult. In this respect, sophisticated quantum-chemical calculations are essential to assist the spectral simulation and assignments.

In the experimental study, the transient infrared spectra of *syn-* and *anti-*CH$_3$CHOO were measured using a step-scan Fourier-transform spectrometer in the energy range of 830-1550 cm^{-1}. Guided and supported by high-level full-dimensional quantum calculations, rotational contours of the four observed bands are simulated successfully and provide definitive identification of both conformers.

In the experiment, a step-scan FTIR spectrometer was used to record time-resolved infrared spectra. A flowing mixture of CH$_3$CHI$_2$ produced CH$_3$CHI using laser photodissociation at 308 nm, which subsequently reacted with O$_2$ to form CH$_3$CHOO. The partial infrared absorption spectrum (830-1550 cm^{-1}) of a flowing mixture of CH$_3$CHI$_2$/N$_2$/O$_2$ at 328 K exhibits an intense absorption line of CH$_3$CHI$_2$ (Figure 8.5a). On irradiation with light at 308 nm, the absorption of CH$_3$CHI$_2$ decreased because of photolysis, whereas

new bands marked $A_1 - A_5$ appeared in the difference spectrum recorded 0-2 μs after laser irradiation (Figure 8.5b). The A_5 band was partially interfered with by the absorption of the precursor and the product acetaldehyde, but its sharp Q-branch is quite characteristic and can be readily recognized. These new lines decreased in intensity, as shown in Figure 8.5c where 68 μs was recorded after ultraviolet irradiation and disappeared after $\sim$ 25 μs. To minimize interference from other products, we subtracted the spectrum recorded during 16.0-19.8 μs from these two spectra and stripped the contributions from the precursor and acetaldehyde, as shown in Figure 8.5d,e.
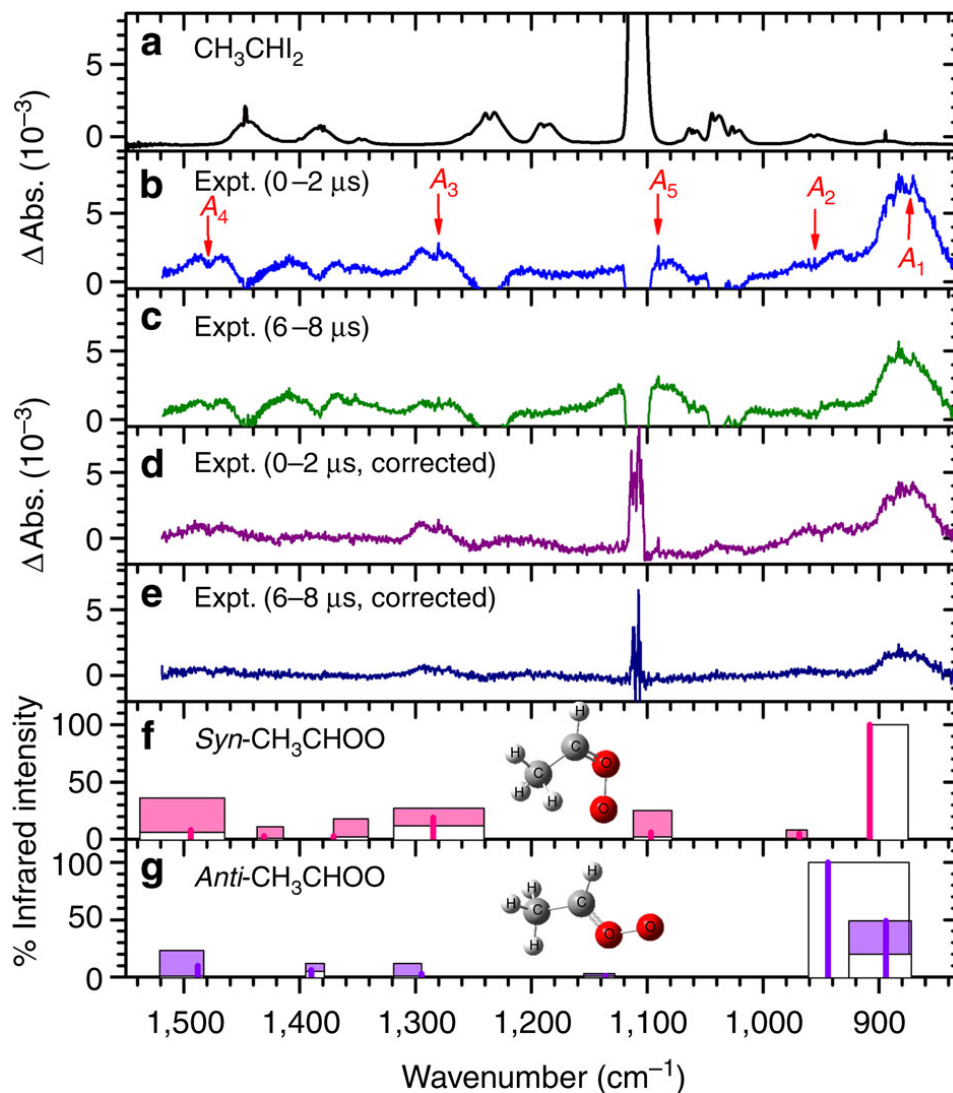
Figure 8.5:   Comparison of observed spectra with predicted stick spectra. (a) Absorption spectrum of a flowing mixture of CH$_3$CHI$_2$/N$_2$/O$_2$ before photolysis. (b) Difference spectra recorded 0-2 μs and (c) 6-8 μs after irradiation of the sample at 308 nm. (d) Corrected spectra recorded 0-2 μs and (e) 68 μs after subtraction of the spectrum recorded at 16.0-19.8 μs and removal of the contributions of the precursor CH$_3$CHI$_2$ and stable product acetaldehyde. Resolution of all spectra is 0.5 cm^{-1}. New features are marked with arrows and labeled as A_1-A_5. (f) Possible ranges of anharmonic vibrational wavenumbers and infrared intensities of syn-CH$_3$CHOO and (g) $anti$-CH$_3$CHOO predicted with various methods shown as filled boxes; those predicted with the MULTIMODE method are shown with thick lines.

Similar with survey spectrum calculation, the internal torsion motion of CH$_3$CHOO is treated with semi-rigid approach since the ground state wave functions are localized. Since the energies of highly excited states of torsion mode exceed the torsion barrier height, 730 and 427 cm^{-1} for *syn-* and *anti-*CH$_3$CHOO, respectively, the excitation of torsion mode is restricted to 2 in order to avoid any unreasonable couplings with torsion mode. The semi-rigid treatment for *anti-*CH$_3$CHOO is more problematic, especially for "hot bands", than for *syn-*CH$_3$CHOO because the barrier to internal rotation for the *anti-*conformer is roughly 300 cm^{-1} lower than for the *syn-*conformer.

Thirteen harmonic oscillator basis are used for each mode in the first VSCF calculation. In the current study, all 18 vibration modes of CH$_3$CHOO are included, and up to 4 modes can be excited simultaneously. As mentioned above, the maximum excitation of torsion mode is 2. To reduce the expense of calculation, the total excitation of four CH-stretching modes of CH$_3$CHOO is limited to 3. Since the frequencies of CH-stretching modes are far beyond the spectral range investigated, 830-1,550 cm^{-1}, such restrictions on CH stretch modes affect little accuracy of the calculation. The maximum excitations of all other modes are 7. Cs symmetry is applied in the MULTIMODE calculation. The sizes of VCI matrix for the two Cs blocks are 22,157 and 17,924. The values predicted with the MULTIMODE method including all 18 modes are depicted with thick lines in Figure 8.5f,g. The vibrational energies are also calculated using various lower-level methods, and the predicted energy range is shown in Figure 8.5f,g as well.

The MM program has been adapted to calculate the coupling for an arbitrary number of pre-specified normal modes between 1 and $3N - 6$ to be considered. In addition, we performed another smaller set of calculations which only includes 13 modes of syn- and 14 modes of anti-conformer to compare with the calculations that includes all 18 modes. For syn-conformer, the frequencies of nine vibration modes are in the measured spectral

range from 830 to 1550 cm^{-1}, and ten such modes for *anti*-conformer. The smaller set calculation of 13 modes for *syn*-CH$_3$CHOO includes such nine modes and four CH stretch modes, and similarly for calculation of the 14 modes for *anti*-CH$_3$CHOO.

As shown in Figure 8.5f, the more stable *syn*-CH$_3$CHOO conformer is predicted from the MULTIMODE calculations to have more intense absorptions near 908 (100), 969 (5), 1,097 (6), 1,285 (19) and 1,494 (8) cm^{-1}; the numbers in parentheses give relative infrared intensity of each vibration. The observed new features near 871 (100), 956, 1,091 (10), 1,281 (40) and 1,477 (30) cm^{-1} agree satisfactorily with these predicted values. The predicted pattern of intense lines of *anti*-CH$_3$CHOO near 894 (49), 944 (100), 1,295 (3) and 1,488 (10) cm^{-1} agrees less satisfactorily with the observed spectrum. We show below that the contribution from the *anti*-CH$_3$CHOO conformer, although less significant, is important for explaining the overall shape of the spectrum and is of primary importance for explaining some of the fine-structure spectral features of the spectrum.

Rotation constants of the ground vibrational state and fundamental vibrational states are determined rigorously from calculated energy difference of $J = 1$ and 0. The rotation constants of *syn*-CH$_3$CHOO ground vibrational state agree with those determined experimentally[87]. The computed rotation constants for *syn*- and *anti*-CH$_3$CHOO are shown in Tables 8.4, respectively. These small energy differences are sensitive to the treatment of the torsion degree of freedom, and so several sets of calculations, including ones that eliminated that degree of freedom, were performed. The rotation constants that appear to be most consistent with the simulation of experimental bands are from the smaller set of calculation with 13 modes coupling for *syn*-CH$_3$CHOO (14 modes for anti) and these are given in the table.

Table 8.4: Comparison of rotational parameters of CH$_3$CHOO in their ground and vibrationally excited states predicted with MULTIMODE calculation coupling 13 modes of *syn* and 14 modes of *anti*

	syn			*anti*		
	A'/A"	B'/B"	C'/C"	A'/A"	B'/B"	C'/C"
ν_4	0.9973	0.9981	0.9980	0.9966	1.0000	0.9993
ν_7	0.9982	0.9981	0.9980	0.9978	1.0000	1.0000
ν_8	1.0011	1.0006	0.9980	1.0051	0.9997	0.9982
ν_9	0.9966	0.9992	0.9989	0.9950	0.9990	0.9982
ν_{10}	0.9904	0.9990	0.9946	1.0049	0.9997	0.9982
	A"	B"	C"	A"	B"	C"
$\nu = 0$	0.5810	0.2388	0.1748	1.5998	0.1482	0.1392
Exp[a]	0.5866	0.2379	0.1744	1.6176	0.1479	0.1390

[a] Ref. 87

The hot-band transition can be calculated from the MULTIMODE calculation as well. We present two sets of calculation results in Table 8.5. One is from the calculation with all 18 modes coupling; another is from the smaller set of calculation with selected 13 modes for *syn*-conformer (14 modes for *anti*) as well as another two lowest frequency modes. As seen, relatively large deviation of the hot-band transition shift is observed between the experimental measurement and MULTIMODE prediction. One main reason is the treatment of the torsional mode of CH$_3$CHOO. As mentioned above, the maximum excitation of torsion mode is restricted to 2. Such restriction affects the calculated energies of torsion states and other modes with small energies. In addition, including the low-frequency modes enhances the coupling among states. For the ground state, the torsion

splitting is small and such restriction has negligible effect to calculation. However, as the torsion mode is excited to the fundamental or overtone states, our "single-reference" treatment of torsion motion may be problematic. Nevertheless, the blue-shifted hot-band transition of these bands agrees with experimental simulation.

Table 8.5:   Comparison of fitted wavenumbers (cm1) and relative intensities of various vibrational modes of syn-CH$_3$CHOO and anti-CH$_3$CHOO predicted with MULTIMODE prediction.

Transition	Inten.	Eng.	Exp	Caln 1[a]	Caln2[b]	Transition	Inten.	Eng.	Exp	Caln 1[ac]
Band A_1						Band A_3				
syn						*syn*				
10^1	1.00		871.2	911.9	908.1	7^1	1.00		1280.8	1287.0
$10^1 18^1$	0.42	198	+2.4	+5.0	+13.6	$7^1 18^1$	0.42	198	+3.7	+7.8
$10^1 18^2$	0.18	391	+6.3	+12.0	+29.4	$7^1 18^2$	0.18	391	+8.2	+17.2
$10^1 18^3$	0.07	597	+11.8			$7^1 18^3$	0.07	597	+12.7	
$10^1 12^1$	0.29	282	+10.1	+12.0	+28.3	$7^1 12^1$	0.29	282	+2.2	
$10^1 12^2$	0.15	433	+15.8	+11.1	+80.8	$7^1 12^2$	0.15	433	+5.7	
anti						*anti*				
9^1	1.00		883.7	954.6	944.2	7^1	1.00		1279.4	1299.8
$9^1 18^1$	0.50	158	+1.8	+18.1	+21.7	$7^1 18^1$	0.50	158	+2.6	+17.2
$9^1 18^2$	0.25	316	+5.3	+27.7	+45.1	$7^1 18^2$	0.25	316	+5.6	+22.0
$9^1 17^1$	0.35	239	+2.3	+8.6	+20.4	Band A_4				
$9^1 17^2$	0.15	433	+6.3			*syn*				
anti						4^1	1.00		1476.8	1495.9
10^1	1.00		851.8	902.7	894.2	$4^1 18^1$	0.42	198	+2.2	+6.8
$10^1 18^1$	0.50	158	+9.2	+16.9	+22.8	$4^1 18^2$	0.18	391	+4.2	+12.6
$10^1 18^2$	0.25	316	+15.2	+27.6	+47.1	$4^1 18^3$	0.07	597	+6.2	
$10^1 17^1$	0.35	239	+11.2	+8.7	+25.3	$4^1 12^1$	0.29	282	+0.2	
$10^1 17^2$	0.15	433	+20.2		+61.7	$4^1 12^2$	0.15	433	+2.7	
						anti				
						4^1	1.00		1479.0	1498.2
						$4^1 18^1$	0.50	158	+1.0	+14.1
						$4^1 18^2$	0.25	316	+2.0	

[a] MULTIMODE calculations coupling 15 modes of *syn* and 16 modes of *anti*-CH$_3$CHOO, which includes 13 modes of *syn* (14 modes of *anti*) as discussed in the text and another two lowest frequency modes. The maximal excitations of two lowest frequency modes are limited to 2.

[b] MULTIMODE calculations coupling all 18 modes.

[b] Hot band results are problematic. See text for discussion.

The rotational contour of the A_1 band near 871 cm^{-1} recorded in the interval of

0-2 μs has several characteristic peaks; it cannot be simulated with a single band and was deconvoluted with guidance from calculations. The experimental data are presented with open circles and the resultant spectrum, simulated according to ratios of rotational constants of the excited and ground states predicted with the MULTIMODE method and the experimental rotational constants of the ground state, is shown as a thick solid line in Figure 8.6a; the agreement is satisfactory. Figure 8.6b presents a comparison of experimental data with the spectrum simulated according to slightly modified ratios of rotational constants for an improved fit. This simulated feature consists of three bands: a dominant OO-stretching (ν_{10}) band of syn-CH$_3$CHOO at 871.2 cm^{-1} and two smaller bands of OO-stretching (ν_9) and OO-stretching mixed with CH$_2$ wagging (ν_{10}) modes of $anti$-CH$_3$CHOO at 883.7 and 851.8 cm^{-1}, respectively, shown as thin lines in Figure 8.6a,b. It is found that several hot bands associated with the ν_{18} (208 cm^{-1}) and ν_{12} (314 cm^{-1}) low-energy vibrational modes of syn-CH$_3$CHOO and with the ν_{18} (156 cm^{-1}) and ν_{17} (255 cm^{-1}) low-energy vibrational modes of $anti$-CH$_3$CHOO contribute significantly to the observed spectral features. The individual contributions of fundamental and hot bands for these three vibrational modes are shown in Figure 8.6c-e; the transitions of hot bands are expressed as ν_i^f in which ν is the vibrational mode number, and i and f are vibrational quantum numbers of the lower and upper states, respectively.
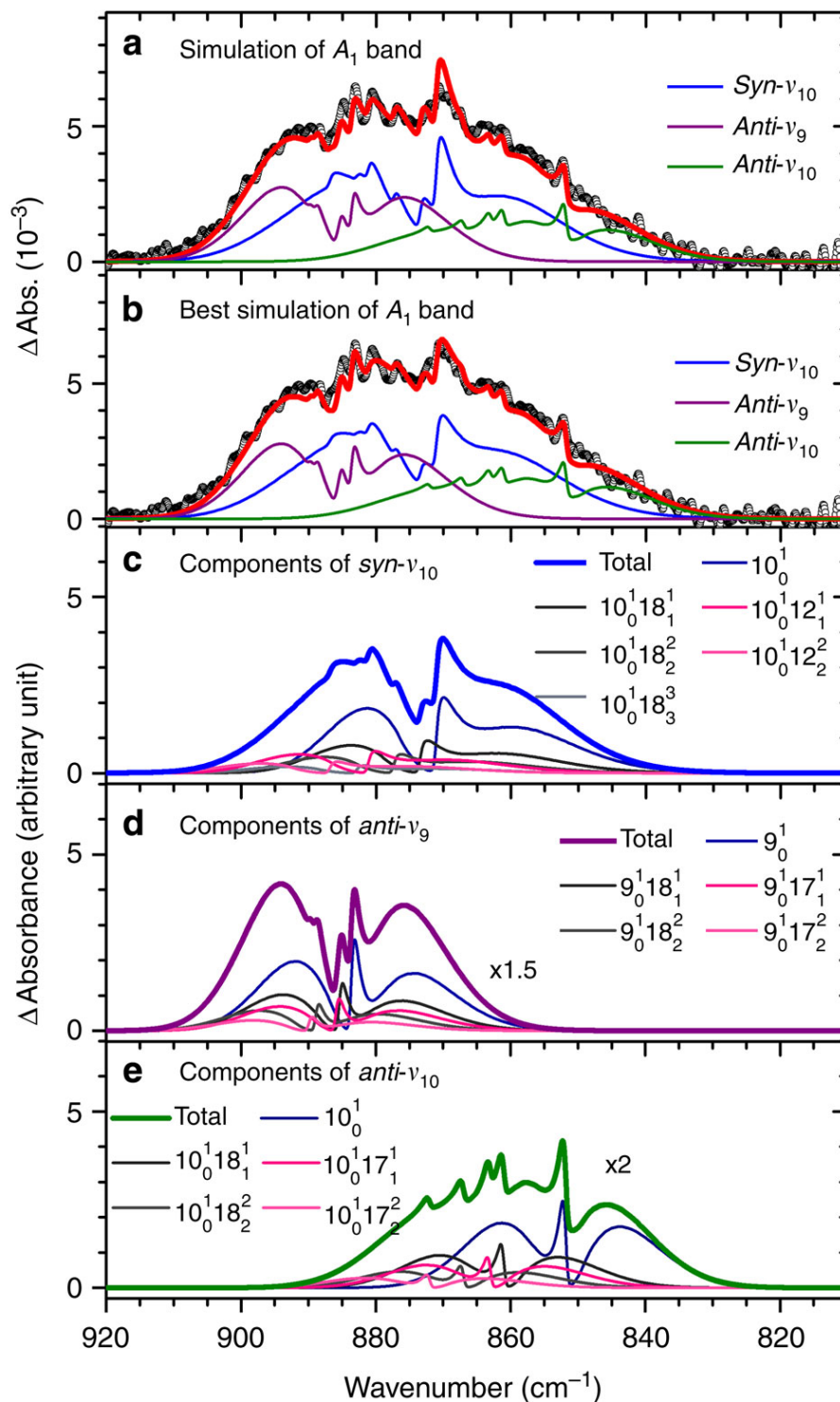
Figure 8.6: Spectral simulation of band A_1. (a) Comparison of experimental data (open circles, recorded $0-2$ μs) with spectrum simulated according to theoretical predictions (thick red solid line) and (b) the best simulated spectrum (thick red solid line) with slightly modified parameters; contributions of ν_{10} of syn-CH₃CHOO, and ν_9 and ν_{10} of anti-CH₃CHOO are shown with thin lines. Resolution is 0.5 cm^{-1}. (c) Contributions of fundamental and hot bands of ν_{10} of *syn*-CH₃CHOO, (d) ν_9 of *anti*-CH₃CHOO and (e) ν_{10} of *anti*-CH₃CHOO.

Detailed positions and relative intensities are listed in Table 8.5. This simulation implies that (1) the hot bands are all blue shifted from the fundamental; the unusual but necessary blue shifts of about 2 and 10 cm^{-1} for the hot bands involving ν_{18} and ν_{12} of *syn*-CH$_3$CHOO, respectively, agree qualitatively with the theoretical predictions (Table 8.5). The calculations also indicate that torsional splitting is small for all vibrational modes so that it has no consequence on our spectral simulation. (2) At 328 K, assuming a Boltzmann distribution and that the infrared intensities of hot bands are the same as that of the fundamental band (in qualitative accord with calculations), observed relative intensities of these hot bands imply energies of the first excited states of ν_{18} and ν_{12} modes of *syn*-CH$_3$CHOO and those of ν_{18} and ν_{17} of *anti*-CH$_3$CHOO to be $\sim$ 193, 282, 149 and 239 cm^{-1}, respectively, which is consistent with theoretical predictions (Table 8.6). (3) The population fraction of *anti*-CH$_3$CHOO is 0.30 and 0.38 at 328 K, respectively, if infrared intensities predicted with the B3LYP and MULTIMODE methods are used. This fraction is consistent with a value of $\sim$ 0.30 derived from ultraviolet experiments[161], but greater than values $\sim$ 0.20 from microwave experiments[87] and $\sim$ 0.10 from photoionization experiments.

The weaker bands A_3 and A_4 can be simulated likewise with contributions of *syn*- and *anti*-CH$_3$CHOO, as presented in Figure 8.7. Band A_3 has a prominent Q-branch at 1280.8 cm^{-1}, which is assigned to the HCO bending coupled with the CO-stretching (ν_7) mode of *syn*-CH$_3$CHOO. A second feature with a weaker Q-branch at 1279.4 cm^{-1} is assigned to the corresponding ν_7 mode of *anti*-CH$_3$CHOO (Figure 8.7a). Band A_4 has prominent P- and R-branches; this band is assigned to the CO-stretching mode coupled with the HCO bending (ν_4) mode of *syn*-CH$_3$CHOO. The observed weak Q-branch arises from a small contribution of the ν_4 mode of anti-CH$_3$CHOO. As band A_2 is rather weak and subject to interference from absorption of C$_2$H$_4$, we could only estimate its position to be $\sim$ 956

cm^{-1} from the Q-branch and assign it to the ν_9 mode of *syn*-CH$_3$CHOO. Band A_5 suffers from partial interference due to the precursor, but the prominent Q-branch indicates that this band is due to *syn*-CH$_3$CHOO and not *anti*-CH$_3$CHOO. The observed position at 1090.6 cm^{-1} is much closer to the predicted anharmonic vibrational wavenumber of 1097 cm^{-1} for *syn*-CH$_3$CHOO than the value 1136 cm^{-1} for *anti*-CH$_3$CHOO.
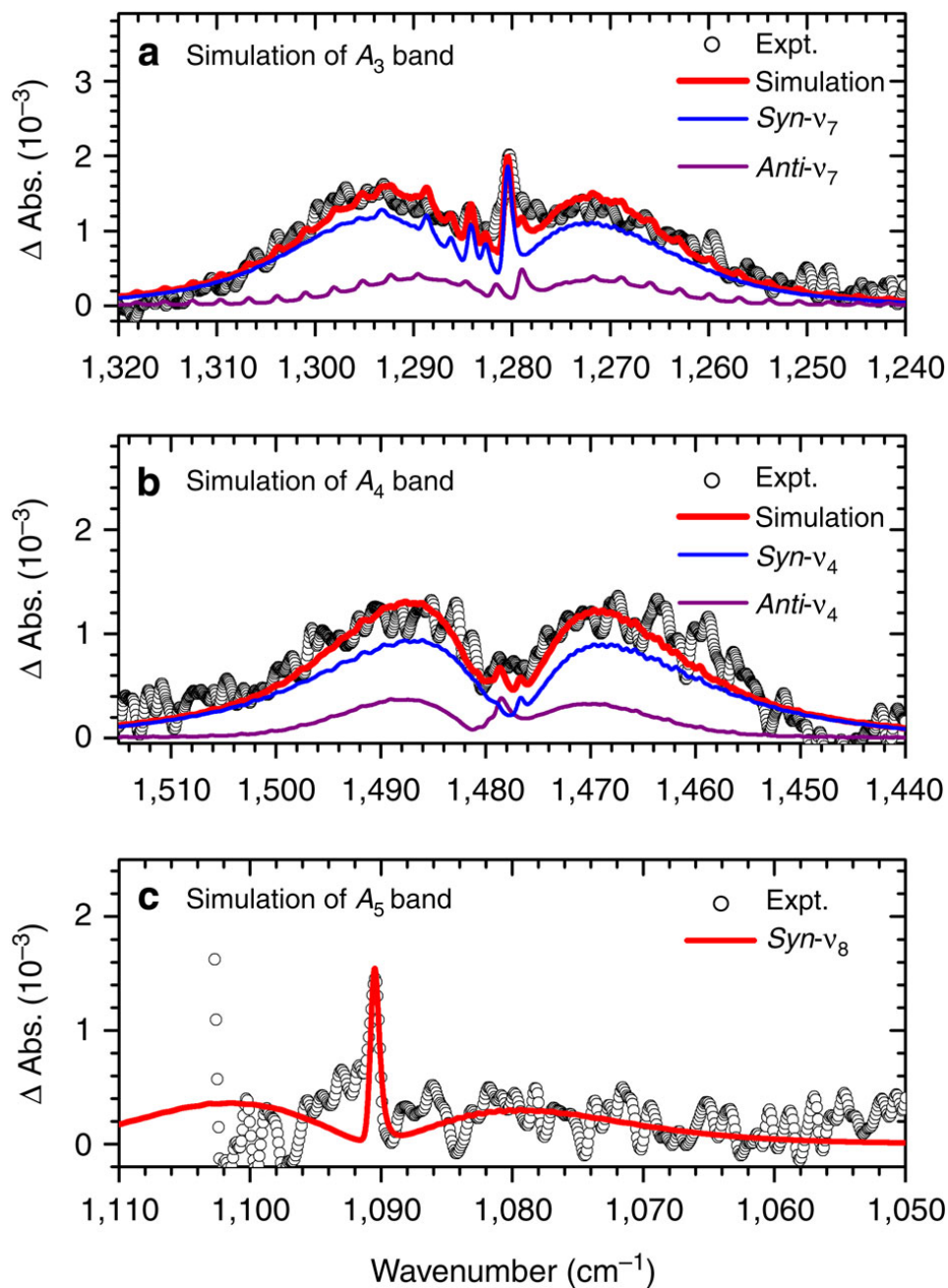
Figure 8.7: Spectral simulation of band A_3 to A_5. (a) Comparison of experimental data (open circles, recorded 0-4 μs) with simulated spectrum (thick red solid line) for band A_3; contributions of ν_7 bands of *syn*-CH$_3$CHOO and *anti*-CH$_3$CHOO are shown with thin lines. (b) Comparison for band A_4; contributions of ν_4 bands of syn-CH$_3$CHOO and anti-CH$_3$CHOO are shown with thin lines. (c) Comparison of band A_5 (recorded 0-2 μs); only the ν_8 band of *syn*-CH$_3$CHOO contributes. Spectral width of simulation is 0.64 cm^{-1}.

As shown in Table 8.6, the agreement between observed vibrational wavenumbers of *syn*- and *anti*-CH$_3$CHOO, and those calculated with the MULTIMODE method is quite satisfactory with differences < 17 cm^{-1}, except for the OO-stretching mode, which has differences of 37 cm^{-1} for *syn*-CH$_3$CHOO and 60 cm^{-1} for *anti*-CH$_3$CHOO. A similar shift between the experiment and MULTIMODE calculations was reported previously for CH$_2$OO for an analogous band[160]. Conceivably, the origin of the deviation is, as in CH$_2$OO, a slight deficiency in the level of electronic structure theory which is more sensitive to the OO-stretching mode.

Table 8.6: Comparison of experimentally observed wavenumbers (cm^{-1}) and intensities with the vibrational wavenumbers and infrared intensities of representative vibrational modes of CH$_3$CHOO predicted with the MULTIMODE method

Sym.	*syn*-CH$_3$CHOO			*anti*-CH$_3$CHOO			Description[a]
	Mode	Exp.	MM	Mode	Exp.	MM	
A'	ν_4	1476.8 (30)	1494 (8)[b]	ν_4	1479.0 (14)	1488 (10)	CO str./HCO bend
A'	ν_7	1280.8 (40)	1285 (19)	ν_7	1279.4 (17)	1295 (3)	HCO bend/CO str.
A'	ν_8	1096.6 (10)	1097 (6)	ν_8		1136 (1)	CH$_2$ wag/CCH bend
A'	ν_9	956.0 (-)	969 (5)	ν_{10}	851.8 (73)	894 (49)	CCH bend/CH$_2$ wag
A'	ν_{10}	871.2 (100)	908 (100)	ν_9	883.7 (100)	944 (100)	OO str.
A'	ν_{12}		314 (3)[c]	ν_{12}		330 (7)	CCO/COO *iph* bend
A"	ν_{17}		449 (0)	ν_{17}		255 (0)[c]	*op* deformation
A"	ν_{18}		208 (1)[c]	ν_{18}		156 (0)[c]	CH$_3$ torsion

[a] Approximate mode description. For anti-CH$_3$CHOO, the HCO bending mode is replaced with CH *ip* bending mode for ν_7, ν_8 is mainly CCH bend, the CCH bend is replaced with OO stretch for ν_{10}, and the iph bend is replaced with *oph* bend for ν_{12}.

[b] Relative infrared intensities normalized to the most intense line.

[c] Harmonic vibrational wavenumbers, as the anharmonic treatment of this mode is problematic using the methods employed here.

Our observations also conform to an expectation that similar to CH$_2$OO, CH$_3$CHOO has a significant zwitterionic character with a strengthened C-O bond and a weakened O-O bond. The observed wavenumber of the OO-stretching mode of *syn*-CH$_3$CHOO near 871 cm^{-1} is smaller than the corresponding value 908 cm^{-1} of CH$_2$OO, consistent with theoretical predictions showing that the length of the O-O bond increases.

8.6 Summary

In summary, we first presented survey IR spectra of the *syn*- and *anti*-conformers of the alkylsubstituted Criegee intermediate (CH$_3$CHOO) up to 6200 cm^{-1}. These are based on accurate full-dimensional potential energy surfaces and dipole moment surfaces and anharmonic coupled vibrational calculations. In addition, the ground state wavefunctions and zero-point energies for the two conformers were determined with Diffusion Monte Carlo calculations.

Collaborating with experimental study, we reported spectrum of *syn*- and *anti*-CH$_3$CHOO in the middle infrared range of 830 - 1550 cm^{-1}. The fundamental energies, hot band transitions, and the rotation constants for the vibrational ground and excited state for both conformers were calculated using the MULTIMODE program. The calculation results successfully support and guide the simulation of observed bands in the experiment.

Chapter 9

Pruning the Hamiltonian Matrix in MULTIMODE

9.1 Introduction

Nitromethane (CH_3NO_2) consists of a heavy nitro (NO_2) group and a relatively light methyl (CH_3) group. The molecule has a very low 6-fold internal rotation barrier, and the CH_3 group is almost a free rotor in the ground vibrational state, which makes it an interesting system. The microwave and infrared (IR) spectra of nitromethane have been thoughly studied experimentally.[162–173] The vibrational spectrum of nitromethane has been investigated in the theoretical studies as well. In the early study, the geometries and vibration frequencies of nitromethane and its isotopomers were investigated using low-level *ab initio* calculation.[174,175] Later, the effect of internal dynamics on the CH stretch overtone states was analyzed using a theoretical model, which considered the coupling between the CH overtone and the methyl internal motion and the isoenergetic states.[169].

The calculation of rigorous quantum vibration is a challenging task for polyatomic molecules, and especially for molecules as large as nitromethane. The present article reports an accurate approach to address the vibration energies and large-amplitude vibrational dynamics using the MULTIMODE (MM) code and diffusion Monte Carlo method, using a full-dimensional potential energy surface (PES).[12] In the usual methyl-rotor system, the torsion motion usually has 3-fold barrier with a barrier height of several hundred wavenumber. The methyl torsion has been treated both as a localized mode[12] and as large amplitude motion[30] in the previous MM calculation, depending on the system. However, the situation of nitromethane with 6-fold extremely low barrier is quite different from many cases where the torsional barrier is several hundred to roughly 1000 wavenumbers.

Previous experimental measurement of CH stretch overtones investigated the change in the torsional barrier height upon the vibrational excitation higher than the third overtone.[169] However, for the energies of fundamental states we are interested in, the effect of torsion motion is negligible. Therefore, we excluded the torsion mode and do not consider its coupling with other modes in the vibration analysis. Note that the rigorous treatment of torsion as large amplitude motion is also available in the reaction path version of MULTIMODE, as has been applied in methanol and $H_5O_2^+$.[176,177]

Nevertheless, 14-mode calculations are still challenging and can lead to very large Hamiltonian matrices. To address this issue, we apply a pruning scheme, suggested previously by Handy and Carter, that reduces size of the matrix without sacrificing accuracy in the eigenvalues. The method is briefly described here in the context of partitioning theory. A new and more efficient implementation of it, coded in the latest version of the MULTIMODE program, is described. The accuracy and efficiency are demonstrated for 12-mode C_2H_4 and then applied to CH_3NO_2. Agreement of the fourteen fundamental energies of CH_3NO_2 with available experimental values is very good.

9.2   Potential Energy Surface

The potential energy surface is a linear least-squares fit to *ab initio* calculations using the MOLPRO 2010 package.[58] The electronic energies were calculated using the explicitly correlated coupled-cluster single and double excitation method that includes a perturbation treatment of triple excitations (CCSD(T)-F12b),[54,55] with the cc-pVDZ basis for the light H atoms and aug-cc-pVDZ basis for other heavy atoms (HaDZ).

Following the procedure of constructing the PES, 17 079 points were sampled totally. Then the energies were calculated using the CCSD(T)-F12b method, and were used in the PES fitting. The maximum fitting polynomial order is 5, which generates 7946 coefficients. The total fitting root mean square (RMS) error is only 0.37 cm^{-1}, which is very small, indicating a precise fit. The number of configurations and the fitting RMS in different energy ranges are shown in Figure 9.1. As seen, most of the energies sampled are below 20 kcal/mol, but with more geometries efficiently sampled at energies up to around 40 kcal/mol.
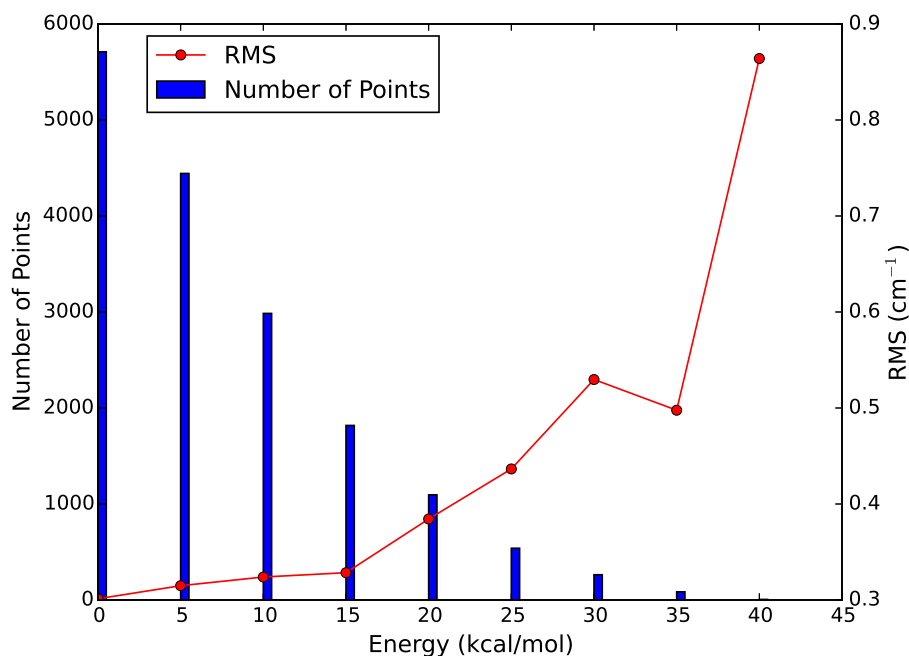
Figure 9.1: Root-mean-square (RMS) error and number of points of the PES fitting in different energy ranges with respect to CH_3NO_2 minimum.

The geometries of minimum and torsion saddle point (SP) were optimized using the PES and normal mode frequencies were obtained at these stationary points. These are given and compared with results from direct CCSD(T)-F12b calculations in Table 9.1. The barrier height of torsion motion from the PES is 3.5 cm^{-1}, which is slightly larger than the earlier report of 2.1 cm^{-1}.[164] Due to such a small barrier height, it is difficult to accurately describe the harmonic normal mode torsion mode and so we are not surprised to find a relatively large discrepancy of the harmonic torsion frequency. For this mode, the harmonic approximation is not a good zero-order one.

Table 9.1: The comparison of electronic energies (cm^{-1}) and harmonic frequencies (cm^{-1}) of CH_3NO_2 between PES and CCSD(T)-F12b calculations.

			Minimum		SP	
			PES	*ab initio*	PES	*ab initio*
Eng.			0.0	0.0	3.52	3.77
mode	sym.	description				
ω_1	A′	C-H str.	3184.5	3184.5	3184.2	3183.8
ω_2	A′	sym. C-H str.	3084.5	3084.8	3084.8	3085.5
ω_3	A′	CH_3 deform.	1487.1	1488.7	1487.9	1487.0
ω_4	A′	NO_2 sym. str.	1437.5	1437.0	1437.7	1437.6
ω_5	A′	CH_3 sym. deform.	1417.1	1417.2	1417.2	1417.3
ω_6	A′	CH_3 rock	1143.7	1142.4	1144.5	1142.9
ω_7	A′	C-N str.	942.7	942.2	942.4	942.0
ω_8	A′	NO_2 sci.	673.3	672.8	670.5	669.6
ω_9	A′	NO_2 wag	608.0	607.6	612.0	611.4
ω_{10}	A″	C-H asym. str.	3212.5	3212.8	3211.7	3211.7
ω_{11}	A″	NO_2 asym. str.	1630.9	1630.3	1631.1	1630.4
ω_{12}	A″	CH_3 deform.	1476.5	1477.3	1475.9	1475.4
ω_{13}	A″	CH_3 rock	1119.0	1119.0	1118.4	1118.1
ω_{14}	A″	NO_2 rock	481.4	481.9	478.8	477.5
ω_{15}	A″	methyl torsion	26.3	66.2	20.9i	57.3i

In order to examine the torsion of methyl group, we use the equilibrium structure and select an H^1 in the CH_3 group and defined the internal rotation coordinate τ as

the dihedral angle between the CNH^1 plane and the CNO_2 plane (these four atoms are co-planar in the equilibrium structure), as indicated in Figure 9.2a. Using this definition, the fully relaxed torsion path was located using the fitting PES. At each step, the torsion angle was fixed, and the energy was optimized with respect to the other 14 degrees of freedom. The relaxed path is depicted in Figure 9.2b, where the six-fold barrier is clearly seen.
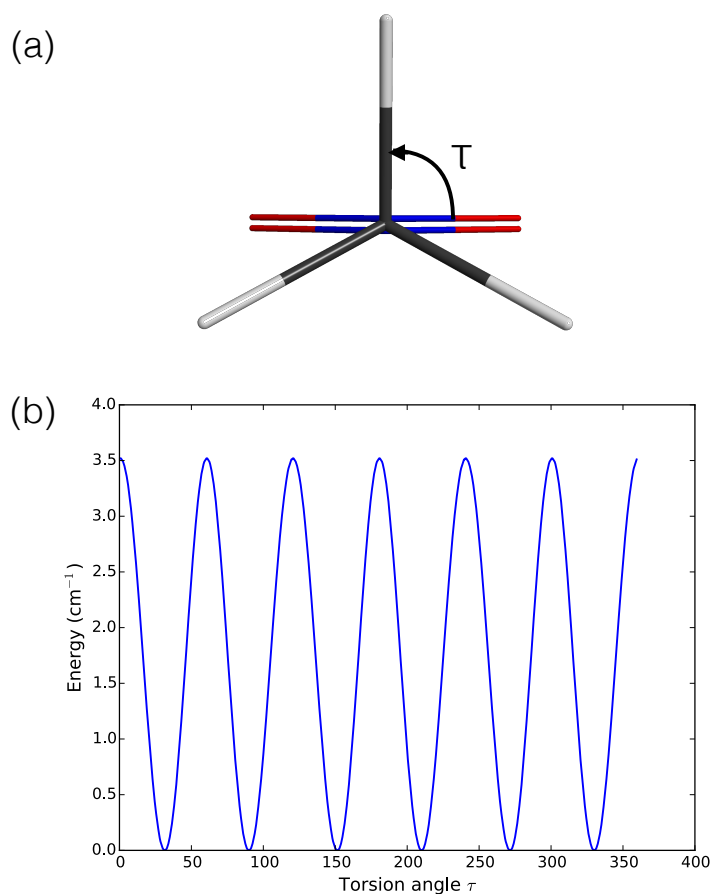
Figure 9.2:   The definition of torsion angle τ is given in panel (a). The fully relaxed path of CH_3NO_2 along the methyl torsion angel is shown in panel (b).

9.3   Diffusion Monte Carlo

The zero-point energy (ZPE) and the wavefunction of the ground vibrational state of nitromethane were determined using the standard Diffusion Monte Carlo (DMC) approach.[26,27] Each DMC trajectory was propagated for 15 000 steps using 15 000 walkers and the time step was equal to 5.0 a.u. In each simulation, the first 5000 steps were used for the system equilibration, and the following 10 000 steps were accumulated to calculate the ZPE. Eight trajectories were performed and the final ZPE of nitromethane was determined to be $10\ 814 \pm 3.63$ cm^{-1}. The distribution of walkers can be used to visualize the wavefunction. The minimum reference geometry and all walkers were mapped to the principle axis frame, then the amplitude of wavefunction can be expressed by the density of walkers and plotted as an isosurface. This is shown in Figure 9.3 from two perspectives. The visualization clearly shows that the methyl group is nearly free rotor in the ground state.
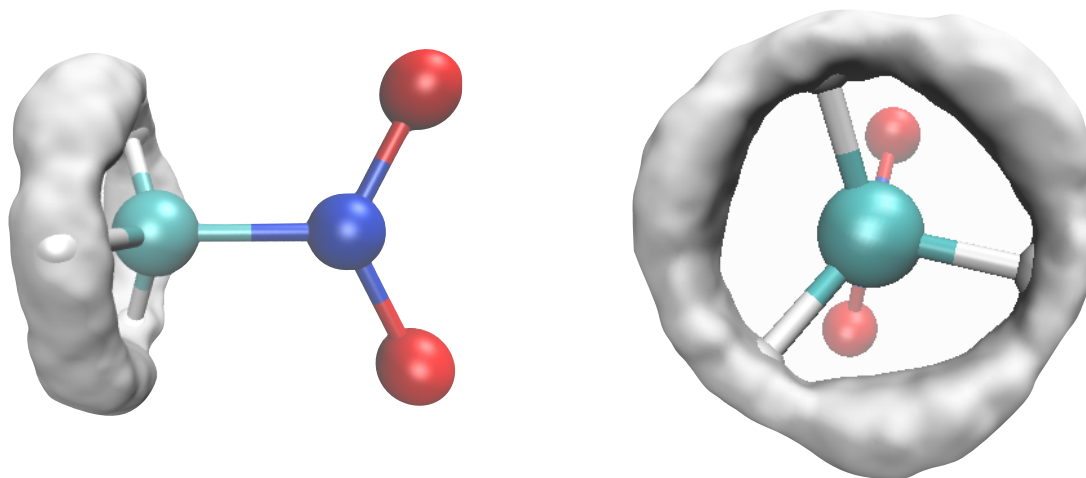
Figure 9.3:   Isosurfaces of ground vibrational state wavefunction for nitromethane from Diffusion Monte Carlo calculations.

9.4   MULTIMODE calculations

The focus of the current study is the vibrational analysis of nitromethane and the comparison with available experimental energies, where the MULTMIMODE program is applied. Details of MULTIMODE have been described in Chapter 2, and so here we focus on a method to prune the Hamiltonian matrix and a new efficient implementation of it. In the

current study, we used both 4MR and 5MR for the potential representation, which give convergence to a few wavenumbers or less.

One of the biggest bottlenecks in variational calculations using basis functions is the construction and diagonalization of the Hamiltonian matrix. As the size of the molecule and thus the number of vibrational modes increases, it is unavoidable that the large VCI matrices will be encountered. There are a variety of schemes for selecting the excitation space using a direct-product basis, such as we use here. The one used in MM has been described in detail[29] and will be explained briefly using more conventional terminology from electronic structure theory. In MULTIMODE an n-mode basis[29] refers to an excitation space. So for example, a 1-and 2-mode basis refers to an excitation space of "singles" and "doubles", respectively, using more conventional terminology.

9.4.1   H-matrix pruning

For moderate-sized Hamiltonian matrices, i.e., those of the order of 10^4, standard full diagonalization routines can be applied efficiently. However, for matrices that approach order 10^5 and for which, as usual, only a small fraction of eigenstates are desired, iterative methods become attractive. MULTIMODE uses an efficient Davidson diagonalization procedure, described previously[29]. However, even this procedure can become prohibitive for very large matrices, where only a percent or so of the eigenvalues and eigenvectors are needed. Handy and Carter proposed a procedure to significantly reduce the matrix size, using a perturbation theory test to evaluate the coupling between the diagonalized singles and doubles Hamiltonian and higher exctations in order to eliminate rows and columns.[37] This procedure was demonstrated for CH_3OH using a realistic PES. In this demonstration, a matrix of order 128 000 is "pruned" to a matrix of order 27 000 with

virtually no loss in accuracy for the first 300 eigenvalues. The procedure can be viewed as a powerful approach to manage the exponential growth of the H-matrix.

We briefly re-capitulate the Handy-Carter proposal using standard matrix partitioning theory and also using the nomenclature of singles, doubles, etc. excitations, noted above. To begin, we note that partitioning a matrix into diagonal and off-diagonal blocks of sub-matrices is well established in the field. The procedure for organizing a matrix in this fashion is of course not unique. Typically, it is done based on a particular strategy that aims in general to put as much of the relevant physics into the first diagonal block of the partitioned matrix. In vibrational analysis, one can trace this idea back to the late 1980s and 90s,[178,179] where the applications were restricted to triatomic molecules.

The Handy-Carter pruning procedure can be cast into a partitioning scheme for a full H-matrix, partitioned into a- and b-spaces, as shown in the following equations:

$$
\begin{bmatrix} H_{aa} & H_{ab} \\ H_{ba} & H_{bb} \end{bmatrix} = \begin{bmatrix} H_{aa} & 0 \\ 0 & H_{bb} \end{bmatrix} + \begin{bmatrix} 0 & H_{ab} \\ H_{ba} & 0 \end{bmatrix}
$$

$$
H^{(0)} = \begin{bmatrix} H_{aa} & 0 \\ 0 & H_{bb} \end{bmatrix} \rightarrow \begin{bmatrix} C_a^t H_{aa} C_a & 0 \\ 0 & C_b^t H_{bb} C_b \end{bmatrix} = \begin{bmatrix} E^{(a)}(\text{easy}) & 0 \\ 0 & E^{(b)}(\text{hard}) \end{bmatrix}
$$

$$
H^{(0)\prime} = \begin{bmatrix} H_{aa} & 0 \\ 0 & H_{bb}^{diag} \end{bmatrix} \rightarrow \begin{bmatrix} C_a^t H_{aa} C_a & 0 \\ 0 & H_{bb}^{diag} \end{bmatrix} = \begin{bmatrix} E^{(a)}(\text{easy}) & 0 \\ 0 & H_{bb}^{diag} \end{bmatrix} \tag{9.1}
$$

where for example a is the space of single and doubles excitations and b is the space of all higher excitations.

As indicated, the full H-matrix is partitioned into blocks. The H_{aa} block is the one obtained from a subset of the excitation space, for example single and double excitations

or even single, double and triple excitations and the H_{bb} block is from all higher exci-
tations. (As noted above, a maximum of sextuple excitations is allowed in the current
version of MM). Of course off-diagonal blocks couple these two spaces. One standard
procedure would be to diagonalize these two blocks separately and then re-couple the
resulting zero-order eigenfunctions either with a final diagonalization or perturbation
theory. Clearly, based on the discussion above H_{aa} is generally much smaller than H_{bb}
and so diagonalization of the latter is not practical. So, the suggestion is to diagonalize
H_{aa} and approximate the H_{bb} eigenvalues and eigenvectors by the diagonal elements of
H_{bb} and the identity matrix, respectively. While this may seem like a drastic approxima-
tion, it nevertheless serves to yield a zero-order set of eigenvalues and eigenfunctions that
can be used to prune the original, full H-matrix. This is done, now following Handy and
Carter, by considering the expression for one term in the usual second-order correction
to the energy (which would be summed over j.)

$$\epsilon_{i(a),j(b)} = \frac{|<\Psi_i^{(a)}|H|\phi_j^{(b)}>|^2}{|E_i^{(a)} - E_j^{(b)}(= H_{j,j}^{(b)})|}, \tag{9.2}$$

where $\psi_i^{(a)}$ is an eigenstate of H_{aa}. Specifically,

$$\psi_i^{(a)} = \sum_j c_{i,j}\phi_j^{(a)}, \tag{9.3}$$

where $\phi_j^{(a)}$ is a virtual-state basis function in the space of single and double excitations
and $c_{i,j}$ is the eigenvector. As noted, diagonalizing H_{aa} is "easy" as the order of this
matrix is modest. The zero-order eigenvalues for the b-block, $E_j^{(b)}$, are just the diagonal
elements of H_{bb} and $\phi_j^{(b)}$ are just the virtual-state basis functions for triple and higher
excitations in the present example.

To continue, it is important to note that the $\psi_i^{(a)}$ are assumed to be good approximations to the exact eigenstates they represent. Then $\epsilon_{i(a),j(b)}$, instead of being one term in the standard expression for the second-order correction to the energy of state $\psi_i^{(a)}$, is used to determine the importance of higher-excitation states. Thus, Handy and Carter defined $\epsilon_{i(a),j(b)}$ as a tolerance, TOL, which was used to determine which rows and columns of the H$_{bb}$ block in H-matrix can be eliminated. The criterion for elimination is that TOL must be less than some threshold for every element in the b block. Thus, for a subset of rows $i(a)$ (see below for details) TOL is calculated for each column $j(b)$.

The practical implementation of this procedure begins with the user deciding in advance how many eigenstates of the full H-matrix are desired. This of course depends on the molecule and states of interest. For example, if one is interested in calculating well converged fundamentals, this may require many eigenstates, including those describing combinations and overtones of low frequency modes, as these may couple to fundamentals, especially high-energy ones. Clearly, the space of single and double excitations spans the fundamental states, as well as pure overtones and combination bands involving two modes. Then the diagonalization of H$_{aa}$ should give well-converged eigenstates. Thus, the order of H$_{aa}$ is typically ten times as large as the number of eigenvalues $E_i^{(a)}$ and eigenfunctions $\Psi_i^{(a)}$ using for the TOL-test.

The pruning process is shown schematically in Figure 9.4. The full matrix of order N is depicted as the upper triangle. As shown, it is composed of three parts, labeled here as A, B, C for simplicity. A corresponds to H$_{aa}$, B to H$_{bb}$ and C to the off-diagonal block H$_{ab}$. In the original Handy-Carter paper, this complete matrix was evaluated and written to disc. In the new approach, we commence by evaluating the half-matrix A, of order N_A, and write it to disc in columns for future use. We diagonalize A with a standard method, e.g., GIVENS is used in MM, and save a specified number of energy

eigenfunctions and eigenvalues $\psi_i^{(a)}$ and $E_i^{(a)}$, respectively. Typically, this would be several hundred functions that span the energy of the eigenstate space of interest, e.g., all of the fundamentals. Next, the rectangular matrix C, of dimension $N_A \times (N - N_A)$, is evaluated and held in core. The diagonal elements $H_{j,j}^{(b)}$ are evaluated and stored. Then the rows of the A-matrix corresponding the set of saved $\psi_i^{(a)}$ and $E_i^{(a)}$ are scanned and the TOL-test is applied to each of N-N_A columns in C. If *any* element of these columns delivers a value of $\epsilon_{i(a),j(b)}$ greater than TOL, this column j is retained. Conversely, if all elements of a column deliver a value of $\epsilon_{i(a),j(b)}$ less than TOL that column is deleted. This procedure is repeated for all $N - N_A$ columns of C. Upon completion, the matrix C is condensed to a new matrix C' of dimension $N_A \times N'_C$, where N'_C is the number of columns of C to be retained. The final step involves evaluating the corresponding elements in B with that block denoted B' (corresponding to C'), Columns of this half-matrix are added to those of C', and the entire column is appended to those of the half-matrix A, previously written to disc. Hence we arrive at the final matrix of order $N_A + N'_C$, indicated by the green shading in Figure 9.4, to be diagonalized without having to evaluate the major part of the half-matrix B. This is noted by the hatched diagonal lines in Figure 9.4. Note, even with this pruning the final matrix may still be quite large and so the iterative Davidson method will often be the method of choice and this is the default in MM.
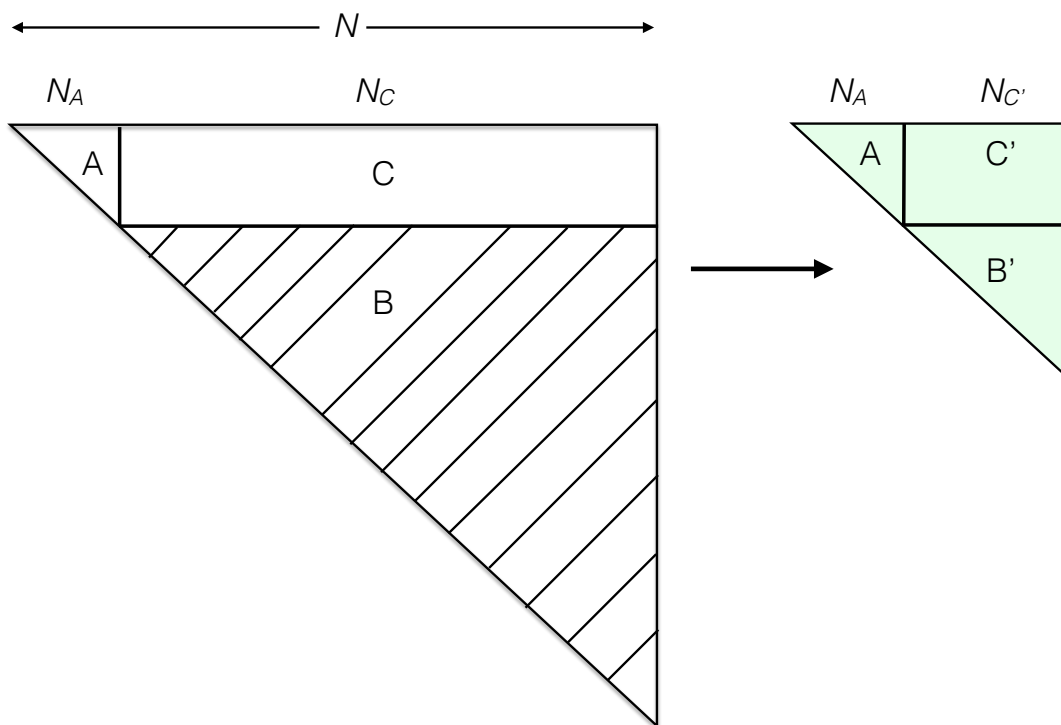
Figure 9.4:   Schematic of the upper triangle of the original H-matrix of order N. Hashed region labeled "B" is not calculated. Pruned matrix is indicated in green shading

Before presenting some tests of this pruning approach, we remark on some expectations of its performance. As already noted, the space of single and double excitations does span the fundamentals, pure overtones and some combinations bands. However, the accuracy of the corresponding eigenstates (of A) is not assured even if A is made sufficiently large to converge them. This is because there exist triple and higher excitation virtual states with energies that are interleaved in the energy spectrum of the singles and doubles space, notably for high-energy fundamentals. Thus, the ultimate accuracy of the

pruning method can be expected to be uneven as the energy increases. Of course, a way to mitigate this is to expand the a-space to include triple excitations. This will lead to a larger A matrix; however, a more accurate final pruning will certainly result. This option is contained in the new version of MULTIMODE and will be illustrated below in the tests of the pruning method for C_2H_4.

9.4.2   Tests for C_2H_4

In order to test the procedure, we have carried out calculations for C_2H_4 which has 12 vibrational normal modes using a PES developed by Avila and Carrington for use in large benchmark calculations by them, which includes full (12) dimensional quadratures of the potential.[180] Subsequently, MULTIMODE calculations, without pruning, were reported for $J=0$ in order to compare directly with the benchmark results[181]. The majority of those calculations were done with a 4-mode representation of the potential and various level of excitations. The full symmetry was used and so the H-matrix was 8-fold block diagonal.

The first test was to generate very large H-matrices by adding 3-mode, 4-mode, 5-mode and 6-mode excitations to the 1- and 2-mode matrix A, and with large values of excitation limits. In this way, we were able to generate matrices of order N equal to 31 958, 222 761, 1 193 789, and 2 932 449. In this test, 3MR was used for the potential for efficiency. Setting the number of saved $\psi_i^{(a)}$ and $E_i^{(a)}$ at 200 and $TOL = 10^{-2}$ cm^{-1}, these matrices were reduced in dimension to 6172, 13 372, 15 798, and 15 798, respectively. The zero-point energy of the final 6-mode matrix was only 1.64 cm^{-1} lower than that of the 3-mode matrix. The fundamentals for the 4-mode, 5-mode and 6-mode matrices differ at most by 3 cm^{-1}. No attempt was made to apply the Davidson method without

the perturbation treatment. The time taken for the diagonalization of the 6-mode matrix of original order 2 932 449 was a mere 1.91 hours on a single core of a workstation.

The second test was to examine the accuracy of low-lying states of C_2H_4 of one symmetry block, using a 4MR of the potential. Based on previous calculations without pruning[181], the expectation is that this representation will give results for several hundred eigenvalues with differences smaller than a wavenumber or so compared with the benchmark ones. The tests with pruning are given in Table 9.2. For the results shown in the fourth and fifth columns, we used a 2-mode basis for A matrix, which in both cases is of order 1942. The final matrix used a 4-mode basis and 6-mode basis respectively. Both calculations gave reasonable vibration energies, however, the 6-mode basis gives better results especially for the overtone and combination states. As seen in Table 9.2, we got quite good agreement with the benchmark for the fundamental and overtone states. However, for combination states involving one overtone and especially the state involving three modes, i.e. $\nu_4 + \nu_8 + \nu_{10}$, we observed large difference of 45 cm^{-1}. The reason is that eigenstates including three modes are not included in the 2-mode A matrix. Therefore, when we did the pruning using A matrix, the final matrix can not accurately describe such states. To further investigate this, we used 3-mode basis for A matrix, and the results are shown in the last column. Even using the 3-mode basis, the A matrix is only of order 6686. A 6-mode basis was used again for the final pruned H-matrix of order 24 051. Comparing the results with the benchmark and previous full MM calculation, we obtained almost identical energies with differences smaller than 2 cm^{-1}. The test also shows that we can choose the n-mode basis for A matrix depending on the states we are interested in, and obtain accurate results with much less computational expense. This illustrates the flexibility of the pruning method.

Table 9.2: C_2H_4 zero-point energy (ZPE) and indicated excitation energies (cm^{-1}) obtained with MULTIMODE (MM). The calculations are tested using 4- and 6-mode basis for TOL=0.01 cm^{-1} and 200 eigenfunctions of H_{aa} with pruning Hamiltonian matrix. The calculated energies are compared with previous benchmark results and previous MM calculations using a much smaller Hamiltonian matrix than used in the benchmark calculations.

State	Ref.[a]	Full[b]	4-mode[c]	6-mode[d]	6-mode[e]
ZPE	11 004.8	11 004.0	11 004.6	11 004.1	11 003.9
ν_3	1341.4	1341.4	1341.6	1341.5	1341.5
ν_2	1623.5	1623.2	1629.9	1623.3	1623.2
ν_1	3019.7	3020.2	3020.9	3020.7	3020.0
$2\nu_{10}$	1655.5	1654.2	1659.3	1654.4	1654.0
$2\nu_8$	1855.7	1854.0	1859.5	1854.6	1853.7
$2\nu_7$	1895.2	1893.6	1899.0	1894.0	1893.2
$2\nu_4$	2049.1	2047.5	2052.7	2048.3	2047.3
$2\nu_6$	2447.7	2446.6	2451.2	2447.4	2446.7
$2\nu_3$	2680.9	2680.5	2685.0	2681.2	2680.7
$2\nu_{12}$	2872.1	2870.5	2876.5	2872.4	2870.6
$2\nu_2$	3238.4	3236.8	3249.9	3238.8	3238.4
$\nu_3 + \nu_2$	2958.0	2957.8	2988.0	2961.5	2957.6
$\nu_4 + \nu_8 + \nu_{10}$	2776.2	2775.8	2844.0	2819.7	2774.8
$2\nu_{10} + \nu_3$	3000.3	2998.8	3033.5	3003.3	2997.8
$2\nu_7 + \nu_3$	3231.0	3230.6	3222.4	3194.5	3229.8

[a] Ref. 180. Matrix order of 697 896 using 2-symmetry blocks

[b] Ref. 181. MM calculation using full Hamiltonian matrix of order 24 058, using 8 symmetry blocks.

[c] 1-2 mode basis for H_{aa} and final 4-mode basis. Final matrix size 14 371

[d] 1-2 mode basis for H_{aa} and final 6-mode basis. Final matrix size 20 756.

[e] 1-2-3 mode basis for H_{aa} and final 6-mode basis. Final matrix size 24 051.

9.4.3   Calculations for CH_3NO_2

The new version of MM which implements the perturbation method described above was applied in the study of nitromethane. Nitromethane has 15 vibration modes, including the methyl torsion mode. As mentioned already, we are interested in the fundamentals, and the coupling of CH_3 torsion mode with other modes is very small. Therefore, the torsion mode was excluded, and all other 14 vibration modes were fully coupled in the MM calculation. A 4MR of the potential was employed for most calculations. In the initial VSCF step, 17 primitive harmonic oscillator basis functions were used for each mode. In the following VCI step, we allowed maximum 4-mode excitations. The maximum sum of quanta in all modes for the 1- and 2-mode excitations was equal to 10, and that for the 3- and 4-mode excitations was equal to 8. The resulting VCI matrix size was equal to 94 690. Note that the convergence of MM calculation results was tested within several wavenumbers with respect to the level of mode coupling, the number of basis functions, and the allowed quanta of mode excitations.

The standard Davidson method was used to diagonalize the large Hamiltonian matrix, and we only calculated the first 1000 eigenstates which covered the fundamental energies of CH_3NO_2. In addition, we also applied the perturbation method to reduce the matrix size, and then the Davidson method was used to diagonalize the pruned matrix. In the perturbation method, the VCI matrix size using a 2-mode basis was order 4236. We obtained and saved the first 300 eigenstates to calculate the perturbation parameters with the states from 3- and 4-mode excitations. The TOL value was tested using 10^{-2} cm^{-1} and 10^{-3} cm^{-1}. The calculations from perturbation method were compared with that using the original matrix, which are treated as benchmark results. An overview of the accuracy of the 300 energies from just the 2-mode basis is shown in the left-hand

panel of Figure 9.5. As seen, the energy differences for these states (ΔE) are fairly large, ranging from roughly 20-120 cm^{-1}, with a few exceptions with smaller differences. This is not surprising for this 14-mode Hamiltonian and indeed similar differences are also seen for C_2H_4. The results from two pruned 4-mode Hamiltonian matrices, of orders 31 989 and 48 606, are also shown in Figure 9.5. As expected, the differences decrease dramatically relative to the 2-mode ones, and the zoomed-in plot in the right-hand panel shows that the differences are less than 3.0 cm^{-1}. Clearly, the calculated energies from the VCI calculation with 2-mode excitation is not accurate enough. However, the calculated states using 2-mode basis can provide a reasonable description of vibration states, with energy differences smaller than 100 cm^{-1}, which allow us to calculate the perturbation parameter with states using higher mode basis. As seen in the right panel of Figure 9.5, after applying the perturbation method, we obtained almost identical results with the benchmark calculation and the differences are smaller than 3 cm^{-1} for TOL $= 10^{-2}$ and less than 1cm^{-1} for TOL $= 10^{-3}$.
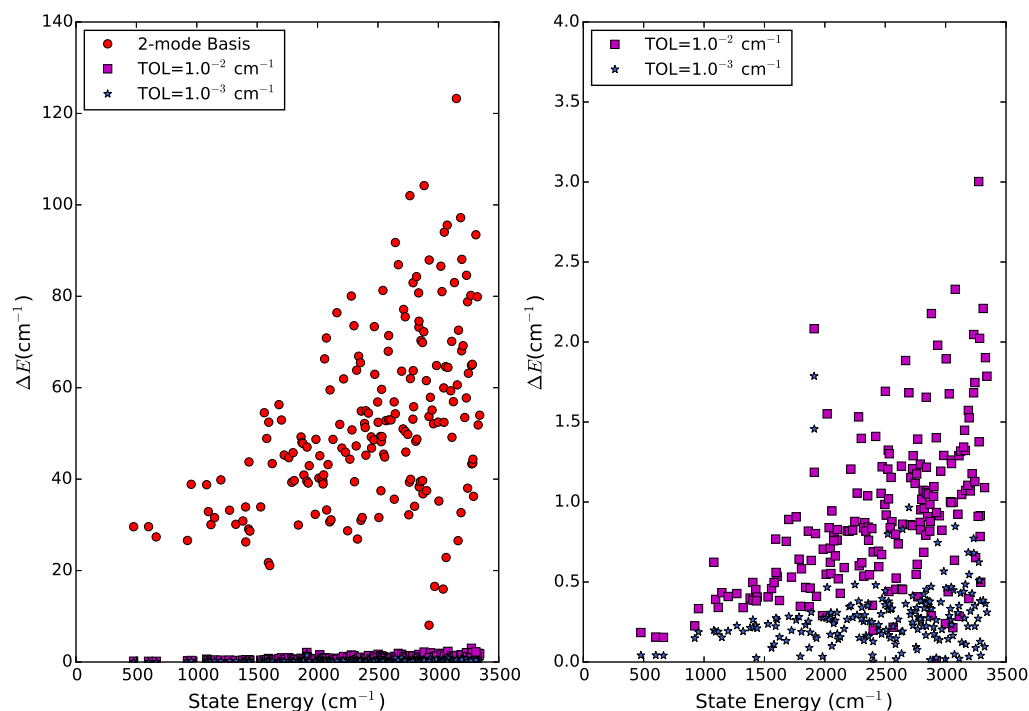
Figure 9.5:   The calculated energy differences ΔE using just the 2-mode basis two final pruned H-matrices obtained using the indicated tolerance values relative to the benchmark results. The benchmarks are obtained from the regular Davidson method without any pruning of matrix. A blow-up of the scale of ΔE is shown in the right-hand figure for the two pruned H-matrices.

The ZPE and fundamentals of nitromethane from the 14-mode MM calculations are given in Table 9.3. The difference of ZPE calculated from DMC and MM is only around 3 cm^{-1}, which indicates that the treatment of excluding the torsion mode in the calculation is reasonable, at least for the ground vibrational state. In addition, the convergence with respect to the n-mode representation was tested by performing 5MR calculation, and we obtained almost identical results with the 4MR calculation except for the strong coupling states. Note that the 5MR calculation was feasible with the pruned matrix and the total

cpu time, indicated in the table, is only 31% greater than the 4MR calculation using the full matrix. As seen, the calculation results using perturbation method are very similar with the regular Davidson method, with differences smaller than 1 cm^{-1} for the states shown. However, because of the much smaller Hamiltonian matrix, the VCI calculation using the perturbation method is about 3-4 times faster than the standard Davidson method, and the memory cost was greatly reduced as well. Due to this advantage, the perturbation method makes it feasible to couple more vibration modes and higher vibration excitations in the VCI calculation, which is very difficult using the regular approach. Comparing the two sets of perturbation calculation using different tolerance values, we can see that as tolerance value decreases, the calculation results show better agreement with the benchmark energies.

Table 9.3: CH_3NO_2 zero-point energy (ZPE) and fundamental energies (cm^{-1}) from MULTIMODE (MM) calculations using the Davidson method for the full matrix and pruned H-matrices for indicated TOL (cm^{-1}) and 200 eigenfunctions of H_{aa} and comparison with experimental result. The VCI computing time using the regular Davidson and perturbation method are also given in the table. The MM calculation using 5MR and pruned matrix (TOL=10^{-2}) is also performed to test the convergence with respect to the n-mode representation of the potential. These calculations are not feasible using the full H-matrix.

State	Full	TOL=10^{-2}	TOL=10^{-3}	5MR[f]	Exp.[a]
ZPE	10 811.5	10 811.6	10 811.5	10 811.9	10 814±3.6[b]
ν_1	*3032.7*	*3033.9*	*3033.0*	*3041.2*	3044
ν_2	2969.6	2970.4	2969.8	2970.2	2973.9
ν_3	1439.6	1440.0	1439.8	1439.9	1438.3
ν_4	1405.5	1405.9	1405.7	1405.6	1397.4
ν_5	1381.2	1381.6	1381.4	1381.8	1378.4
ν_6	1117.5	1117.9	1117.7	1117.9	1119.0
ν_7	923.0	923.2	923.2	922.9	917.6[c]
ν_8	663.8	664.0	663.8	663.6	657.4
ν_9	600.8	601.0	600.8	600.8	602.5
ν_{10}	3064.2	3065.2	3064.7	3066.9	3080
ν_{11}	*1604.3*	*1604.8*	*1604.6*	*1596.2*	1583.8[d]
ν_{12}	1428.9	1429.4	1429.2	1429.3	1428.2
ν_{13}	1095.9	1096.3	1096.1	1096.3	1099
ν_{14}	477.1	477.3	477.2	477.2	475.4[e]
Time(s)	49 294	13 411	18 858	64 946	

[a] Ref. 167; [b] ZPE from diffusion Monte Carlo calculation; [c] Ref. 171; [d] Ref. 172; [e] Ref. 173; [f] MM calculation using 5-mode representation (5MR) of the potential. All other calculations were performed using 4MR.

Comparison with experimental data is also shown in Table 9.3. As seen, there is very good agreement. States ν_1 and ν_{11} (energies shown in italics font in Table 9.3) are found to show strong coupling with other states in the VCI calculation, and their occupation probabilities in total vibrational wavefunction are less than 50%, which are calculated from the VCI coefficients. Therefore, the assignments of ν_1 and ν_{11} fundamental states are problematic, and the calculated energies show relatively large differences with experimental results. However, agreement improves substantially in the 5MR calculation, indicating the importance of that level of potential representation for those states. For all other fundamental states, very good agreement is observed comparing our calculation with the experimental results with differences less than 10 cm^{-1}.

To summarize this section, a new, full-dimensional PES has been used in 14-mode MM calculations with a focus on the zero-point energy and the fundamental excitations. Comparison with vibrational energies measured in the experiments shows very good agreement. The Handy-Carter pruning method, as implemented in the latest version of MM, does result in a substantial reduction in the order of the H-matrix, and permits an application of the computationally intensive 5-mode representation of the potential.

9.5   Summary and Conclusions

In this study, we reported a new semi-global potential energy surface (PES) for nitromethane in full dimensionality. The fitting PES is quite accurate given that the root-mean-square error is only 0.37 cm^{-1} and the harmonic frequencies agree very well with direct *ab initio* calculations. The PES can also accurately describe the internal torsion motion of methyl group, and the torsion barrier was determined around 3.5 cm^{-1}. Based on the PES, a diffusion Monte Carlo calculation was performed to obtain the zero-point

energy and wavefunction of ground vibrational state. The visualization of wavefunction directly shows that the CH_3 group acts like a free rotor in the ground vibrational state.

The zero-point and fundamental energies of CH_3NO_2 were calculated using MULTIMODE, for which the effect of internal rotation can be neglected for the states of interest here. Thus, we coupled all the 14 vibration modes except the torsion mode of nitromethane in the MM calculation. For this large number of vibrational modes a pruning method introduced by Handy and Carter was applied to obtain these energies. The method was described in the context of matrix partitioning theory and tested for the first time on 12-mode ethylene.

4-mode excitations were allowed in the VSCF/VCI calculations for CH_3NO_2, and the maximum sum of 3- and 4-mode excitation quanta was equal to 8, which results in a large VCI matrix of size of order 94 690. The Handy-Carter pruning method was applied for the the VSCF/VCI calculations, and this greatly reduces the dimension of the H-matrix without a loss of accuracy. In the vibration calculation of nitromethane, the perturbation method achieved nearly identical results with regular calculations using full Hamiltonian matrix, but using much less memory and computation time. The calculated energies agree well with previous experimental results. This validates the accuracy of the PES, the neglect of the near free-rotor torsional mode and the good convergence of the VSCF/VCI calculations.

References

[1] Zhang, X.; Zou, S.; Harding, L. B.; Bowman, J. M. *J. Phys. Chem. A* **2004**, *108*, 8980–8986.

[2] Zou, S.; Bowman, J. M.; Brown, A. *J. Chem. Phys.* **2003**, *118*, 10012.

[3] Braams, B. J.; Bowman, J. M. *Int. Rev. Phys. Chem.* **2009**, *28*, 577–606.

[4] Xie, Z.; Bowman, J. M. *J. Chem. Theory Comput.* **2010**, *6*, 26–34.

[5] Derksen, H.; Kemper, G. *Computational Invariant Theory*; Springer Verlag: Berlin, 2002.

[6] Bosma, W.; Cannon, J.; Playoust, C. *J. Symbolic Comput.* **1997**, *24*, 235–265.

[7] Conte, R.; Qu, C.; Bowman, J. M. *J. Chem. Theory Comput.* **2015**, *11*, 1631–8.

[8] Wang, Y.; Huang, X.; Shepler, B. C.; Braams, B. J.; Bowman, J. M. *J. Chem. Phys.* **2011**, *134*, 094509.

[9] Wang, X.; Bowman, J. M. *J. Chem. Theory Comput.* **2013**, *9*, 901–908.

[10] Yang, B.; Zhang, P.; Wang, X.; Stancil, P. C.; Bowman, J. M.; Balakrishnan, N.; Forrey, R. C. *Nat. Commun.* **2015**, *6*, 6629.

[11] Wang, X.; Huang, X.; Bowman, J. M.; Lee, T. J. *J. Chem. Phys.* **2013**, *139*, 224302.

[12] Bowman, J. M.; Wang, X.; Homayoon, Z. *J. Mol. Spectros.* **2014**,

[13] Lin, H.-Y.; Huang, Y.-H.; Wang, X.; Bowman, J. M.; Nishimura, Y.; Witek, H. A.; Lee, Y.-P. *Nat. Commun.* **2015**, *6*, 7012.

[14] Kidwell, N. M.; Li, H.; Wang, X.; Bowman, J. M.; Lester, M. I. *Nat. Chem. (accepted)* **2016**,

[15] Wang, X.; Carter, S.; Bowman, J. M. *J. Phys. Chem. A* **2015**, *119*, 11632–40.

[16] Hase, W. L. *Encyclopedia of Computational Chemistry, Classical Trajectory Simulations: Initial Conditions,*; John Wiley & Sons, Ltd: Chichester, UK, 1998; pp 402–407.

[17] Chang, Y.-T.; Minichino, C.; Miller, W. H. *J. Chem. Phys.* **1992**, *96*, 4341.

[18] Rheinecker, J.; Zhang, X.; Bowman, J. *Mol. Phys.* **2005**, *103*, 1067–1074.

[19] Hase, W. L. *Encyclopedia of Computational Chemistry, Classical Trajectory Simulations: Final Conditions*; John Wiley & Sons, Ltd: Chichester, UK, 1998; pp 399–402.

[20] Bowman, J. M.; Gazdy, B.; Sun, Q. *J. Chem. Phys.* **1989**, *91*, 2859.

[21] Miller, W. H.; Hase, W. L.; Darling, C. L. *J. Chem. Phys.* **1989**, *91*, 2863.

[22] Bonhommeau, D.; Truhlar, D. G. *J. Chem. Phys.* **2008**, *129*, 014302.

[23] Czakó, G.; Kaledin, A. L.; Bowman, J. M. *J. Chem. Phys.* **2010**, *132*, 164103.

[24] Paul, A. K.; Hase, W. L. *J. Phys. Chem. A* **2016**,

[25] Anderson, J. B. *J. Chem. Phys.* **1975**, *63*, 1499.

[26] Kosztin, I. *Am. J. Phys.* **1996**, *64*, 633.

[27] McCoy, A. B. *Int. Rev. Phys. Chem.* **2006**, *25*, 77–107.

[28] Wang, Y.; Babin, V.; Bowman, J. M.; Paesani, F. *J. Am. Chem. Soc.* **2012**, *134*, 11116–11119.

[29] Carter, S.; Bowman, J. M.; Handy, N. C. *Theor. Chem. Acc.* **1998**, *100*, 191–198.

[30] Bowman, J. M.; Carter, S.; Huang, X. *Int. Rev. Phys. Chem.* **2003**, *22*, 533–549.

[31] Watson, J. K. *Mol. Phys.* **1968**, *15*, 479–490.

[32] Bowman, J. M. *J. Chem. Phys.* **1978**, *68*, 608.

[33] Bowman, J. M. *Acc. Chem. Res.* **1986**, *19*, 202–208.

[34] Norris, L. S.; Ratner, M. A.; Roitberg, A. E.; Gerber, R. B. *J. Chem. Phys.* **1996**, *105*, 11261.

[35] Jung, J. O.; Gerber, R. B. *J. Chem. Phys.* **1996**, *105*, 10332.

[36] Carter, S.; Bowman, J. M.; Harding, L. B. *Spectrochim. Acta A* **1997**, *53*, 1179–1188.

[37] Handy, N. C.; Carter, S. *Mol. Phys.* **2004**, *102*, 2201–2205.

[38] Burcl, R.; Carter, S.; Handy, N. C. *Chem. Phys. Lett.* **2003**, *380*, 237–244.

[39] Bair, R. A.; Dunning Jr., T. H. *J. Chem. Phys.* **1985**, *82*, 2280–2294.

[40] Wagner, A. F.; Bair, R. A. *Int. J. Chem. Kinet.* **1986**, *18*, 473–486.

[41] Sun, Q.; Yang, D. L.; Wang, N. S.; Bowman, J. M.; Lin, M. C. *J. Chem. Phys.* **1990**, *93*, 4730–4739.

[42] Sun, Q.; Bowman, J. M. *J. Chem. Phys.* **1990**, *92*, 5201–5210.

[43] ter Horst, M. A.; Schatz, G. C.; Harding, L. B. *J. Chem. Phys.* **1996**, *105*, 558.

[44] Sumathi, R.; Nguyen, M. T. *J. Phys. Chem. A* **1998**, *102*, 8013–8020.

[45] Wang, J.-H.; Liu, K.; Schatz, G. C.; ter Horst, M. *J. Chem. Phys.* **1997**, *107*, 7869–7875.

[46] Zhu, W.; Zhang, J. Z. H.; Zhang, Y. C.; Zhang, Y. B.; Zhan, L. X.; Zhang, S. L.; Zhang, D. H. *J. Chem. Phys.* **1998**, *108*, 3509–3516.

[47] Nguyen, M. T.; Sengupta, D.; Ha, T.-K. *J. Phys. Chem.* **1996**, *100*, 6499–6503.

[48] Kaledin, A. L.; Heaven, M. C.; Bowman, J. M. *J. Chem. Phys.* **1999**, *110*, 10380–10392.

[49] Troya, D.; Banos, I.; Gonzalez, M.; Wu, G.; ter Horst, M. A.; Schatz, G. C. *J. Chem. Phys.* **2000**, *113*, 6253–6263.

[50] Lambert, H. M.; Carrington, T.; Filseth, S. V.; Sadowski, C. M. *J. Phys. Chem.* **1993**, *97*, 128–133.

[51] Guo, Y.; Harding, L. B.; Wagner, A. F.; Minkoff, M.; Thompson, D. L. *J. Chem. Phys.* **2007**, *126*, 104105.

[52] Coletti, C.; Billing, G. D. *J. Chem. Phys.* **2000**, *113*, 11101–11108.

[53] Johnston, G. W.; Bersohn, R. *J. Chem. Phys.* **1989**, *90*, 7096–7102.

[54] Adler, T. B.; Knizia, G.; Werner, H. J. *J. Chem. Phys.* **2007**, *127*.

[55] Knizia, G.; Adler, T. B.; Werner, H. J. *J. Chem. Phys.* **2009**, *130*.

[56] Dunning Jr., T. H. *J. Chem. Phys.* **1989**, *90*, 1007–1023.

[57] Kendall, R. A.; Dunning Jr., T. H.; Harrison, R. J. *J. Chem. Phys.* **1992**, *96*, 6796–6806.

[58] Werner, H. J. et al. MOLPRO 2008. MOLPRO, Inc.

[59] Pfeiffer, J. M.; Metz, R. B.; Thoemke, J. D.; Woods III, E.; Crim, F. F. *J. Chem. Phys.* **1996**, *104*, 4490–4501.

[60] Kreher, C.; Theinl, R.; Gericke, K.-H. *J. Chem. Phys.* **1996**, *104*, 4481–4489.

[61] Johnson, D.; Marston, G. *Chem. Soc. Rev.* **2008**, *37*, 699–716.

[62] Criegee, R. *Angew. Chem., Int. Ed.* **1975**, *14*, 745–752.

[63] Osborn, D. L.; Taatjes, C. A. *Int. Rev. Phys. Chem.* **2015**, *34*, 309–360.

[64] Chao, W.; Hsieh, J.-T.; Chang, C.-H.; Lin, J. J.-M. *Science* **2015**, *347*, 751–4.

[65] Lewis, T. R.; Blitz, M. A.; Heard, D. E.; Seakins, P. W. *Phys. Chem. Chem. Phys.* **2015**, *17*, 4859–63.

[66] Lee, Y.-P. *J. Chem. Phys.* **2015**, *143*, 020901.

[67] Orzechowska, G. E.; Paulson, S. E. *Atmos. environ.* **2002**, *36*, 571–581.

[68] Paulson, S. E.; Orlando, J. J. *Geophy. Res. Lett.* **1996**, *23*, 3727–3730.

[69] Marston, G. *Science* **2012**, *335*, 178–179.

[70] Beames, J. M.; Liu, F.; Lu, L.; Lester, M. I. *J. Amer. Chem. Soc.* **2012**, *134*, 20045–20048.

[71] Taatjes, C. A.; Welz, O.; Eskola, A. J.; Savee, J. D.; Osborn, D. L.; Lee, E. P. F.; Dyke, J. M.; Mok, D. W. K.; Shallcross, D. E.; Percival, C. J. *Phys. Chem. Chem. Phys.* **2012**, *14*, 10391–10400.

[72] Taatjes, C. A.; Welz, O.; Eskola, A. J.; Savee, J. D.; Scheer, A. M.; Shallcross, D. E.; Rotavera, B.; Lee, E. P. F.; Dyke, J. M.; Mok, D. K. W.; Osborn, D. L.; Percival, C. J. *Science* **2013**, *340*, 177–180.

[73] Stone, D.; Whalley, L. K.; Heard, D. E. *Chem. Soc. Rev.* **2012**, *41*, 6348–404.

[74] Harrison, R. M. et al. *Sci. Total Environ.* **2006**, *360*, 5–25.

[75] Emmerson, K. M.; Carslaw, N.; Carslaw, D. C.; Lee, J. D.; McFiggans, G.; Bloss, W. J.; Gravestock, T.; Heard, D. E.; Hopkins, J.; Ingham, T.; Pilling, M. J.; Smith, S. C.; Jacob, M.; Monks, P. S. *Atmos. Chem. Phys.* **2007**, *7*, 167–181.

[76] Emmerson, K.; Carslaw, N. *Atmos. Environ.* **2009**, *43*, 3220–3226.

[77] Liu, F.; Beames, J. M.; Petit, A. S.; McCoy, A. B.; Lester, M. I. *Science* **2014**, *345*, 1596–1598.

[78] Beames, J. M.; Liu, F.; Lu, L.; Lester, M. I. *J. Chem. Phys.* **2013**, *138*, 244307.

[79] Beames, J. M.; Liu, F.; Lester, M. I.; Murray, C. *J. Chem. Phys.* **2011**, *134*, 241102.

[80] Kurtén, T.; Donahue, N. M. *J. Phys. Chem. A* **2012**, *116*, 6823–6830.

[81] Aquilante, F.; Vico, L. D.; Ferr, N.; Ghigo, G.; Malmqvist, P.-.; Neogrdy, P.; Pedersen, T. B.; Pitonk, M.; Reiher, M.; Roos, B.; Serrano-Andrs, L.; Urban, M.; Veryazov, V.; Lindh, R. *J. Comput. Chem.* **2010**, *31*, 224–247.

[82] Mordaunt, D. H.; Osborn, D. L.; Neumark, D. M. *J. Chem. Phys.* **1998**, *108*, 2448.

[83] Brouard, M. *Reaction Dynamics*; Oxford University Press, 1998.

[84] Drozd, G. T.; Kroll, J.; Donahue, N. M. *J. Phys. Chem. A* **2011**, *115*, 161–6.

[85] Lehman, J. H.; Li, H.; Beames, J. M.; Lester, M. I. *J. Chem. Phys.* **2013**, *139*, 141103.

[86] Li, H.; Fang, Y.; Beames, J. M.; Lester, M. I. *J. Chem. Phys.* **2015**, *142*, 214312.

[87] Nakajima, M.; Endo, Y. *J. Chem. Phys.* **2014**, *140*, 011101.

[88] Kuwata, K. T.; Hermes, M. R.; Carlson, M. J.; Zogg, C. K. *J. Phys. Chem. A* **2010**, *114*, 9192–9204.

[89] Novelli, a.; Vereecken, L.; Lelieveld, J.; Harder, H. *Phys. Chem. Chem. Phys.* **2014**, *16*, 19941–51.

[90] Yu, H.-G.; Muckerman, J. T.; Sears, T. J. *Chem. Phys. Lett.* **2001**, *349*, 547–554.

[91] Li, J.; Wang, Y.; Jiang, B.; Ma, J.; Dawes, R.; Xie, D.; Bowman, J. M.; Guo, H. *J. Chem. Phys.* **2012**, *136*, 041103.

[92] Lakin, M. J.; Troya, D.; Schatz, G. C.; Harding, L. B. *J. Chem. Phys.* **2003**, *119*, 5848.

[93] Chang, C.-H.; Buckingham, G. T.; Nesbitt, D. J. *J. Phys. Chem. A* **2013**,

[94] Wang, Y.; Carter, S.; Bowman, J. M. *J. Phys. Chem. A* **2013**, *117*, 9343–9352.

[95] Fortenberry, R. C.; Huang, X.; Francisco, J. S.; Crawford, T. D.; Lee, T. J. *J. Chem. Phys.* **2011**, *135*, 134301.

[96] Fortenberry, R. C.; Huang, X.; Francisco, J. S.; Crawford, T. D.; Lee, T. J. *J. Chem. Phys.* **2011**, *135*, 214303.

[97] Kohno, N.; Izumi, M.; Kohguchi, H.; Yamasaki, K. *J. Phys. Chem. A* **2011**, *115*, 4867–4873.

[98] Golden, D. M.; Smith, G. P.; McEwen, A. B.; Yu, C.-L.; Eiteneer, B.; Frenklach, M.; Vaghjiani, G. L.; Ravishankara, A. R.; Tully, F. P. *J. Phys. Chem. A* **1998**, *102*, 8598–8606.

[99] Chen, W.-C.; Marcus, R. A. *J. Chem. Phys.* **2005**, *123*, 094307.

[100] Clements, T. G.; Continetti, R. E.; Francisco, J. S. *J. Chem. Phys.* **2002**, *117*, 6478.

[101] Lu, Z.; Hu, Q.; Oakman, J. E.; Continetti, R. E. *J. Chem. Phys.* **2007**, *126*, 194305.

[102] Johnson, C. J.; Harding, M. E.; Poad, B. L. J.; Stanton, J. F.; Continetti, R. E. *J. Am. Chem. Soc.* **2011**, *133*, 19606–19609.

[103] Johnson, C. J.; Continetti, R. E. *J. Phys. Chem. Lett.* **2010**, *1*, 1895–1899.

[104] Zhang, S.; Medvedev, D. M.; Goldfield, E. M.; Gray, S. K. *J. Chem. Phys.* **2006**, *125*, 164312.

[105] Ma, J.; Li, J.; Guo, H. *Phys. Rev. Lett.* **2012**, *109*, 063202.

[106] Li, J.; Xie, C.; Ma, J.; Xie, D.; Bowman, J. M.; Guo, H. *J. Phys. Chem. A* **2012**, *116*, 5057–5067.

[107] Johnson, C. J.; Poad, B. L. J.; Shen, B. B.; Continetti, R. E. *J. Chem. Phys.* **2011**, *134*, 171106.

[108] Wang, Y.; Bowman, J. M. *J. Chem. Phys.* **2013**, *139*.

[109] Wang, Y.; Bowman, J. M. *J. Chem. Phys.* **2008**, *129*, 121103.

[110] Kamarchik, E.; Wang, Y.; Bowman, J. *J. Phys. Chem. A* **2009**, *113*, 7556–62.

[111] Sharma, A. R.; Bowman, J. M.; Nesbitt, D. J. *J. Chem. Phys.* **2012**, *136*, 034305.

[112] Chen, J.; Xu, X.; Zhang, D. H. *J. Chem. Phys.* **2013**, *138*, 221104.

[113] Jiang, B.; Guo, H. **2013**, *138*, 234104.

[114] Jiang, B.; Guo, H. *J. Amer. Chem. Soc.* **2013**, *135*, 15251–15256.

[115] Siebrand, W.; Smedarchina, Z.; Fernandez-Ramos, A. **2013**, *139*, 021101.

[116] Dreier, T.; Wolfrum, J. *Proc. Symp. Int. Combust.* **1981**, *18*, 801–809.

[117] Dzegilenko, F. N.; Bowman, J. M. *J. Chem. Phys.* **1998**, *108*, 511.

[118] Miller, W. *J. Amer. Chem. Soc.* **1979**, *101*, 6810–6814.

[119] Miller, W. H. *Chem. Rev.* **1987**, *87*, 19–27.

[120] Miller, W. H.; Hernandez, R.; Handy, N. C.; Jayatilaka, D.; Willetts, A. *Chem. Phys. Lett.* **1990**, *172*, 62–68.

[121] Nguyen, T. L.; Xue, B. C.; Weston, R. E.; Barker, J. R.; Stanton, J. F. *J. Phys. Chem. Lett.* **2012**, *3*, 1549–1553.

[122] Wagner, A. F. *J. Phys. Chem. A* **2013**, *117*, 13089–100.

[123] Truhlar, D. G. *J. Chem. Phys.* **1982**, *77*, 3516.

[124] Yoon, S.; Holiday, R. J.; Sibert, E. L.; Crim, F. F. *J. Chem. Phys.* **2003**, *119*, 9568.

[125] Weltner, W.; Vanzee, R. J. *Chem. Rev.* **1989**, *89*, 1713–1747.

[126] Van Orden, A.; Saykally, R. J. *Chem. Rev.* **1998**, *98*, 2313–2357.

[127] Watts, J. D.; Gauss, J.; Stanton, J. F.; Bartlett, R. J. *J. Chem. Phys.* **1992**, *97*, 8372–8381.

[128] Masso, H.; Senent, M. L.; Rosmus, P.; Hochlaf, M. *J. Chem. Phys.* **2006**, *124*.

[129] Zajfman, D.; Feldman, H.; Heber, O.; Kella, D.; Majer, D.; Vager, Z.; Naaman, R. *Science* **1992**, *258*, 1129–1131.

[130] Kella, D.; Zajfman, D.; Heber, O.; Majer, D.; Feldman, H.; Vager, Z.; Naaman, R. *Z. Phys. D Atom Mol. Cl.* **1993**, *26*, 340–342.

[131] Arnold, D. W.; Bradforth, S. E.; Kitsopoulos, T. N.; Neumark, D. M. *J. Chem. Phys.* **1991**, *95*, 8753.

[132] Martin, J. M. L.; Francois, J. P.; Gijbels, R. *J. Chem. Phys.* **1991**, *94*, 3753–3761.

[133] Martin, J. M. L.; Francois, J. P.; Gijbels, R. *J. Chem. Phys.* **1990**, *93*, 8850–8861.

[134] Thompson, K. R.; Dekock, R. L.; Weltner, W. *J. Am. Chem. Soc.* **1971**, *93*, 4688.

[135] Martin, J. M. L.; Schwenke, D. W.; Lee, T. J.; Taylor, P. R. *J. Chem. Phys.* **1996**, *104*, 4657–4663.

[136] Senent, M. L.; Masso, H.; Hochlaf, M. *Astrophys. J.* **2007**, *670*, 1510–1517.

[137] Mills, I. M. *Molecular Spectroscopy - Modern Research*; New York: Academic Press, 1972.

[138] Papousek, D.; Aliev, M. R. *Molecular Vibration-Rotation Spectra*; Amsterdam: Elsevier, 1982.

[139] Watson, J. K. G. *Vibrational Spectra and Structure*; Amsterdam: Elsevier, 1977.

[140] Willetts, A.; Gaw, F.; Green, W.; Handy, N. C. SPECTRO 3.0. University Chemical Laboratory, Cambridge, 1994.

[141] Gaw, J. F.; Willetts, A.; Green, W. H.; Handy, N. C. *Advances in Molecular Vibrations and Collision Dynamics*; JAI press: Greenwich, CT, USA, 1991; pp 170–185.

[142] Huang, X.; Lee, T. J. *Astrophys. J.* **2011**, *736*, 33.

[143] Huang, X.; Fortenberry, R. C.; Lee, T. J. *Astrophys. J.* **2013**, *768*, L25.

[144] Lee, T. J.; Taylor, P. R. *Int. J. Quantum Chem.* **1989**, 199–207.

[145] Martin, J. M.; Taylor, P. R.; Lee, T. J. *Chem. Phys. Lett.* **1997**, *275*, 414 – 422.

[146] Martin, J. M. L.; Taylor, P. R. *Chem. Phys. Lett.* **1994**, *225*, 473–479.

[147] Allen, W. D. et al. INTDER Program. 2005.

[148] Dateo, C. E.; Lee, T. J.; Schwenke, D. W. *J. Chem. Phys.* **1994**, *101*, 5853–5859.

[149] Bowman, J. M.; Czako, G.; Fu, B. *Phys. Chem. Chem. Phys.* **2011**, *13*, 8094–8111.

[150] Townes, C. H.; L., S. A. Microwave Spectroscopy. Dover Publications; 2nd edition, 2012.

[151] Sheps, L. *J. Phys. Chem. Lett.* **2013**, *4*, 4201–4205.

[152] Su, Y.-T.; Huang, Y.-H.; Witek, H. A.; Lee, Y.-P. *Science* **2013**, *340*, 174–176.

[153] Nakajima, M.; Endo, Y. *J. Chem. Phys.* **2013**, *139*, 101103.

[154] McCarthy, M. C.; Cheng, L.; Crabtree, K. N.; Martinez, O.; Nguyen, T. L.; Womack, C. C.; Stanton, J. F. *J. Phys. Chem. Lett.* **2013**, *4*, 4133–4139.

[155] Welz, O.; Savee, J. D.; Osborn, D. L.; Vasu, S. S.; Percival, C. J.; Shallcross, D. E.; Taatjes, C. A. *Science* **2012**, *335*, 204–207.

[156] Stone, D.; Blitz, M.; Daubney, L.; Howes, N. U. M.; Seakins, P. *Phys. Chem. Chem. Phys.* **2014**, *16*, 1139–49.

[157] Su, Y.-T.; Lin, H.-Y.; Putikam, R.; Matsui, H.; Lin, M. C.; Lee, Y.-P. *Nat. Chem.* **2014**, *6*, 477–83.

[158] Liu, Y.; Bayes, K. D.; Sander, S. P. *J. Phys. Chem. A* **2014**, *118*, 741–7.

[159] Nguyen, M. T.; Nguyen, T. L.; Ngan, V. T.; Nguyen, H. M. T. *Chem. Phys. Lett.* **2007**, *448*, 183–188.

[160] Li, J.; Carter, S.; Bowman, J. M.; Dawes, R.; Xie, D.; Guo, H. *J. Phys. Chem. Lett.* **2014**, *5*, 2364–2369.

[161] Sheps, L.; Scully, A. M.; Au, K. *Phys. Chem. Chem. Phys.* **2014**, *16*, 26701–6.

[162] Cox, A. P.; Waring, S. *J. Chem. Soc. Faraday Trans.* **1972**, *68*, 1060.

[163] Rohart, F. *J. Mol. Spectrosc.* **1975**, *57*, 301–311.

[164] Sø rensen, G.; Pedersen, T.; Dreizler, H.; Guarnieri, A.; Peter Cox, A. *J. Mol. Struct.* **1983**, *97*, 77–82.

[165] Wells, A. J.; Wilson, E. B. *J. Chem. Phys.* **1941**, *9*, 314.

[166] Jones, W. J.; Sheppard, N. *Proc. R. Soc. London A* **1968**, *304*, 135–155.

[167] McKean, D.; Watt, R. *J. Mol. Spectrosc.* **1976**, *61*, 184–202.

[168] Hill, J. R.; Moore, D. S.; Schmidt, S. C.; Storm, C. B. *J. Phys. Chem.* **1991**, *95*, 3037–3044.

[169] Cavagnat, D.; Lespade, L. *J. Chem. Phys.* **1997**, *106*, 7946–7957.

[170] Halonen, M.; Halonen, L.; Callegari, A.; Lehmann, K. K. *J. Phys. Chem. A* **1998**, *102*, 9124–9128.

[171] Hazra, A.; Ghosh, P.; Kshirsagar, R. *J. Mol. Spectrosc.* **1994**, *164*, 20–26.

[172] Pal, C.; Hazra, A.; Ghosh, P. N.; Kshirsagar, R. *J. Mol. Struct.* **1997**, *407*, 165–170.

[173] Dawadi, M. B.; Twagirayezu, S.; Perry, D. S.; Billinghurst, B. E. *J. Mol. Spectrosc.* **2014**, *315*, 10–15.

[174] Bock, C. W.; Krasnoshchiokov, S.; Khristenko, L.; Panchenko, Y.; Pentin, Y. *J. Mol. Struct.* **1987**, *149*, 201–211.

[175] Gorse, D.; Cavagnat, D.; Pesquer, M.; Lapouge, C. *J. Phys. Chem.* **1993**, *97*, 4262–4269.

[176] Huang, X.; Braams, B. J.; Bowman, J. M. *J. Chem. Phys.* **2005**, *122*, 44308.

[177] Bowman, J. M.; Huang, X.; Handy, N. C.; Carter, S. *J. Phys. Chem. A* **2007**, *111*, 7317–7321.

[178] Bacic, Z.; Light, J. C. *Ann Rev. Phys. Chem.* **1989**, *40*, 469–498.

[179] Bowman, J. M.; Gazdy, B. *J. Chem. Phys* **1991**, *94*, 454–460.

[180] Avila, G.; Carrington, T. *J. Chem. Phys.* **2011**, *135*.

[181] Carter, S.; Bowman, J. M.; Handy, N. C. *Mol. Phys.* **2012**, *110*, 775–781.